



저작자표시-비영리-변경금지 2.0 대한민국

이용자는 아래의 조건을 따르는 경우에 한하여 자유롭게

- 이 저작물을 복제, 배포, 전송, 전시, 공연 및 방송할 수 있습니다.

다음과 같은 조건을 따라야 합니다:



저작자표시. 귀하는 원저작자를 표시하여야 합니다.



비영리. 귀하는 이 저작물을 영리 목적으로 이용할 수 없습니다.



변경금지. 귀하는 이 저작물을 개작, 변형 또는 가공할 수 없습니다.

- 귀하는, 이 저작물의 재이용이나 배포의 경우, 이 저작물에 적용된 이용허락조건을 명확하게 나타내어야 합니다.
- 저작권자로부터 별도의 허가를 받으면 이러한 조건들은 적용되지 않습니다.

저작권법에 따른 이용자의 권리는 위의 내용에 의하여 영향을 받지 않습니다.

이것은 [이용허락규약\(Legal Code\)](#)을 이해하기 쉽게 요약한 것입니다.

[Disclaimer](#)

공학박사학위논문

전방향 전단 탄성과 구현을 위한
평판용 초음파 트랜스듀서

Ultrasonic Transducers for Omnidirectional
Shear-Horizontal Elastic Waves in Plate Structures

2016년 2월

서울대학교 대학원

기계항공공학부

승 홍 민

ABSTRACT

Ultrasonic Transducers for Omnidirectional Shear-Horizontal Elastic Waves in Plate Structures

Hong Min Seung

School of Mechanical and Aerospace Engineering

The Graduate School

Seoul National University

This dissertation is concerned with the development and characterization of new ultrasonic guided wave transducers that generate and measure omnidirectional shear-horizontal elastic waves in plate structures. Because all of the previous researches focused on the development of omnidirectional guided wave transducers have been limited to use Lamb wave only, by using the developed transducers in this work, not only the disadvantages of using Lamb waves are overcome but more effective inspection of plates is possible. To this end, two types of omnidirectional shear-horizontal wave transducers, a magnetostrictive patch transducer and an electromagnetic acoustic transducer, are newly developed and investigated.

First, an omnidirectional shear-horizontal wave magnetostrictive patch transducer is developed. The performances and characteristics of the transducer are investigated through simulations and experiments. Moreover, the effect of magnetic flux leakage on the poor performance of the transducer installed on a ferromagnetic plate is studied. To resolve the leakage issue, a method to optimally configure the transducer is proposed. By doing so, the possibility of practical applications using the transducer is shown.

An electromagnetic acoustic transducer for the noncontact transduction of omnidirectional shear-horizontal waves in metallic plates is also developed. Because the transducer is easily installed on plates without any bonding material, more accurate, efficient and various applications are possible. In order to check the effectiveness of the transducer, numerical analysis and experiments are carried out. By successfully evaluating the transducer performances, the usefulness of the transducer is confirmed.

Keywords: Ultrasonic transducer, Omnidirectional wave, Shear-horizontal wave, Guided wave, Magnetostrictive patch transducer, Electromagnetic acoustic transducer

Student Number: 2010-20689

CONTENTS

ABSTRACT	i
CONTENTS.....	iii
LIST OF TABLES.....	vii
LIST OF FIGURES.....	viii
CHAPTER 1 INTRODUCTION	1
1.1 Research Motivation	1
1.2 Research Objectives	3
1.3 Thesis Outline	7
CHAPTER 2 ULTRASONIC TRANSDUCERS FOR PLATES.....	11
2.1 Overview	11
2.2 Ultrasonic Guided Waves in Plate Structures.....	12
2.2.1 Guided wave based NDE and SHM of plates	13
2.2.2 Lamb and shear-horizontal (SH) waves	14
2.2.3 Advantages of using SH waves over Lamb waves.....	21

2.3 Magnetostrictive Patch Transducer (MPT)	23
2.3.1 Magnetostriction.....	23
2.3.2 MPTs for SH wave transduction	26
2.4 Electromagnetic Acoustic Transducer (EMAT)	27
2.4.1 Lorentz force mechanism for EMATs	28
2.4.2 EMATs for SH wave transduction.....	29

**CHAPTER 3 OMNIDIRECTIONAL SHEAR-HORIZONTAL WAVE
MAGNETOSTRICTIVE PATCH TRANSDUCER (OSH-MPT).....43**

3.1 Overview	43
3.2 Development of OSH-MPT.....	45
3.2.1 Configuration and working mechanism	46
3.2.2 Coil winding strategy	50
3.3 OSH-MPT for a Nonferromagnetic Plate.....	51
3.3.1 SH wave transduction and transducer sensitivity.....	52
3.3.2 Omnidirectivity of the SH wave by OSH-MPT	56
3.3.3 Frequency characteristic.....	60
3.3.4 Optimal static magnetic field strength in patches.....	62
3.4 OSH-MPT for a Ferromagnetic Plate.....	64
3.4.1 Issue on OSH-MPT for a ferromagnetic plate.....	66
3.4.2 Investigation of magnetic flux leakage problem	68
3.4.3 Design of OSH-MPT for a ferromagnetic plate	74

3.4.4 Experimental verification and discussion.....	80
3.5 Concluding Remarks	83

CHAPTER 4 OMNIDIRECTIONAL SHEAR-HORIZONTAL WAVE ELECTROMAGNETIC ACOUSTIC TRANSDUCER (OSH-EMAT) 118

4.1 Overview	118
4.2 Fundamentals of OSH-EMAT	121
4.2.1 Configuration and coil winding.....	122
4.2.2 Working principle.....	123
4.3 Design of OSH-EMAT	125
4.3.1 Design issue on the magnet size and wavelength.....	126
4.3.2 Transducer design by simulations	128
4.3.3 The effect of magnet width ratio	131
4.4 Experiments.....	133
4.4.1 SH wave transduction using OSH-EMAT	133
4.4.2 Frequency characteristic.....	135
4.4.3 Radiation pattern of the SH wave by OSH-EMAT	136
4.5 Concluding Remarks	138

CHAPTER 5 CONCLUSIONS 162

APPENDIX A. EFFECT OF STATIC MANGETIC FIELD STRENGTH ON THE PERFORMANCE OF LAMB AND SH WAVE MANGETOSTRICTIVE PATCH TRANSDUCERS.....	166
A.1 Overview	166
A.2 Experimental investigation.....	168
A.3 Piezomagnetic theory	172
A.4 Analysis	177
A.5 Discussion	179
REFERENCES.....	189

LIST OF TABLES

Table 3.1 The numerical values of the geometries of considered magnetostrictive patches and the corresponding peak frequency/wavelength of the SH0 wave mode yielding the maximum wave magnitude.87

Table 3.2 The optimal static magnetic fields applied to the patches for the OSH-MPTs of three different sizes and the corresponding vertical positions of the used cylindrical magnets.88

Table 3.3 The width of the nickel patch (D) and the corresponding central frequency (f_c)/wavelength(λ) of the SH0 wave mode. The symbol $^*\hat{H}_r^{S-NP}$ denotes the optimal value of the averaged values of the radial static magnetic field in the nickel patch (\hat{H}_r^{S-NP}), when the SH0 signal measured by the pair of OSH-MPTs installed on the 1 mm thick aluminum plate is largest.....89

Table 4.1 The peak wavelengths of SH waves for varying widths of the ring magnets satisfying the condition $r_1 = 0.25a$ and the corresponding scaling factor.140

LIST OF FIGURES

Fig. 1.1 Photos of the previously developed omnidirectional Lamb wave transducers on a plate. (a) A piezoelectric transducer type, (b) an electromagnetic acoustic transducer (EMAT) type and (c) a magnetostrictive patch transducer type, respectively.	9
Fig. 1.2 A conceptual drawing of the omnidirectional shear-horizontal (SH) wave generation by a circular deformation in a plate structure.	10
Fig. 2.1 Schematic drawings of the generation of (a) bulk waves (Compressional and shear waves) in an elastic bulk media and (b) guided waves (Lamb and shear-horizontal waves) in an elastic plate.	31
Fig. 2.2 Illustrations of ultrasonic inspections using (a) bulk elastic waves and (b) guided waves.	32
Fig. 2.3 Lamb wave propagation in an elastic plate and the designated coordinate systems for (a) a symmetric mode and (b) a antisymmetric mode with the mode shapes along the plate thickness.	33

Fig. 2.4 Shear-horizontal (SH) wave propagation in an elastic plate. The particle motion is only in the z direction and there are no deformations in y direction on the top and bottom surfaces of the plate.....34

Fig. 2.5 The dispersion curves of (a) Lamb waves and (b) SH waves for an aluminum plate. The horizontal axis represents the frequency*thickness while the vertical axis represents the phase velocity.35

Fig. 2.6 Measured guided wave signals. (a) A dispersive wave signal and (b) a nondispersive wave signal. The waveform of the first arrival in a dispersive wave is distorted due to various velocity components.36

Fig. 2.7 Illustration of the magnetostrictive effect of a ferromagnetic material. The disordered magnetic domains are aligned and rotated by the applied magnetic field and thus the mechanical strain (magnetostriction) of the material is generated.....37

Fig. 2.8 (a) Nonlinear magnetostriction curve and (b) magnetization curve of a magnetostrictive material (pure nickel) with a hysteresis property.38

Fig. 2.9 Illustrations for deformation of a magnetostrictive patch by the induced magnetostriction. (a) Static and dynamic magnetic fields are applied to a

patch in the same direction for Lamb wave generation while (b) two fields are orthogonally applied to a patch for SH wave generation.39

Fig. 2.10 Schematic configuration of a SH wave MPT operating on a plate. The static magnetic field by the magnets is perpendicular to the dynamic magnetic field by the coil and the two fields are directly applied to the patch.40

Fig. 2.11 Lorentz force generation by an electromagnetic acoustic transducer (EMAT) consisting of a magnet and a coil on a metallic plate. The cross product of the induced eddy current by the coil and the static magnetic flux from the magnet produces the Lorentz force acting on the plate.41

Fig. 2.12 Schematic configuration of a SH wave EMAT acting on a metallic plate. The EMAT consists of a pair of magnets having different magnetic polarities and a coil. The resulting Lorentz force by the EMAT generates SH waves dominantly in x direction.42

Fig. 3.1 Schematic configuration of (a) thin annular nickel patch used in (b) the developed OSH-MPT on a plate (nonferromagnetic) with the indicated static and dynamic magnetic fields.90

Fig. 3.2 Fabrication process of the OSH-MPT. (a) A thin annular nickel patch and a

hosting plastic guide with notches along the circumference. (b) Toroidally wound coil on the set consisting of the patch and the guide. The OSH-MPT connected to an electrical terminal with (c) and without a magnet (d).91

Fig. 3.3 Drawing of the coil winding on the patch and the hosting guide. Step 1 is coil winding for odd numbered notches while Step 2 is for even numbered notches after finishing Step 1. The directions of the current and magnetic field by the coil are indicated by the arrows.....92

Fig. 3.4 Pitch-catch type experimental setup for SH wave transduction in an aluminum plate using a pair of OSH-MPTs.93

Fig. 3.5 (a) Dispersion curves in terms of group velocity and frequency for Lamb and SH wave modes in a 1 mm thick aluminum plate. (b) Measured wave signal of the generated SH waves using the OSH-MPTs.94

Fig. 3.6 (a) Measured waveform of the first arrival of SH₀ mode by the OSH-MPTs. (b) Sensitivity characteristic of the OSH-MPT checked by varying input current in the transmitter coil.95

Fig. 3.7 (a) Illustration of schematic model of OSH-MPT for finite element analysis in an aluminum plate. (b) Snapshot of omnidirectionally propagating shear

strain $\varepsilon_{r\theta}$ (SH wave) by numerical simulation conducted in an aluminum plate.....	96
Fig. 3.8 Experimental setup to check the omnidirectional generation of SH wave by the transmitting OSH-MPT and experimentally measured radiation pattern.	97
Fig. 3.9 Experimental setup to check the omnidirectional measurement of SH waves using the receiving OSH-MPT and experimentally measured radiation pattern.....	98
Fig. 3.10 (a) The installation process of the OSH-MPT used for the radiation pattern experiments. The bonding material and the wound coil are directly placed on the plate. (b) The used sigle-line MPT for the radiation pattern experiments.	99
Fig. 3.11 (a) Illustration of an annular nickel patch. The inner diameter ($2r_i$) and the difference between the outer and inner radius ($r_o - r_i$) of the patch are equal to half the wavelength (0.5λ) of target frequencies for SH wave modes. (b) Fabricated OSH-MPTs of three different patch sizes (target wavelengths).....	100

Fig. 3.12 Experimental results of the frequency characteristics of the three different sizes of OSH-MPTs. The peak frequency for each case is indicated by solid line circles..... 101

Fig. 3.13 Schematic diagram of the nonlinear amplitude variation of SH wave MPTs according to varying static magnetic fields applied to patches. 102

Fig. 3.14 (a) Two dimensional axisymmetric configuration of the OSH-MPT for the static magnetic field analysis including (b) magnetization curve of pure nickel in [101]. 103

Fig. 3.15 Static magnetic field distribution in the patch along the radial direction by varying (a) the diameter (d_M) and (b) the vertical position (h) of the magnet for Case 2 model. (c) Simulations results of static magnetic fields in the patches for Case 1~3 to find the optimal value (H_o), which is indicated by dotted circles. 104

Fig. 3.16 Measured SH wave signals using the OSH-MPT for case 2 according to various h values. The largest first arrival signal of SH0 mode is measured at $h = 8$ mm 105

Fig. 3.17 (a) Schematic illustration of the OSH-MPT bonded onto a ferromagnetic plate with the bonding layer of (h_p) in thickness. The parameters related to geometries are defined and the generated static and dynamic magnetic fields are indicated. (b) Photos of OSH-MPT prototypes on a ferromagnetic plate with and without a magnet..... 106

Fig. 3.18 Experimentally measured signals using a pair of OSH-MPTs installed on a non-ferromagnetic (aluminum) and a ferromagnetic (AISI1008) plate in the pitch catch manner, respectively. For the ferromagnetic plate (Case 2), the amplitude of the SH0 mode substantially decreased and the unwanted S0 mode was measured..... 107

Fig. 3.19 Detailed drawings of part A shown in Fig. 3.16 (a). Specific coil configuration and current flow in the coil are indicated. (b) The several types of magnetic fields generated by the magnet and coils are illustrated. 108

Fig. 3.20 Numerical simulation results for the static magnetic field of the OSH-MPTs installed on a nonferromagnetic and a ferromagnetic plate, respectively. Owing to the leakage, the averaged value of the radial static magnetic field in the nickel patch (\hat{H}_r^{S-NP}) placed on the ferromagnetic plate is smaller

than that in the patch placed on the nonferromagnetic plate 109

Fig. 3.21 (a) Numerical simulation results for the radial dynamic magnetic field (H_r^D) generated by only the circumferentially wound coil of the OSH-MPT (150 kHz, $D=10$ mm) placed on the ferromagnetic plate. (b) Normalized signals of H_r^D at the measurement point indicated by the red dot in Fig. 3.20 (a) and (b) its peak-to-peak values for various h_p values. 110

Fig. 3.22 Experimental setup for the SH wave transduction using a pair of OSH-MPTs in the pitch-catch manner. A photo in the inset shows the specially fabricated housing to accurately control the thickness of the bonding layer (epoxy resin) between the patch and the plate..... 111

Fig. 3.23 Amplitude variation of measured SH waves using the three different sizes of OSH-MPTs installed on a nonferromagnetic plate. The peak values for each case are marked by the dotted circles..... 112

Fig. 3.24 Numerical simulation results for the \hat{H}_r^{S-NP} values of the OSH-MPTs placed on the ferromagnetic plate for different D and various h_m values

when (a) $h_p = 0$, (b) 1.0 mm and (c) 2.0 mm. The optimal value listed in Table 3.2 ($^* \hat{H}_r^{S-NP}$) is denoted by the purple horizontal line. The solid dots denote the points of the optimal combinations of (h_p, h_m) yielding $^* \hat{H}_r^{S-NP}$ 113

Fig. 3.25 Experimental results for the OSH-MPT ($D = 15$ mm). (a) Normalized Peak-to-peak values are shown. The optimal combination of h_p and h_m from the simulation results are indicated by the dotted circles. The time signals for the fixed h_m values (shown as a dashed vertical line) are also shown in (b). At the optimal condition, not only is the SH mode enhanced, but the S0 mode is also greatly suppressed. The A_{\max} is the largest value of the SH0 mode at the optimal condition for comparing the transduction efficiency with those from other cases. 114

Fig. 3.26 Experimental results for the OSH-MPT ($D = 10$ mm). (a) Normalized Peak-to-peak values are shown. The optimal combination of h_p and h_m from the simulation results are indicated by the dotted circles. The time signals for the fixed h_m values (shown as a dashed vertical line) are also shown in (b). At the optimal condition, not only is the SH mode enhanced,

but the S0 mode is also greatly suppressed. The A_{\max} is the largest value of the SH0 mode at the optimal condition for comparing the transduction efficiency with those from other cases. 115

Fig. 3.27 Experimental results for the OSH-MPT ($D = 7.5$ mm). (a) Normalized Peak-to-peak values are shown. The optimal combination of h_p and h_m from the simulation results are indicated by the dotted circles. The time signals for the fixed h_m values (shown as a dashed vertical line) are also shown in (b). At the optimal condition, not only is the SH mode enhanced, but the S0 mode is also greatly suppressed. The A_{\max} is the largest value of the SH0 mode at the optimal condition for comparing the transduction efficiency with those from other cases. 116

Fig. 3.28 The numerical simulation results of the optimal combination of h_p and h_m (satisfying $^* \hat{H}_r^{S-NP}$ value) for various D values. The corresponding frequency range for the used D values is approximately from 100 kHz to 600 kHz. 117

Fig. 4.1 Dispersion curves of phase velocities for (a) Lamb and (b) SH waves in a 1 mm thick aluminum plate. 141

Fig. 4.2 (a) Schematic configuration of the OSH-EMAT in the top and cross-sectional views. (b) Photo of a prototype of the OSH-EMAT placed on an aluminum plate. 142

Fig. 4.3 (a) Illustration of coil winding with the direction of AC current flow. (b) Photo of the finished coil winding on the magnets. 143

Fig. 4.4 Illustration of the static magnetic flux lines and AC current flow in the coil. The Lorentz force (f_{θ}^L) in the circumferential direction generated in the plate is also sketched 144

Fig. 4.5 Schematic drawing of a noncontact EMAT that generates omnidirectional SH waves in a metallic plate. 145

Fig. 4.6 Schematic configurations of the conventional EMAT equipped with rectangular magnets used to generate unidirectional SH waves. 146

Fig. 4.7 Schematic configurations of the proposed OSH-EMAT equipped with ring magnets developed to generate omnidirectional SH waves. 147

Fig. 4.8 A three-dimensional finite element model of the proposed EMAT and the snapshot of the shear strain ($\varepsilon_{r\theta}$) distributions at $t = 20 \mu\text{s}$ by time

transient simulation.	148
Fig. 4.9 (a) The snapshot of the shear strain ($\varepsilon_{r\theta}$) distributions at $t = 60 \mu\text{s}$ by time transient simulation. (b) The signal of the induced current in the receiver coil.	149
Fig. 4.10 Frequency characteristics of the OSH-EMAT by the simulations for the five cases. PTPs of J^i : the peak-to-peak values of the induced current density in the coil of the receiving EMAT, $f_{\text{SH}}^{\text{peak}}$: the peak frequency yielding the largest PTP value, $\lambda_{\text{SH}}^{\text{peak}}$: the peak wavelength of the SH0 wave mode corresponding to $f_{\text{SH}}^{\text{peak}}$	150
Fig. 4.11 Schematic figure of OSH-EMAT for defining the widths of the inner and outer ring magnets.	151
Fig. 4.12 The measured signals by simulations for various r_m values ($r_m = w_1 / w_2$). The simulations are performed for $r_m < 1$ using the OSH-EMAT for Case 3. The symbol A_{Ref} represents the peak-to-peak amplitude of the measured signal for $r_m = 1$ case.	152

Fig. 4.13 The measured signals by simulations for various r_m values ($r_m = w_1 / w_2$).

The simulations are performed for $r_m > 1$ using the OSH-EMAT for Case

3. The symbol A_{Ref} represents the peak-to-peak amplitude of the measured signal for $r_m = 1$ case..... 153

Fig. 4.14 Frequency characteristics calculated by numerical simulations for $r_m > 1$ case. The used OSH-EMAT is Case 3. 154

Fig. 4.15 Experimental setup for SH wave transduction using the two OSH-EMATs (one: transmitter, the other: receiver) installed on a 1 mm thick aluminum plate. 155

Fig. 4.16 (a) The measured SH0 mode signal by the EMAT at 130 kHz and (b) its short time Fourier transform (STFT) result. 156

Fig. 4.17 (a) Comparison of the frequency characteristics of the EMATs by experiments and simulations. The width of the two magnets is $a = 20$ mm. (b) SH wave signals are chosen at around the peak frequencies ($f_{\text{SH}}^{\text{peak}}|_{\text{sim}}$) as indicated with dotted circles in (a). 157

Fig. 4.18 (a) Comparison of the frequency characteristics of the EMATs by experiments and simulations. The width of the two magnets is $a = 15 \text{ mm}$.
 (b) SH wave signals are chosen at around the peak frequencies ($f_{\text{SH}}^{\text{peak}}|_{\text{sim.}}$) as indicated with dotted circles in (a). 158

Fig. 4.19 (a) Comparison of the frequency characteristics of the EMATs by experiments and simulations. The width of the two magnets is $a = 10 \text{ mm}$.
 (b) SH wave signals are chosen at around the peak frequencies ($f_{\text{SH}}^{\text{peak}}|_{\text{sim.}}$) as indicated with dotted circles in (a). 159

Fig. 4.20 The radiation pattern experiment of the transmitting OSH-EMAT at 130 kHz. (The unidirectional SH wave magnetostrictive patch transducer (MPT) is used as a receiver.) (a) The experimental setup, (b) the radiation pattern determined by the experimental results and the comparison of the signals with the maximum and minimum amplitudes. 160

Fig. 4.21 The radiation pattern experiment of the receiving OSH-EMAT at 130 kHz. (The unidirectional SH wave magnetostrictive patch transducer (MPT) is used as a transmitter.) (a) The experimental setup, (b) the radiation pattern determined by the experimental results and the comparison of the signals with the maximum and minimum amplitudes. 161

Fig. A.1 The configuration of the magnetostrictive patch transducer and the specification of the patch used in this investigation. Different configurations of figure-of-eight coils for the S0 and SH0 wave modes are also indicated. 181

Fig. A.2 The overall experimental setup for guided wave transduction using a pair of the proposed magnetostrictive patch transducers. 182

Fig. A.3 Normalized peak-to-peak values (V_{p-p}) of the S0 wave mode corresponding to various static magnetic flux densities in the transmitter (\mathbf{B}_T^S) for three different static magnetic flux densities in the receiver (\mathbf{B}_R^S). 183

Fig. A.4 Normalized peak-to-peak values (V_{p-p}) of the SH0 wave mode corresponding to various static magnetic flux densities in the transmitter (\mathbf{B}_T^S) for three different static magnetic flux densities in the receiver (\mathbf{B}_R^S). 184

Fig. A.5 Normalized peak-to-peak values (V_{p-p}) of the S0 wave mode corresponding to various static magnetic flux densities in the receiver (\mathbf{B}_R^S) for three different static magnetic flux densities in the transmitter (\mathbf{B}_T^S). 185

Fig. A.6 Normalized peak-to-peak values (V_{p-p}) of the SH0 wave mode corresponding to various static magnetic flux densities in the receiver (\mathbf{B}_R^S) for three different static magnetic flux densities in the transmitter (\mathbf{B}_T^S).186

Fig. A.7 Coordinate systems for the piezomagnetic theory analysis of (a) Lamb and (b) SH wave cases. Static, dynamic and total magnetic fields are depicted for both case.187

Fig. A.8 Comparison between experimental and theoretical results for (a) the S0 wave mode and (b) the SH0 wave mode according to various static magnetic field strengths in the transmitter (\mathbf{H}_T^S)188

CHAPTER 1

INTRODUCTION

1.1 Research Motivation

Large plate structure systems in industrial fields, such as airplane wings and high pressure vessels, contain many kinds of defects as time passes. To detect defects of plate structures earlier than the failure of systems, nondestructive evaluation (NDE) and structural health monitoring (SHM) techniques using ultrasonic elastic waves are widely used. Among various ultrasonic techniques, guided wave based technique is most preferred for plate inspections [1-6]. This is because guided waves propagate long distance in a short time along plates and thus cover wide areas efficiently. The guided wave technique is also suitable for the inspection of pipe structures [7-11] and inaccessible hidden regions of structures [12-14].

For the effective inspection of plates using guided waves, forming a phased array system with multiple transducers has received much attention [15-17]. Using the phased array system, it is easy to focus wave energy at a desired point on a plate by controlling time delay and amplitude. By doing so, highly sensitive detection of

small cracks in plates is possible. Especially, if the system is formed by an array of omnidirectional guided wave transducers, it allows wave focusing in any direction and at any point on a plate. Therefore, more rapid and high-performance inspection of large plates can be realized using the phased array system equipped with omnidirectional guided wave transducers [18-23].

Because transducers are essential elements of a phased array system, a number of researches have been performed to develop various kinds of omnidirectional transducers using piezoelectric element [24-28], Lorentz force [29-34] and magnetostrictive effect [35]. Although there are several disadvantages inherent in using Lamb waves, which are a type of guided waves in plates, *all these previous researches are concerned with only omnidirectional Lamb wave transducers.* (Fig. 1.1 shows the photos of some previously developed omnidirectional Lamb wave transducers.) *Motivated by this, in this work, two types of omnidirectional shear-horizontal (SH) wave transducers using magnetostrictive effect and Lorentz force, respectively, are newly developed and characterized. It is expected that if the newly developed transducers are employed for phased array systems, not only the disadvantages of using Lamb waves can be overcome but more effective inspections of plates are possible.* SH waves are the other type of guided waves in plates and the detailed comparison of Lamb and SH waves will be discussed in Section 2.2.

Magnetostrictive effect is a coupling phenomenon between the change of magnetic and mechanical fields in ferromagnetic (magnetostrictive) materials [36-38]. Magnetostrictive patch transducers (MPTs) are operated by this effect [39]. MPTs usually consist of a thin magnetostrictive patch bonded onto plates with bonding material, a coil and magnets. MPTs are highly sensitive and easy to generate SH waves for plate inspections [40-43]. Accordingly, MPT techniques are adopted to develop an omnidirectional SH wave transducer.

Electromagnetic acoustic transducers (EMATs) are operated by the Lorentz force mechanism [44] and commonly used for SH wave transduction. EMATs simply consist of magnets and coils. Moreover, because EMATs are installed on metallic plates without any physical contact, noncontact transduction of guided waves are possible. Using the noncontact feature of EMATs, various practical inspections can be performed. Hence, it is worth developing a new EMAT for omnidirectional SH wave transduction.

1.2 Research Objectives

The main objective of this research is to develop an omnidirectional shear-horizontal (SH) wave magnetostrictive patch transducer (MPT) and an omnidirectional SH wave electromagnetic acoustic transducer (EMAT) for plates, respectively. Because the transducers are new, its performance, characteristics and

the possibility for plate applications should be investigated.

The specific objectives concerned in this research can be summarized as follows:

● *Development and realization of omnidirectional SH wave MPT and EMAT*

To generate omnidirectional SH waves in plates, a circular deformation (similar to a torsional deformation) along the circumferential direction is needed as shown in Fig. 1.2. In other words, the transducers should be designed to have axisymmetric configuration and excite the surface of plates circularly. Before designing the transducers, the mechanisms of MPTs and EMATs for SH wave transduction in plate structures should be fully understood. After that, the detailed configuration of the transducers is considered. In developing an omnidirectional SH wave MPT, an annular thin nickel patch, a toriodally wound coil on the patch and a cylindrical permanent magnet placed on the patch are considered. On the other hand, the developed omnidirectional SH wave EMAT consists of a two ring magnets of different radii and a specially wound coil on the magnets. Because the coil winding strategies for both transducers are a little tricky, a thin hosting plastic guide having uniform notches along the inner and outer circumferences is also designed. The detailed configuration and working principle of both transducers are explained with the schematic drawings and photos.

● *Evaluation of the developed MPT and EMAT*

The developed MPT and EMAT should generate and measure omnidirectional SH waves in plate structures. That is, the generated SH waves by the transducers propagate uniformly in all direction without being accompanied by other unwanted wave modes such as Lamb wave modes. In order to confirm the omnidirectivity of the SH wave by the transducers, numerical and experimental studies are carried out. In addition, some attempts to improve the transducer sensitivity are made. For the MPT case, the deformation of the patch is highly affected by the applied static magnetic field strength on the patch. Therefore, to supply appropriate a static magnetic field, the size and vertical position of magnet are optimally determined through simulations and experiments. In case of the EMAT, the conventional design scheme of the magnet size is properly modified for the axisymmetric configuration. By doing so, the constructive interference between the circular deformations of plates underneath each ring magnet occurs and thus the omnidirectional SH waves are generated. The experimental evaluation of the developed transducers is mainly performed to check the omnidirectional radiation patterns of the generated SH waves by the EMAT. Auxiliary simulations are also numerically conducted to support experimental results.

● Characterization of the developed MPT and EMAT

In using guided wave transducers for plate inspections, the selection of the desired guided wave mode at a target frequency is an important issue. While there are three modes in bulk waves (one longitudinal and two transverse), guided waves have an infinite number of modes according to various frequencies and structure geometries. Considering the dispersive feature of higher SH waves, the prototypes of the MPT and EMAT are fabricated to be operated at the frequency range lower than the first cut off frequency of the SH wave modes. In other words, the transducers are designed to effectively excite the first SH wave mode (SH₀ mode), which is a single nondispersive mode among all guided wave modes in plates. Moreover, to maximize the transducer output at a target excitation frequency, i.e. to make frequency-tuned omnidirectional SH wave transducers, the main components of both transducers are reconfigured. Specifically, the patch size of MPT and the magnet size of EMAT are carefully selected by numerical and experimental investigations so that the transducer output becomes the largest at a target frequency. By successfully verifying the frequency characteristic, it is shown that the developed transducers can possibly be applied to inspect plate structures as a new and alternative solution instead of conventional Lamb wave transducers.

1.3 Thesis Outline

This thesis presents the new development and characterization of two types of omnidirectional shear-horizontal (SH) wave transducers, a magnetostrictive patch transducer (MPT) and an electromagnetic acoustic transducer (EMAT), respectively, for the inspection of plate structures.

In Chapter 1, the brief explanations on ultrasonic transducers (MPTs and EMATs) and its use for nondestructive evaluation (NDE) and structural health monitoring (SHM) are addressed. The importance of omnidirectional transducers and existing Lamb wave transducers are also introduced. Then, the necessity and significance of the development of new omnidirectional SH wave transducers are highlighted as a research motivation. Moreover, the objectives of this research are summarized with extra explanations on technical issues.

In Chapter 2, *theoretical backgrounds of ultrasonic guided waves and transducers for plate applications are explained.* General information of guided wave based NDE and SHM is described first. Theories of guided waves in plates, Lamb and SH wave modes, are then introduced. By emphasizing the advantages of using SH wave over using Lamb waves for plates, the importance and usefulness of this work are reminded. In addition, fundamental theories for understanding of MPTs and EMATs for SH wave transduction in plate structures are introduced.

In Chapter 3, *the first developed transducer, an omnidirectional SH wave MPT (OSH-MPT) is introduced.* The configuration and working principle of the OSH-MPT are presented. After presenting the evaluation and characterization of the performances of the OSH-MPT installed on a nonferromagnetic plate, such as radiation patterns and mode purity, an application of the OSH-MPT for a ferromagnetic plate is also considered. The issue of magnetic flux leakage on the poor performance of the OSH-MPT installed on a ferromagnetic plate is investigated and the design strategy of the transducer for resolving the issue is proposed.

In Chapter 4, *an omnidirectional SH wave EMAT (OSH-EMAT) for metallic plates, which is a noncontact type transducer, is introduced.* Then, the fundamentals of OSH-EMAT including its configuration and working principle are fully addressed. Through numerical simulations, not only the omnidirectivity of the EMAT is confirmed but the design method for maximizing the transducer sensitivity at a given excitation frequency is proposed. For the demonstration of omnidirectional SH wave transduction using the EMAT and the verification of the proposed design method, experimental studies are also performed in a metallic plate.

In Chapter 5, the overall conclusion of this thesis is presented.

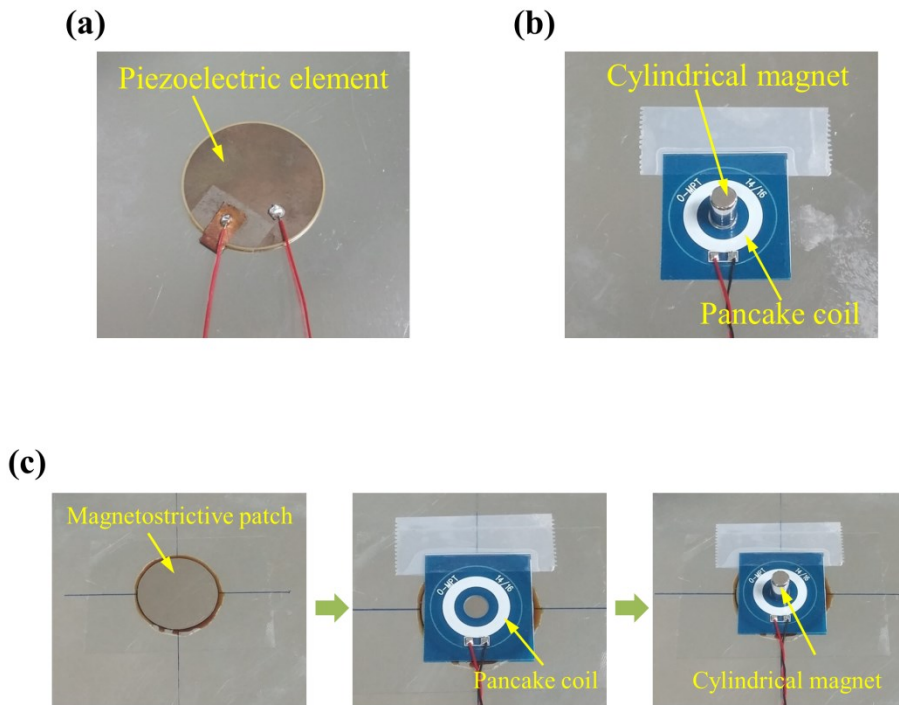


Fig. 1.1 Photos of the previously developed omnidirectional Lamb wave transducers on a plate. (a) A piezoelectric transducer type, (b) an electromagnetic acoustic transducer (EMAT) type and (c) a magnetostrictive patch transducer type, respectively.

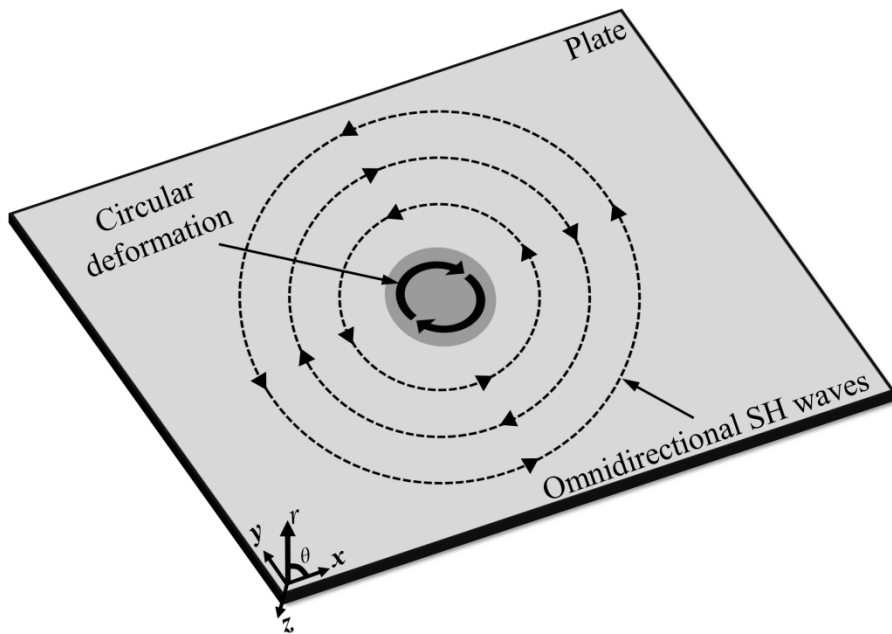


Fig. 1.2 A conceptual drawing of the omnidirectional shear-horizontal (SH) wave generation by a circular deformation in a plate structure.

CHAPTER 2

ULTRASONIC TRANSDUCERS FOR PLATES

2.1 Overview

This chapter presents the theoretical backgrounds that are necessary to understand the general principles and use of ultrasonic guided waves transducers for the inspection of plate structures. In Section 2.2, the concept of nondestructive evaluation (NDE) and structural health monitoring (SHM) of plates using ultrasonic guided waves is introduced. The wave equations of guided wave modes in plate structures (Lamb and shear-horizontal (SH) waves) are also explained and the characteristics of the two wave modes are compared. Then, The advantages of using SH waves for plate applications are drawn by the comparison. Through the Sections 2.3 and 2.4, by introducing the fundamentals of magnetostrictive patch transducers (MPTs) and electromagnetic acoustic transducers (EMATs) for plates, how the SH wave transduction can be achieved by the previously developed MPT and EMAT is described.

2.2 Ultrasonic Guided Waves in Plate Structures

Before explaining ultrasonic guided waves in plates, wave motion in elastic bulk media should be examined first. As shown in Fig. 2.1 (a), there are two bulk wave modes in infinite elastic media: compressional and shear waves [45-47]. By longitudinal excitation of a certain part, compressional waves are generated and the direction of particle motion is the same with that of propagation. It is similar to acoustic wave motion in fluidic media. On the other hand, for shear wave generation, transverse excitation is required so that the motion is perpendicular to the direction of wave propagation. The velocities of two waves are different and these bulk waves have commonly been used for the inspection of structures.

Guided waves are elastic waves that propagate in thin structures such as plates and pipes [45-47]. It is the wave fields formed by the summation of multiple reflected bulk waves from structure boundaries. There are an infinite number of guided wave modes according to structure geometries, excitation frequencies, material properties and so on. Fig. 2.1 (b) sketches guided waves in a plate. Because of the interference of the multiple reflections at the plate boundaries, the incident waves are converted to Lamb and shear-horizontal (SH) waves which are preferred guided waves modes for plates. Various mode shapes are formed along the thickness of plates with respect to wave types. Further details on the guided waves in plates and

the concept of inspection using it will be discussed in the following subsections.

2.2.1 Guided wave based NDE and SHM of plates

Ultrasonic techniques are preferred in the fields of nondestructive evaluation (NDE) and structural health monitoring (SHM) for structures because it is suitable for detecting internal defects and no harmful for structures as well as inspectors [48, 49]. Conventional ultrasonic testing using a bulk wave transducer is depicted in Fig. 2.2 (a). By generating bulk waves at the surface of a structure, one dimensional inspection is achieved. If the transducer position is changed as described in Fig. 2.2 (a), scanning of a structure can be made.

However, using guided wave technique is much useful and efficient to inspect thin and large plate structures. Because guided waves propagate long distance along a plate, it provides rapid scanning of a large plate by a single installation of a fixed transducer as shown Fig. 2.2. (b). In addition, if the transducer is installed on an exposed part of a structure, inaccessible and invisible parts such as buried or hidden parts can be detected [12-14] unlike bulk wave testing. In the guided wave based inspection of plates, therefore, designing guided wave transducers to have great performances and characteristics for certain purposes is important. Note that using a wedge and a commercialized ultrasonic transducer to transmit waves into plate is one of possible methods for guided wave generation as seen in Fig. 2.2 (b).

Piezoelectric transducers, magnetostrictive patch transducers (MPTs) and electromagnetic acoustic transducers (EMATs) are widely used to generate and detect Lamb and shear-horizontal (SH) waves in plate structures. Usually, ultrasonic transducers are used as both transmitters and receivers, respectively. Among these three types of transducers, MPTs and EMATs are known to be easy to generate SH waves by controlling the configuration of the transducers [39, 44]. Since this research is mainly focused on the development of omnidirectional SH wave transducers, MPT and EMAT techniques are considered. (A number of studies on piezoelectric transducers for guided Lamb waves could be found in many previous works such as [50].)

2.2.2 Lamb and shear-horizontal (SH) waves

Lamb and SH waves are guided wave modes in thin plates [45-47] as shown in Figs. 2.3 and 2.4, respectively. There are two Lamb wave modes, symmetric and antisymmetric modes, according to its mode shapes along the thickness. The particle motion of Lamb waves is parallel to the propagation direction (x) and perpendicular to a plate (y) as shown in Fig. 2.3. In other words, Lamb waves contain both in and out of plane deformations. Fig. 2.3 (a) depicts a symmetric Lamb wave mode (S mode) and it is similar to compressional waves in bulk media. Note that the signs of particle motion at top and bottom surface are opposite

because of the symmetric mode shape. An antisymmetric Lamb wave mode (A mode) is also shown in Fig. 2.3 (b) and it acts like bending waves. These two Lamb waves are always coupled and simultaneously excited as long as a special treatment of transducers is not considered.

The vibration of particles by SH waves are only subjected to a plane of the plate surface and its direction is perpendicular to that of wave propagation (i. e. particle motion in z direction only) as shown in Fig. 2.4. Therefore, there is no change of the plate surface position in y direction unlike Lamb waves.

To understand the mechanics of Lamb and SH waves with theoretical details, the dispersion relation (frequency-wavenumber) for each wave mode should be considered. To this end, the theories for elastic wave motion in [46] are explained here.

The well-known governing equation for stress wave motion in homogeneous isotropic elastic media (Navier's equation in a vector form) is

$$(\lambda + \mu)\nabla\nabla \cdot \mathbf{u} + \mu\nabla^2 \mathbf{u} = \rho\ddot{\mathbf{u}}. \quad (2.1)$$

The symbols \mathbf{u} and ρ denote the displacement field and the density of the

media, respectively. The symbols λ and μ represent Lamé constants. The displacement field of Eq. (2.1) is obtained using the Helmholtz decomposition consisting of a scalar potential (ϕ) and a vector potential ($\boldsymbol{\psi}$) as

$$\mathbf{u} = \nabla\phi + \nabla \times \boldsymbol{\psi} . \quad (2.2)$$

Because ϕ and $\boldsymbol{\psi}$ are independent to each other, by substituting Eq. (2.2) into Eq. (2.1), a scalar equation for dilatation waves and a vector equation for shear waves, respectively, are obtained as

$$\nabla^2\phi = \frac{1}{c_d^2} \ddot{\phi} , \quad = \sqrt{\frac{\lambda+2\mu}{\rho}} , \quad (2.3)$$

$$\nabla^2\boldsymbol{\psi} = \frac{1}{c_s^2} \ddot{\boldsymbol{\psi}} , \quad = \sqrt{\frac{\mu}{\rho}} . \quad (2.4)$$

Note that c_d and c_s denote the dilatation and shear wave speeds, respectively.

Now, the Lamb wave in a plate having the thickness $2b$ is considered as shown in Fig. 2.3. The angular frequency and wavenumber of the waves will be denoted by ω and k , respectively. The resulting potentials and the displacement field components by Eqs. (2.2)-(2.4) according to the coordinate system in Fig. 2.3 will

be

$$\phi = (A_1 \sin \xi y + A_2 \cos \xi y) e^{j(kx - \omega t)}, \quad (2.5)$$

$$\psi = j(A_3 \sin \chi y + A_4 \cos \chi y) e^{j(kx - \omega t)}, \quad (2.6)$$

$$u_x = j\{k(A_1 \sin \xi y + A_2 \cos \xi y) + \chi(A_3 \cos \chi y - A_4 \sin \chi y)\} e^{j(kx - \omega t)}, \quad (2.7)$$

$$u_y = \{\xi(A_1 \cos \xi y - A_2 \sin \xi y) + k(A_3 \sin \chi y + A_4 \cos \chi y)\} e^{j(kx - \omega t)}, \quad (2.8)$$

where

$$\xi = \sqrt{\frac{\omega^2}{c_d^2} - k^2} \quad \text{and} \quad \chi = \sqrt{\frac{\omega^2}{c_s^2} - k^2}. \quad (2.9)$$

Then, by using the well-known stress-displacement relation in the elasticity theory, the stress field components are given by

$$\sigma_{yy} = \mu[\{2k^2 - \nu^2(k^2 + \xi^2)\}(A_1 \sin \xi y + A_2 \cos \xi y) + 2\chi k(A_3 \cos \chi y - A_4 \sin \chi y)] e^{j(kx - \omega t)}, \quad (2.10)$$

$$\sigma_{xy} = j\mu\{2\xi k(A_1 \cos \xi y - A_2 \sin \xi y) - (\chi^2 - k^2)(A_3 \sin \chi y + A_4 \cos \chi y)\} e^{j(kx - \omega t)}, \quad (2.11)$$

where

$$v = \frac{c_s}{c_d} = \sqrt{\frac{\lambda + 2\mu}{\mu}}. \quad (2.12)$$

If the traction free boundary condition (say, $\sigma_{yy} = \sigma_{xy} = 0$) at the top and bottom surfaces of the ($y = \pm b$) is applied to Eqs. (2.10) and (2.11), the frequency equations, widely known as the Rayleigh-Lamb wave equation, are obtained for symmetric and antisymmetric wave modes as

$$\frac{\tan \chi b}{\tan \xi b} = -\frac{4\xi\chi k^2}{(k^2 - \chi^2)^2} \quad \text{for symmetric wave modes,} \quad (2.13)$$

$$\frac{\tan \chi b}{\tan \xi b} = -\frac{(k^2 - \chi^2)^2}{4\xi\chi k^2} \quad \text{for antisymmetric wave modes.} \quad (2.14)$$

Note that Eqs. (2.13) and (2.14) will also be referred as the dispersion relation or $\omega - k$ (frequency-wavenumber) relation for the Lamb waves in this study.

In case of SH waves, the coordinate system in Fig. 2.4 is considered. In this case, the governing wave equation and the corresponding displacement field will simply be

$$\nabla^2 u_z = \frac{1}{c_s^2} \ddot{u}_z, \quad (2.15)$$

$$u_z = (B_1 \sin \chi y + B_2 \cos \chi y) e^{j(kx - \omega t)}. \quad (2.16)$$

By applying the traction free condition ($\sigma_{yy} = \sigma_{xy} = 0$) and the SH wave restriction condition $\frac{\partial u_z}{\partial y} = 0$ at $y = \pm b$ to Eq. (2.16), the following equations can be obtained as

$$B_1 \cos \chi b - B_2 \sin \chi b = 0, \quad B_1 \cos \chi b + B_2 \sin \chi b = 0, \quad (2.17)$$

and it gives

$$\cos \chi b \sin \chi b = 0. \quad (2.18)$$

Accordingly, Eq. (2.18) satisfies the following condition as

$$\chi b = \frac{n\pi}{2} \quad (n = 0, 1, 2, 3, \dots), \quad (2.19)$$

which is the frequency equation for SH wave in a plate. Considering the definition of χ in Eq. (2.9), Eq. (2.19) can be rewritten as

$$\left(\frac{\omega b}{c_s}\right)^2 = \left(\frac{n\pi}{2}\right)^2 + k^2 b^2 \quad (n = 0, 1, 2, 3, \dots). \quad (2.20)$$

By using Eqs. (2.13), (2.14) and (2.20), the dispersion curves of Lamb and SH waves for an aluminum plate can be plotted as shown in Fig. 2.5. Note that it is expressed by the frequency*plate thickness and phased velocity. Theoretically, there is an infinite number of Lamb and SH wave modes as the frequency or the thickness of plate increases. Note that the phase velocity represents the slope of the frequency-wavenumber relation. If a guided wave mode is dispersive, its phase velocity is not a constant value according to frequencies. It means that the wave packet of a dispersive guided wave mode can be distorted after propagation because of different values of velocity components at a given frequency band. Fig. 2.6 compares the measured signals of dispersive and nondispersive waves. While the waveform of the first arrival of dispersive wave is distorted and lengthen in time axis (see the dotted circle in Fig. 2.6 (a)), in the case of nondispersive wave (see the dotted circle in Fig. 2.6 (b)), the waveform of first arrival signal is clearly measured without any distortion. It is observed that only the fundamental mode of SH wave (SH0 mode) is nondispersive although all other Lamb and SH waves are dispersive as shown in Fig. 2.5. This feature of SH0 wave mode in plates will be more discussed in the following subsection to emphasis the advantage of using SH waves.

2.2.3 Advantages of using SH waves over Lamb waves

Even though Lamb waves are widely used for plate inspections, there are several disadvantages inherent in using Lamb waves such as dispersion, multiple mode excitation and attenuation by loadings on plates. However, these disadvantages of using Lamb waves can be avoided or overcome by using SH waves as an alternative method. To explain the details on this, the advantages of SH waves over Lamb waves are addressed and compared as follows:

First, a nondispersive wave mode (SH0 mode) can be used to inspect plates unlike using Lamb wave modes. As mentioned above, only the SH0 mode is nondispersive among all guided wave modes in plates. Fig. 2.5 (a) is the dispersion curve of Lamb waves and it is seen that all Lamb waves are dispersive. Some of them at certain frequencies are highly dispersive, which should be avoided for more accurate inspections. Because the waveform of dispersive waves is distorted as seen in Fig. 2.6, a signal processing technique such as the dispersion compensation [51] is needed to reconstruct the original signal from the measured dispersive signal. However, if the SH0 mode is used instead of Lamb waves, more accurate inspections can be made without any dispersion compensation technique.

Second, a single mode excitation is possible at a relatively low frequency range by

using *SH waves*. As shown in Fig. 2.5 (a), more than two Lamb wave modes are always generated in all frequency range. Because of the excitation of multiple Lamb waves, the mutual interference between them occurs which negatively influences on the inspection results [52]. In SH wave case, however, only a single SH₀ mode exists at a low frequency range (less than the first cutoff frequency of SH waves) as seen in Fig. 2.5 (b). Therefore, if the SH wave at this frequency range is chosen to inspect plates, the problem caused by the excitation of multiple modes in using Lamb waves can be avoided.

Third, because the particle motion of SH waves is only in-plane motion as shown in Fig. 2.4, it is less influenced by arbitrary loadings on plates. In practical situations, plate structures are subjected to various loadings such as fluid, soil and other mechanical parts. If the direction of particle motion is normal to a plate like Lamb wave motion, it is highly attenuated by loadings on a plate. On the contrary, the vibration of particle by SH waves are only parallel to a plane of a plate. So, SH waves are not affected by the loading on a plate and thus propagate long distance more effectively comparing to Lamb waves

To sum up, by using SH waves instead of Lamb waves, not only a single and nondispersive mode can only be used but more effective inspections of long and large plate area are possible unlike Lamb wave based inspections.

2.3 Magnetostrictive Patch Transducer (MPT)

Magnetostrictive patch transducers (MPTs) are known to be useful to generate and measure guided waves in pipe [53-59] and plate structures [40-43, 60-65]. It is highly sensitive, cost-effective and easy to induce shear deformations of magnetostrictive patches. In the configuration of a MPT for a plate structure, a thin magnetostrictive patch bonded onto a plate is subjected to static and dynamic magnetic fields. Therefore, the patch deforms by magnetostriction effect which is a coupling phenomenon between magnetic and mechanical fields in ferromagnetic materials [36-38]. The patch is bonded onto a plate by bonding material and thus the deformation of the patch is transferred to guided waves in a plate. While MPTs have several advantages for plate applications, its mechanism is quite complicated to be fully analyzed. Hence, it is important to understand the principle of magnetostriction and how to configure MPTs for the SH wave transduction.

2.3.1 Magnetostriction

When a magnetic field is applied to a ferromagnetic material such as iron, nickel, cobalt and alloys based on them, it deforms and produces a mechanical strain by magnetostrictive effect or Joule effect [66, 67]. The generated strain is usually referred as magnetostriction. On the contrary to this, if a ferromagnetic material is deformed by a mechanical input, as a result of the reciprocity, it generates the

change of magnetic induction of material. This phenomenon is called the inverse magnetostriction or Villari effect [68].

The magnetostrictive effect in macroscopic level is described in Fig. 2.7. (Its behavior in microscopic level is beyond the scope of this research.) The randomly disordered magnetic domain walls are rotated as a response to an external magnetic field. As a result of this, the change of the domain orientation and dimension of a ferromagnetic material in turn occur. Therefore, the physical length change of a ferromagnetic material is induced by the magnetostrictive effect as shown in Fig. 2.7.

The magnetostrictive effect and its inverse phenomenon can be interpreted and analyzed by the following equations [44, 69, 70-72]

$$\varepsilon = \frac{\sigma}{E^H} + qH, \quad (2.21)$$

$$B = q^* \sigma + \mu^\sigma H, \quad (2.22)$$

where the symbols ε , σ , H and B represent the strain, the stress, the magnetic field and the magnetic flux density, respectively. The symbols for material constants E^H , q , q^* and μ^σ are the Young's modulus under a constant magnetic field, the coupling coefficient of the magnetostrictive effect, the

coupling coefficient of the inversed magnetostrictive effect and the permeability under a constant stress, respectively. The detailed explanations on Eqs. (2.21) and (2.22) are addressed in Appendix A with the piezomagnetic theory [44].

Although the piezomagnetic theory is well developed, the analysis of MPTs using the theory is still cumbersome because of the nonlinear properties of magnetostrictive materials. For example, the two graphs in Fig. 2.8 represent the nonlinear features of a pure nickel. Fig. 2.8 (a) shows the sensitivity of a nickel expressed by a magnetostriction (λ) and a magnetic field (H). This relation is commonly called $\lambda-H$ curve. As shown in Fig. 2.8 (a), if the enough static magnetic field (H_s) for biasing and the dynamic magnetic field (H_{D1}) for actuation are applied to a magnetostrictive material, a substantially stronger strain at a locally linear range (λ_{D1}) can be generated comparing to the operation at the origin of the curve. Even if stronger dynamic magnetic field (H_{D2}) is applied to the material, the induced strain (λ_{D2}) is small due to the nonlinear characteristic. Therefore, supplying a static magnetic field strong enough to bias operating range at a locally linear area should be performed first before actuating MPTs for wave transduction. Furthermore, a magnetization curve ($B-H$ curve) of a ferromagnetic material is nonlinear hysteresis loops as shown in Fig. 2.8 (b). So, to fully analyze the behavior of MPTs, these nonlinear properties of magnetostrictive materials should be considered with the piezomagnetic theory together.

2.3.2 MPTs for SH wave transduction

In this subsection, the configuration of a SH wave MPT is presented. To generate shear deformations of a patch, a magnetic circuit formed by static and dynamic magnetic fields is needed. Fig. 2.9 shows the deformations of a magnetostrictive patch according to the different magnetic circuits. For Lamb wave generation by a MPT, the static and dynamic magnetic fields are applied to the patch in the same direction as shown in Fig. 2.9 (a). This generates the longitudinal deformation of the patch. Note that Fig. 2.9 is sketched for a pure nickel case which is a negative magnetostrictive material. In case of the shear deformation, as shown in Fig. 2.9 (b), the applied static and dynamic magnetic fields are mutually perpendicular each other. By doing so, the shear deformation of the patch is generated, which is referred to as Wiedemann effect [73].

Fig. 2.10 is a schematic configuration of a SH wave MPT installed on a plate. A pair of rectangular magnets are placed each side of the patch in opposite polarizations to produce a static magnetic field in a certain direction and an AC current carrying wire is placed on the patch to generate a dynamic magnetic field in the orthogonal direction to that of a static magnetic field. Then, SH waves are generated as a response to the shear deformation of the patch by the applied static and dynamic magnetic fields.

2.4 Electromagnetic Acoustic Transducer (EMAT)

Ultrasonic transducers operated by the Lorentz force mechanism [44] are referred to as electromagnetic acoustic transducers (EMATs) and widely used in many industrial fields. EMATs do not require any physical contact to transmit waves into media, so it allows the noncontact transduction of elastic waves in metallic structures. This noncontact feature of EMATs is a powerful advantage over other ultrasonic transducers. Hence, various EMAT configurations are commercialized [74] and its many applications are performed [75-79] by slightly lifting off the vertical position of EMAT from structures. On the other hand, the signal to noise ratio (SNR) of the generated waves by EMATs is relatively lower than that of other transducers. For instance, if a MPT and an EMAT are installed on a plate using the same experimental setup, the amplitude of the generated wave mode signal by an EMAT is much smaller than the signal by a MPT. More specifically, to obtain the similar amplitude of the desired wave mode using an EMAT (SNR is still low), some amplification in the connected electronic equipment is needed. Furthermore, there are other several issues on the SNR performance of EMATs such as lift-off distance, skin effect, impedance matching and so on. By considering these issues in the design process of EMATs, the SNR performance of EMATs can be improved.

The Lorentz force mechanism, which is a key principle of EMAT operation, is a

result of the interaction between static magnetic fluxes and eddy currents on a metallic plate. Accordingly, understanding of the Lorentz force mechanism is important to design EMATs and its reversal effect, the inversed Lorentz force mechanism, should also be considered when EMATs operating as wave sensors.

2.4.1 Lorentz force mechanism for EMATs

Fig. 2.11 depicts the general principle of an EMAT installed on a metallic plate. EMATs consist of permanent magnets to supply static magnetic fluxes and AC current carrying coils to induce eddy currents on a plate. Because the working mechanism of EMATs is also based on an electromagnetic effect (Lorentz force) like MPTs (Magnetostrictive effect), it is noted that the main components (magnets, coils) of EMATs are similar to that of MPTs except patches. The Lorentz force is a result of the cross product between eddy currents and static magnetic fluxes, which can be expressed [44] as

$$\mathbf{f} = \mathbf{i}^e \times \mathbf{B}^s . \quad (2.23)$$

The symbols \mathbf{f} , \mathbf{i}^e and \mathbf{B}^s denote the Lorentz force, the induced eddy current and the static magnetic flux density, respectively. For example, in the EMAT configuration shown in Fig. 2.11, the static magnetic flux in z direction and the eddy current in x direction generate the Lorentz force in y direction mainly. Note

that the Lorentz force mechanism is a linear relation as expressed in Eq. (2.23), so its analysis is much easier than MPTs. Eq. (2.23) is usually considered for the design of EMAT transmitters to generate waves. As a reciprocal effect of Eq. (2.23), the inversed Lorentz force mechanism for a receiving EMAT can also be expressed as [44]

$$\mathbf{J} = \eta(\mathbf{v} \times \mathbf{B}^s), \quad (2.24)$$

where \mathbf{J} , \mathbf{v} and η represent the induced current density in a receiving EMAT, the particle velocity and the electrical conductivity of a plate, respectively. By measuring \mathbf{J} in a coil of a receiving EMAT, waveforms of guided waves in plates can be recorded.

2.4.2 EMATs for SH wave transduction

To generate SH waves using an EMAT, a pair of Lorentz forces in opposite direction is required as shown in Fig. 2.12. This is a conventional EMAT for SH wave generation that consists of a pair of rectangular magnets with different polarizations and an AC current carrying coil. The two rectangular magnets produce the static magnetic fluxes in z direction with the different signs and the coil causes the eddy currents on a plate in x direction. Therefore, the Lorentz forces are generated in y direction. Note that the directions of the generated Lorentz forces

underneath each magnet are opposite each other because of the arrangement of different magnet poles. By the Lorentz forces in y direction, SH waves are generated and propagated in x direction as shown in Fig. 2.12. This is suitable for generating SH waves in a certain direction (unidirectional). It is noted that the Lorentz force is mainly generated on the surface of the plate due to the skin depth. Although there may exist trivial Lorentz forces in other directions (not y direction) due to the irregularities of the static magnetic fluxes and eddy currents, it is generally negligible in practical use.

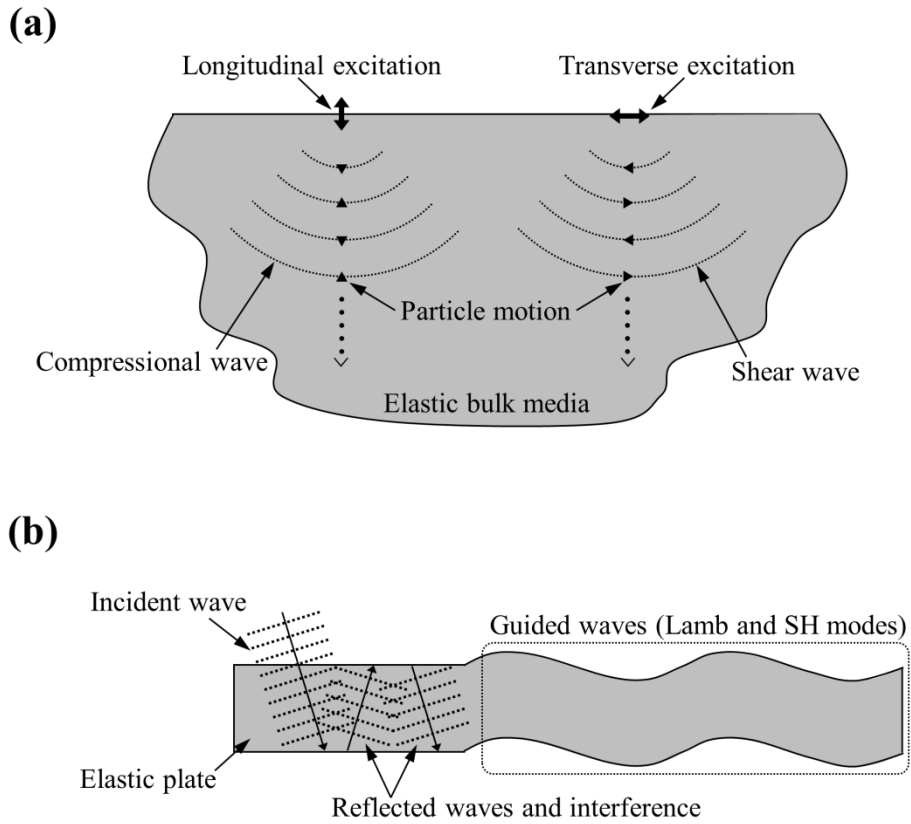


Fig. 2.1 Schematic drawings of the generation of (a) bulk waves (Compressional and shear waves) in an elastic bulk media and (b) guided waves (Lamb and shear-horizontal waves) in an elastic plate.

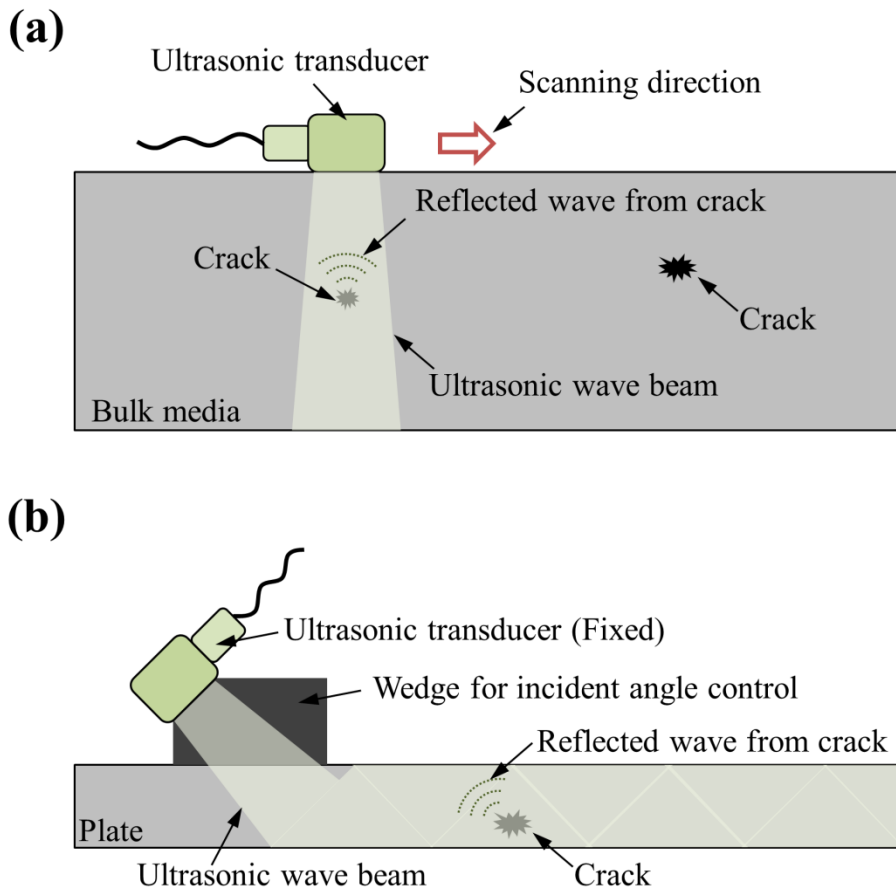
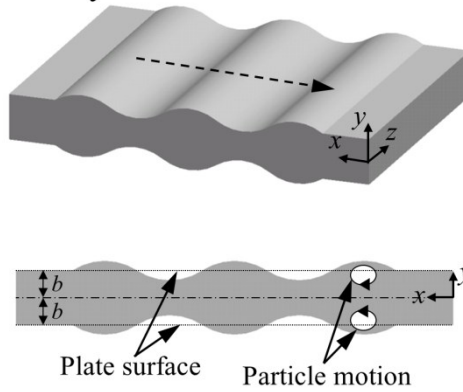


Fig. 2.2 Illustrations of ultrasonic inspections using (a) bulk elastic waves and (b) guided waves.

(a)

Symmetric Lamb wave



(b)

Antisymmetric Lamb wave

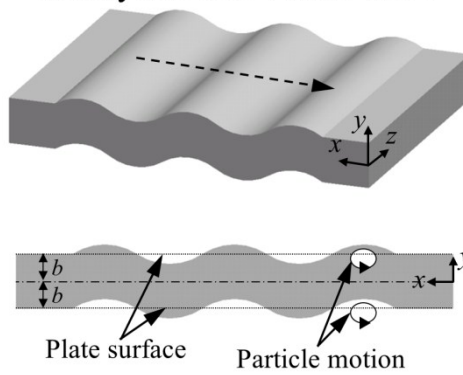


Fig. 2.3 Lamb wave propagation in an elastic plate and the designated coordinate systems for (a) a symmetric mode and (b) a antisymmetric mode with the mode shapes along the plate thickness.

Shear-horizontal (SH) wave

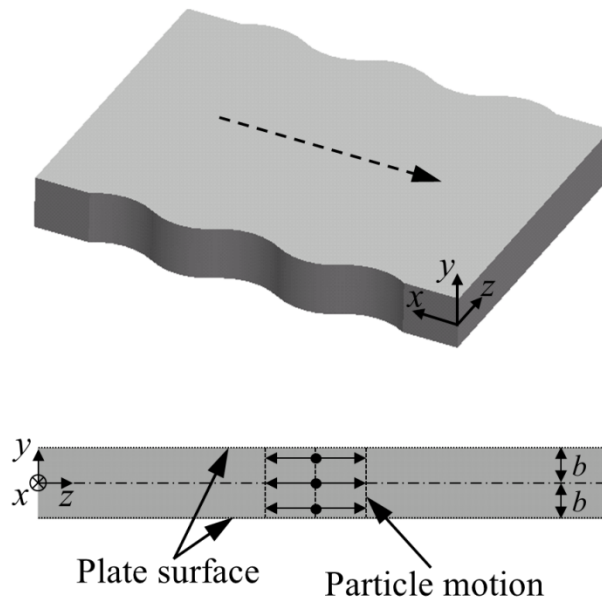


Fig. 2.4 Shear-horizontal (SH) wave propagation in an elastic plate. The particle motion is only in the z direction and there are no deformations in y direction on the top and bottom surfaces of the plate.

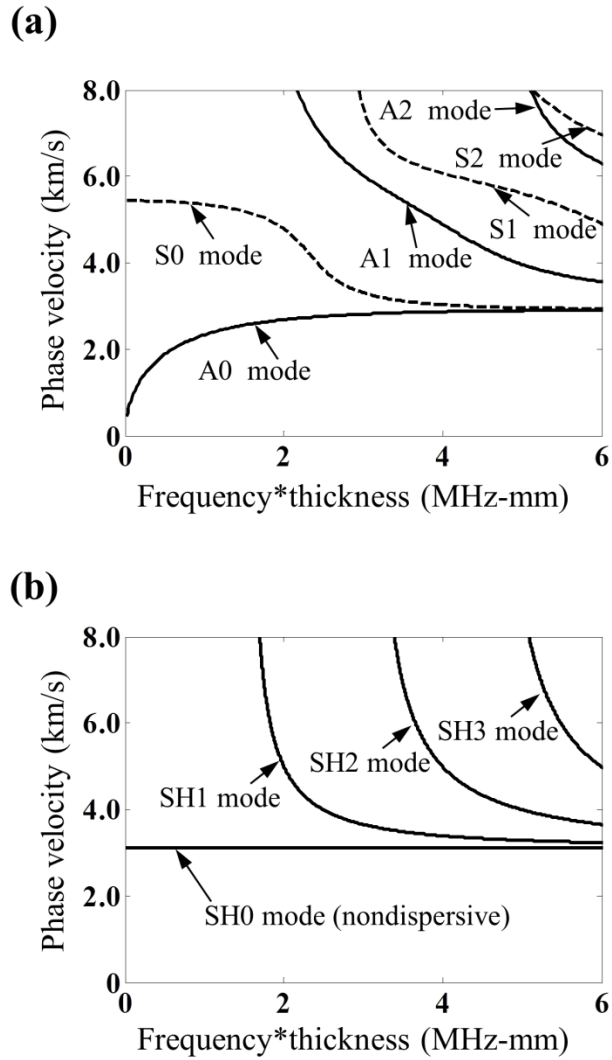


Fig. 2.5 The dispersion curves of (a) Lamb waves and (b) SH waves for an aluminum plate. The horizontal axis represents the frequency*thickness while the vertical axis represents the phase velocity.

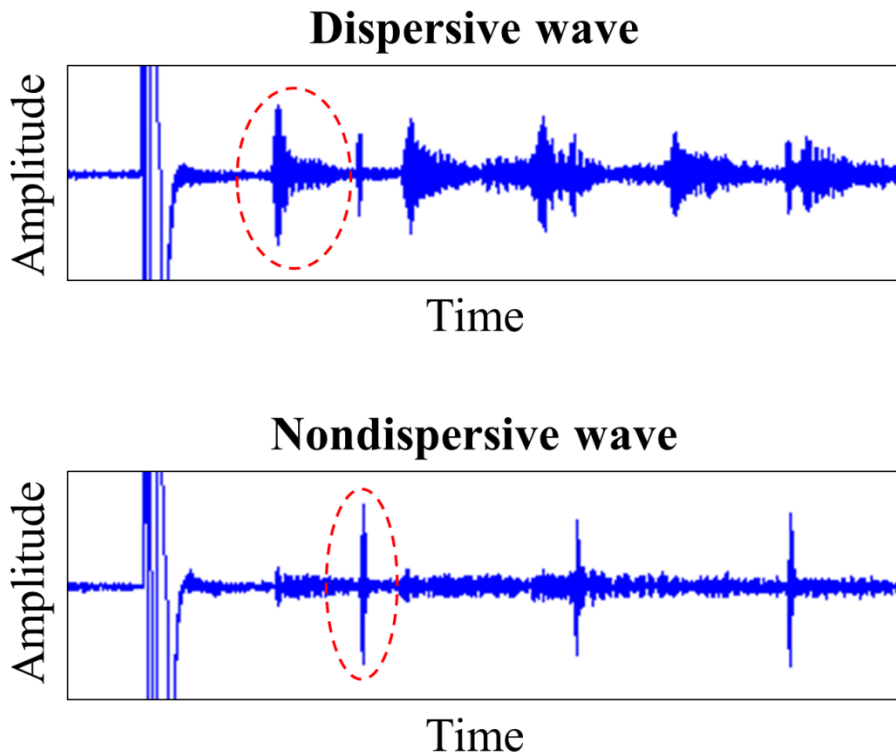


Fig. 2.6 Measured guided wave signals. (a) A dispersive wave signal and (b) a nondispersive wave signal. The waveform of the first arrival in a dispersive wave is distorted due to various velocity components.

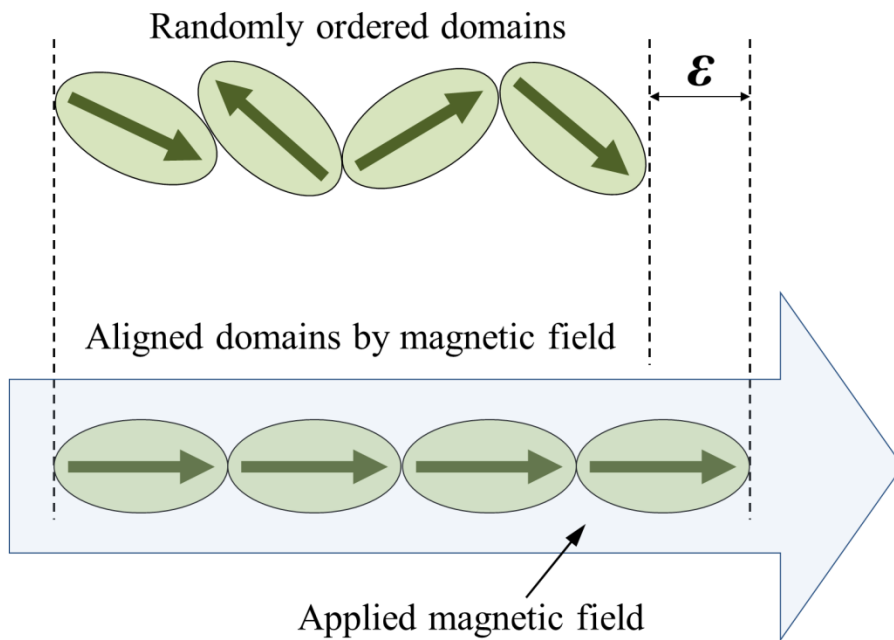


Fig. 2.7 Illustration of the magnetostrictive effect of a ferromagnetic material. The disordered magnetic domains are aligned and rotated by the applied magnetic field and thus the mechanical strain (magnetostriction) of the material is generated.

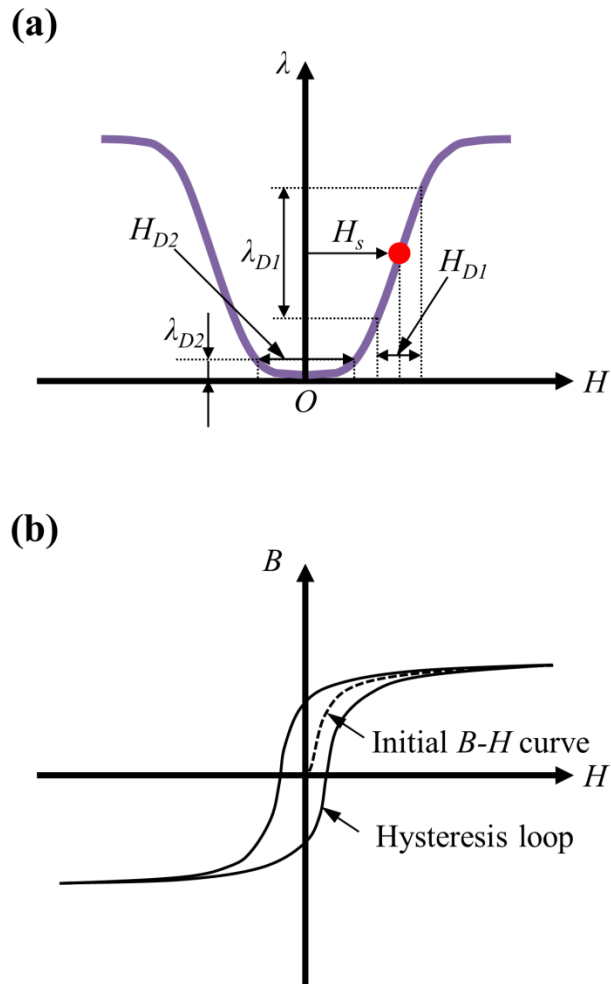
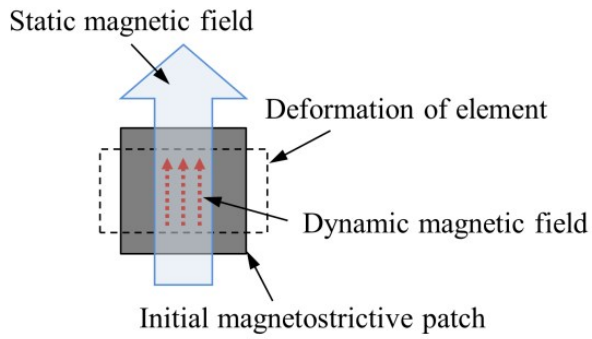


Fig. 2.8 (a) Nonlinear magnetostriction curve and (b) magnetization curve of a magnetostrictive material (pure nickel) with a hysteresis property.

(a)



(b)

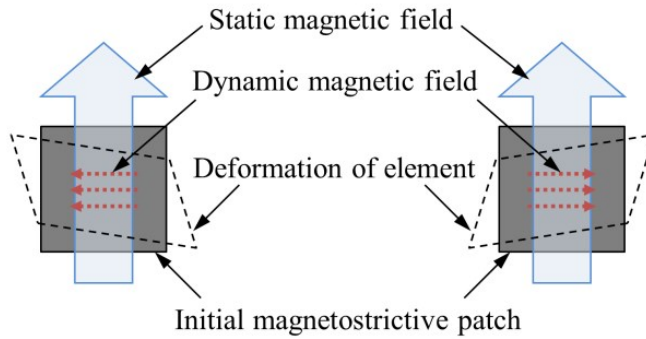


Fig. 2.9 Illustrations for deformation of a magnetostrictive patch by the induced magnetostriction. (a) Static and dynamic magnetic fields are applied to a patch in the same direction for Lamb wave generation while (b) two fields are orthogonally applied to a patch for SH wave generation.

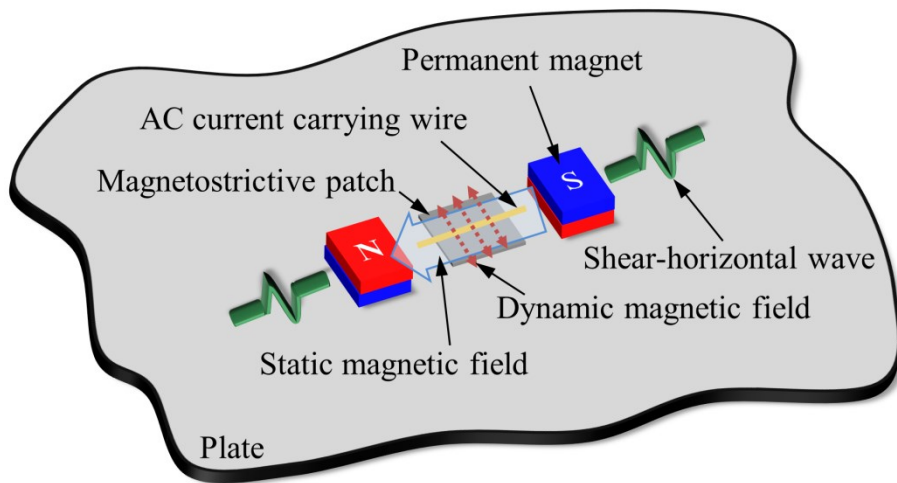


Fig. 2.10 Schematic configuration of a SH wave MPT operating on a plate. The static magnetic field by the magnets is perpendicular to the dynamic magnetic field by the coil and the two fields are directly applied to the patch.

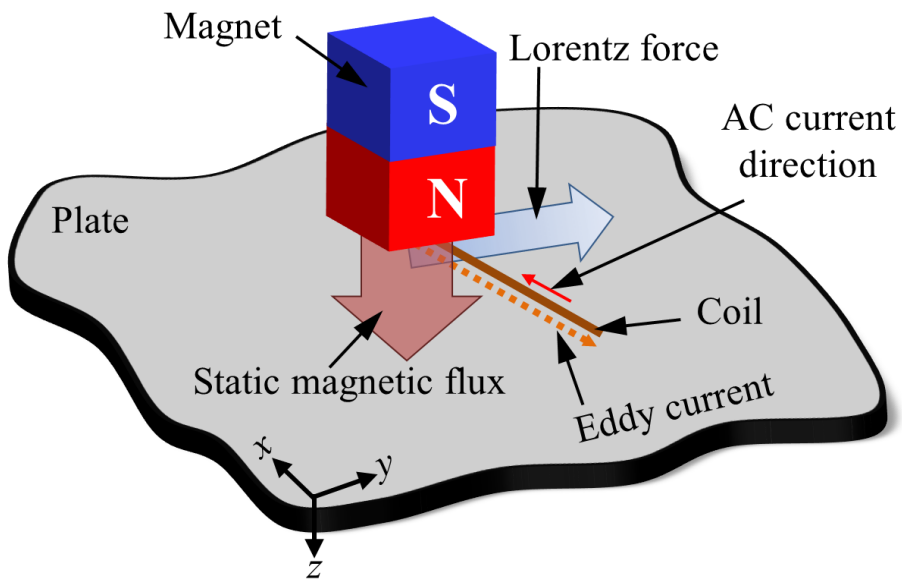


Fig. 2.11 Lorentz force generation by an electromagnetic acoustic transducer (EMAT) consisting of a magnet and a coil on a metallic plate. The cross product of the induced eddy current by the coil and the static magnetic flux from the magnet produces the Lorentz force acting on the plate.

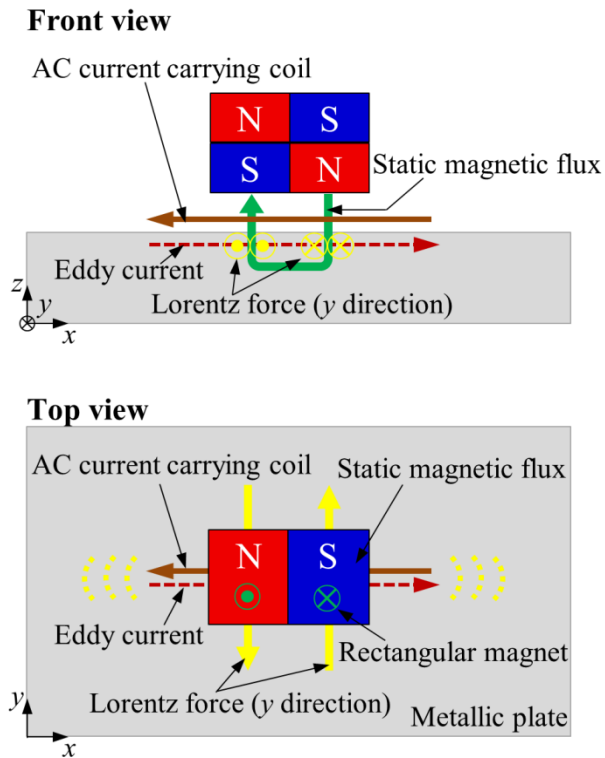


Fig. 2.12 Schematic configuration of a SH wave EMAT acting on a metallic plate. The EMAT consists of a pair of magnets having different magnetic polarities and a coil. The resulting Lorentz force by the EMAT generates SH waves dominantly in x direction.

CHAPTER 3

OMNIDIRECTIONAL SHEAR-HORIZONTAL WAVE MAGNETOSTRICTIVE PATCH TRANSDUCER (OSH-MPT)

3.1 Overview

As a useful tool to inspect large plate structures using ultrasonic waves, various omnidirectional guided wave transducers have become more widely used to form phased array systems. While many kinds of omnidirectional Lamb wave transducers have been developed and utilized in the phased array systems, there has been no research on the development of omnidirectional shear-horizontal (SH) wave transducers so far. Therefore, in this chapter, an omnidirectional SH magnetostrictive patch transducer (OSH-MPT) is newly proposed. It consists of a thin annular magnetostrictive patch, a specially wound coil and a cylindrical permanent magnet.

After explaining the configuration of the OSH-MPT and its working mechanism, the omnidirectional SH wave transduction using the developed transducer is performed by experiments in a nonferromagnetic (aluminum) plate. Then, the omnidirectivity of the generated SH waves by the OSH-MPT is confirmed by measuring the radiation pattern through numerical simulations and experiments. In addition, the frequency characteristic of the developed transducer depending on the dimension of the patch are experimentally investigated considering the practical use for the construction of a SH wave based phased array system. The effect of static magnetic field strength on the variation of OSH-MPT sensitivity is examined as the underlying reference data.

Furthermore, omnidirectional shear-horizontal wave transduction is performed using the developed OSH-MPT in a ferromagnetic plate which is a quite common structural component. In case of a ferromagnetic plate, unavoidable magnetic flux leakage into the plate not only makes transduction efficiency poor but also generates unwanted wave modes in the plate. Therefore, these problems must be overcome in order to generate omnidirectional SH waves in ferromagnetic plates by using the transducer. In the related sections, the reason for the poor performance of the magnetostrictive patch transducer is investigated when it is installed on a ferromagnetic plate. Moreover, a method to improve its performance is suggested. The effectiveness of the proposed methods is validated through numerical simulations and experiments. The experiments are conducted at several excitation

frequencies by using the transducers of different sizes installed on a ferromagnetic plate

In this chapter, the development of OSH-MPT for a nonferromagnetic and a ferromagnetic plate, respectively, is mainly carried out. The various performances of the OSH-MPT are evaluated and the methods to optimally configure the transducer for each case are also proposed. The results in this chapter will be helpful to form phased array system using OSH-MPTs for practical purposes.

3.2 Development of OSH-MPT

The use of omnidirectional guided wave transducers is very effective for structural health monitoring (SHM) or nondestructive evaluation (NDE) of large plate structures when the phased array system is formed by the transducers. Various omnidirectional guided wave transducers have been developed and employed in the inspection systems for plates [18, 80-83], they all use only omnidirectional Lamb wave transducers. However, no omnidirectional shear-horizontal (SH) wave transducer has been considered so far. Therefore, considering the first development and the advantages of using SH wave as discussed in Subsection 2.2.3, it is worth proposing an omnidirectional SH wave transducer. To take the advantage of using the nondispersive fundamental SH wave mode [46], the transducer should be designed to be operated at a frequency range less than the first cutoff frequency of

SH waves for a given plate.

Because transducers are a key element of a phased array system, this section deals with the development of an omnidirectional SH wave transducer which can be used for plate inspection. In doing so, the use of the magnetostrictive phenomenon [36, 38] is considered. It refers to the phenomenon that when magnetic fields are applied to magnetostrictive (ferromagnetic) materials, the corresponding mechanical deformations are induced in the materials. If the static and dynamic magnetic fields are applied mutually perpendicular directions to a magnetostrictive material, the shear deformation of the material occur by Wiedemann effect [73]. While there were some previous works to generate and measure SH waves in structures [43, 59, 84-86] using the Wiedemann effect, no omnidirectional SH wave transduction has been made. Hence, the new development of an omnidirectional SH wave transducer is challenging and meaningful.

3.2.1 Configuration and working mechanism

Fig. 3.1 (b) schematically shows the configuration of the developed omnidirectional shear-horizontal wave magnetostrictive patch transducer (OSH-MPT). Because the details of the transducer will be addressed later, the main components of the developed OSH-MPT are pointed out first: A) a thin annular magnetostrictive patch inner and outer radii of which are determined by the

wavelength of an excited shear-horizontal wave as shown in Fig. 3.1 (a); B) a toroidally wound coil over the patch using a special winding strategy and C) a vertically polarized cylindrical permanent magnet. While the wound coil provides the circumferential dynamic magnetic field to the magnetostrictive patch, the permanent magnet supplies the static magnetic field in the radial direction. Using the OSH-MPT in Fig. 3.1 (b), experiments in a 1 mm thick aluminum plate are carried out to confirm the transduction of the desired SH wave mode and the omnidirectional radiation patterns of the transducer. The experimental results will be compared with numerical simulation results. The frequency characteristics of the OSH-MPT will also be investigated by experiments conducted using the OSH-MPT formed by magnetostrictive patches of different sizes.

The detailed configuration of the developed OSH-MPT is as follows. A thin annular magnetostrictive patch is made of a 0.15 mm thick patch (pure nickel). The inner (r_i) and outer (r_o) radii of the patch, as indicated in Fig. 3.1 (a), so selected that $r_o - r_i = \lambda / 2$ where λ is the wavelength of the fundamental SH wave mode (SH0 mode) at a target excitation frequency and thus the resulting radii should be $r_i = \lambda / 4$ and $r_o = 3\lambda / 4$. Because the annular nickel patch will generate shear strains of the same sign for the magnetic circuit formed by the magnet and the coil, it is important to have the maximum displacements at the inner and outer circumferences of the patch. (The explanations on the magnetic

circuit will be given later.) Accordingly, the choice of $r_o - r_i = \lambda / 2$ satisfies that the largest displacements in the circumferential direction occur on the inner and outer circumferences of the annular patch, respectively, by the constructive interference. In other words, the maximum SH wave can be generated if the geometry of the patch is selected to ensure the relation $r_o - r_i = \lambda / 2$. This argument will be checked experimentally in Subsection 3.3.3. Similar approaches to design SH wave MPTs were successfully employed in earlier researches [40, 56].

Now, the explanation on the magnetic circuit of the OSH-MPT is addressed. The applied static and dynamic magnetic fields to the magnetostrictive patch should be perpendicular to each other to generate a shear deformation in the patch by the Wiedemann effect. First, a cylindrical permanent magnet, polarized in the vertical direction, is placed right above the center of the annular patch in order to supply the radial static magnetic field to the patch. In general, the amplitude of the generated SH wave by MPTs are highly depends on the strength of applied static magnetic field strength because of the nonlinear feature of the magnetostrictive phenomenon as discussed in Chapter 2. (More detailed research on the strength of the applied static magnetic field to MPTs is presented in Appendix A.) Considering this fact, in the case of the developed OSH-MPT, the permanent magnet should be properly located above the patch to supply the optimal static magnetic field to the patch. By doing so, the sensitivity of the OSH-MPT can be maximized.

Second, a coil is used to supply a circumferential dynamic magnetic field to the patch (i.e. orthogonally to the static magnetic field). To supply a circumferential dynamic magnetic field to the patch by the coil, the coil must be radially wound on the patch like toroidal coils. To wind the coil in the radial direction with each turn spaced at an equal distance in the circumferential direction, a thin annular plastic hosting plate, slightly larger than the annular patch, is fabricated to have the notches at the intended locations along the inner and outer circumferences of the patch. The hosting plate is placed on the patch and tightly attached with some sticky material. The coil wound around the patch will be simply called as the toroidal coil. The special strategy of coil winding for the toroidal coil will be introduced in the next subsection.

The fabrication process of the OSH-MPT is depicted in Fig. 3.2. The patch and the hosting plate in Fig. 3.2 (a) is attached each other first. Then, the coil is wound along the patch as shown in Fig. 3.2 (b). (The details on the coil winding will be discussed in the following subsection.) By connecting the coil to the electrical terminal and placing the magnet, the OSH-MPT is finally made (see Figs. 3.2 (c) and (d)).

3.2.2 Coil winding strategy

For coil winding in order to yield as uniform circumferential dynamic magnetic field as possible, some special efforts are conducted. As indicated in Fig. 3.3, there are $2n$ sets of evenly spaced notches fabricated in the thin hosting plate along its inner and outer circumferences, respectively, each set marked with N_i and N'_i ($i = 1, 2, 3, \dots, 2n-1, 2n$). The initial winding of the coil is made by connecting odd sets of notches, N_{2j-1} and N'_{2j-1} ($j = 1, 2, \dots, n$) in the radial direction. In doing so, the coil passes over the outer circumference of the thin hosting plate between N_{2j-1} and N_{2j} ($j = 1, 2, \dots, n$) and also passes under it between N_{2j} and N_{2j+1} . By doing so, the directions of currents flown in all of coil segments placed over or under the patch can become the same as shown in Fig. 3.3. After completing the coil winding with the odd sets of notches (Step 1 in Fig. 3.3), winding is continued radially using even sets of notches ((N_{2j}, N'_{2j}) , ($j = 1, 2, \dots, n$)). This is Step 2. At this time, between Step 1 and 2, the roles of even notches and odd notches are interchanged for the extension of the radial coil winding in the circumferential direction.

While the figure of Step 1 in Fig. 3.3 depicts the direction of coil flow in the coil and the circumferential dynamic magnetic field generated by the current, the figure of Step 2 in Fig. 3.3 shows the final current directions in the coil wound over the

patch and the total induced dynamic magnetic field in the circumferential direction. The angle θ_s between two consecutive radially wound coil segments is $180^\circ / \dots$. As the value θ_s becomes smaller, obviously, the circumferential dynamic magnetic field by the coil will be more uniform but the winding process may be more difficult so it would require more efforts. An appropriate value of θ_s for the given dimension of the OSH-MPT is found by the finite element simulations. For example, the prototype of the OSH-MPT shown Fig. 3.2 is fabricated for $\theta_s = 20^\circ$. In this case, a cylindrical permanent magnet of $d_M = 20$ mm (d_M : the diameter of the magnet) and $h_M = 5$ mm (h_M : the height of the magnet) is used to supply proper static magnetic field. The simulation results will be given in Subsection 3.3.2.

3.3 OSH-MPT for a Nonferromagnetic Plate

Theoretically, for the transduction of elastic waves, MPTs can be applied to any elastic material by attaching the patch to specimen using bonding material. Among applications using MPTs for various elastic media, nonferromagnetic structures such as aluminum structures are mostly preferred. In the case of nonferromagnetic structures, the generated magnetic fields by the installed MPTs on the structures do not cause any magnetic interference between transducers and the structures. Therefore, more reliable wave transduction can be achieved if MPTs are used in

nonferromagnetic structures.

To facilitate the developed OSH-MPT in a nonferromagnetic plate, a 1 mm thick aluminum plate is considered. The performance evaluation of the OSH-MPT installed on the aluminum plate is carried out in several ways. Through experiments and numerical analysis, SH wave transduction using the transducers is investigated with its sensitivity and the radiation pattern of the OSH-MPT is also examined. Furthermore, the frequency characteristic of OSH-MPTs of different sizes and the effect of static magnetic field on the patch are studied. By successfully evaluating the performances of the OSH-MPT in a nonferromagnetic plate, it is shown that the developed transducer can be an attractive tool to inspect large plates using omnidirectional SH waves.

3.3.1 SH wave transduction and transducer sensitivity

In this subsection, the generation of the desired SH wave mode without being accompanied by other unwanted wave modes such as Lamb wave modes is checked through experiments using the OSH-MPT installed on a 1 mm thick aluminum plate. Moreover, the linear sensitivity of the transducer according to linearly increasing input current is experimentally checked considering the practical use.

For actual applications of the developed transducers, the transducers are tightly bonded onto the aluminum plate by bonding material (in this case, epoxy resin is used). While the cylindrical permanent magnet placed over the patch provides the static magnetic field in the radial direction, an alternating current flow into the coil generates the dynamic magnetic field in the circumferential direction and the coupling of two magnetic fields generates shear deformation of the patch by the Wiedemann effect as discussed above. First, the generated guided waves using a pair of OSH-MPTs in the pitch-catch manner is examined if the measured guided wave is only the desired SH wave mode without being accompanied by other unwanted wave modes (Lamb wave modes). This examination is very important in developing SH wave transducers because the generation of other unwanted modes can negatively influence on the inspection results.

Fig. 3.4 sketches the used experimental setup to verify the type of the measured guided waves using a pair of OSH-MPTs installed on a 1 mm thick aluminum plate. The center frequency of actuation is $\eta = 150 \text{ kHz}$ and the targeting wave mode is the fundamental SH wave mode (SH0 mode). Note that SH0 mode is the only nondispersive mode among all guided waves in plate structures. Two OSH-MPTs having the identical configuration ($r_i = 5 \text{ mm}$, $r_o = 15 \text{ mm}$ and $\theta_s = 20^\circ$) are employed both as a transmitter and a receiver, respectively. With these values of r_i and r_o , the difference between inner and outer radii matches half the wavelength

of the SH0 mode at 150 kHz. The input signal into the coil is the Gabor pulse of the following form as used in [87]:

$$f_{Gp}(t) = e^{-\frac{t^2}{2\sigma^2}} \cos(2\pi\eta t), \quad (3.1)$$

where σ , the spread in the time axis, is chosen to be $\sigma = 5.3 \times 10^{-6}$ s when the central frequency (η) is 150 kHz.

The experiment procedure with the setup in Fig. 3.4 is as follows. The input signal generated by a function generator (33250A, Agilent Technologies Inc., Santa Clara, CA) is amplified by a power amplifier (AG1017L, T&C Power Conversion, Rochester, NY) and then sent to the transmitter. The wave generated by the transmitter propagates omnidirectionally in the plate and measured by the receiver located 200 mm away from the transmitter. The measured signal is then amplified by a preamplifier (SR560 low-noise pre-amplifier, Stanford Research Systems, Sunnyvale, CA) before recorded by an oscilloscope (WaveRunner 104MXi-A, LeCroy, Chestnut Ridge, NY).

Fig. 3.5 (a) is the group velocity curves of guided waves for the test aluminum plate of 1 mm in thickness. As it is seen in Fig. 3.5 (a), three wave modes (S0, A0 and SH0 modes) can be measured at 150 kHz in the experimental setup.

Accordingly, the measured wave using the OSH-MPTs should not contain the fundamental Lamb wave modes (S0 and A0) except SH0 mode. Fig. 3.5 (b) shows the measured wave signal using the OSH-MPTs. By checking the arrival time of each wave packet in Fig. 3.5 (b), it is confirmed that no wave mode other than the desired SH0 wave mode is measured; the measured wave packet around at $t = 70 \mu\text{s}$ (t : time) represents the SH0 wave mode directly propagated from the transmitter to the receiver and the packet around at $t = 260 \mu\text{s}$, the reflected SH0 wave mode from the closest boundary of the plate. If the fundamental Lamb wave modes (denoted by the S0 and A0 mode in Fig. 3.5 (a)) are generated by the OSH-MPT, it would appear some wave packets of appreciable magnitudes at the areas in the time axis as marked by dotted circles in Fig. 3.5 (b).

The variation of magnitudes of the measured output signals using the transducers is investigated with respect to varying input current. By doing so, the sensitivity of the transducer is characterized which is the important feature of ultrasonic transducers. As shown in Fig. 3.6 (a), the peak-to-peak value of the first arrival signal ($V_{\text{ptp}}^{\text{SH0}}$) is experimentally examined for various input currents varying from 0.9 A to 5.4 A. Fig. 3.6 (b) shows the experimental results for the sensitivity of the developed OSH-MPT. It is found that the magnitude of measured signal linearly increase as the input current to the actuating coil also increase. Because the operation point is biased at the linear area in the magnetostriction curve of the

nickel patch, the linear sensitivity of the transducer is obtained as long as the input current is applied less than 5.4 A. In other words, the sensitivity is no longer linear due to the saturated magnetization of the patch when the input current is more than 5.4 A. Fig. 3.6 (b) provides the linear operating range that will be helpful for the use of the OSH-MPT in practical applications.

3.3.2 Omnidirectivity of the SH wave by OSH-MPT

This subsection presents the study on the omnidirectivity of the developed OSH-MPT using finite element simulations and experiments. Although finite element simulations can be used for the investigation of various characteristics of the OSH-MPT, they are mainly used to check its generation of dominant SH waves and the omnidirectivity. The finite element simulation is performed using the three dimensional full time transient model constructed and analyzed by the commercial package, COMSOL Multiphysics 3.5 [88]. The various elements used in the finite element model are illustrated in Fig. 3.7 (a). For instance, the copper coil used in the experiment is modeled by the segmented wires. The magnetostrictive constitutive relation based on a linearized isotropic equation [69] is considered for the magnetostrictive patch, which is commonly called the piezomagnetic theory. It can be symbolically written as:

$$S = s^H T + d_t H , \quad (3.2)$$

$$B = dT + \mu^T H, \quad (3.3)$$

where S , T , H and B are the strain, the stress, the magnetic field strength and the magnetic flux density, respectively. In Eqs. (3.2) and (3.3), the symbol s^H denotes the elastic compliance measured at constant H , the symbol d , the piezomagnetic strain coefficient, the symbol μ^T , the permeability, and the symbol d_t , the transpose of d . After the static magnetic field analysis is performed in the magnetostrictive patch, the value of the bias magnetic field is used to determine the piezomagnetic coefficient. Using the result of the static magnetic field analysis as an initial configuration, the analysis for the dynamic magnetic field is then carried out. The remaining modeling procedure and transient finite element analysis are rather standard, the details are skipped. The geometric data ($r_i = 5$ mm, $r_o = 15$ mm and $\theta_s = 20^\circ$, etc.) and the excitation frequency are the same as those used in Subsection 3.3.1.

Fig. 3.7 (b) shows the snapshot of the shear strain component ($\epsilon_{r\theta}$) on the aluminum plate at $t = 35$ μ s. Among others, the shear strain distribution is virtually axisymmetric, implying the omnidirectional property of the generated SH waves by the OSH-MPT. Furthermore, the propagation speed of the generated axisymmetric shear strain (omnidirectional SH waves) also agreed well with the theoretical group velocity of the SH0 wave mode. Although not shown here, other

strain components, such as ε_{rr} and $\varepsilon_{\theta\theta}$, are also analyzed. It is examined that the magnitudes of these strain components are shown to be negligibly smaller compared with that of $\varepsilon_{r\theta}$. The analysis of other values of θ_s is also carried out, but it appears that the radiation pattern of the generated SH waves by the OSH-MPT with $\theta_s = 20^\circ$ yielded sufficiently omnidirectional for the patch geometry considered here.

The omnidirectivity of the developed OSH-MPT is also checked experimentally. All data used in previous sections are also used here. Two sets of experiments are performed to check the omnidirectivities of the transducer as a transmitter and also as a receiver, respectively, although the two results should be the same theoretically in consideration of the reciprocity. The experimental setups and the radiation patterns of the two cases are shown in Figs. 3.8 and 3.9. The distance between the transmitter and the receiver is 300 mm, and measurements are made at every 15° from 0° to 180° for both cases. By extracting the peak-to-peak voltage values from all measured signals with the proper normalization, the radiation patterns of the developed OSH-MPT are measured.

The radiation pattern for the first case, the omnidirectional SH wave generation by the OSH-MPT is shown in Fig. 3.8. Note that while the OSH-MPT is used as a transmitter, a single line SH wave MPT is intentionally used as a receiver as

illustrated in Fig 3.8. Because the single-line MPT has a flat response characteristic for the desired frequency band according to the patch size, it can measure waves without distortions of waveforms caused by frequency dependencies. Otherwise, the frequency characteristics of the receiving unit should be compensated by adjusting the configuration of transducers, which makes the analysis of the measured signals difficult and inaccurate. As shown the bottom figure of Fig. 3.8, the radiation pattern is virtually omnidirectional. It represents the generated SH waves by the OSH-MPT is propagated in all direction uniformly. Hence, the omnidirectivity of the OSH-MPT as a transmitter is experimentally confirmed.

Likewise, for the second case, the single-line MPT is used as a transmitter to generate SH waves while the OSH-MPT is used as a receiver for SH wave measurement (see Fig. 3.9). The experiment results are plotted in the bottom of Fig. 3.9. It is observed that the radiation pattern in the second case is also omnidirectional. Therefore, the developed OSH-MPT also can measure SH waves omnidirectionally if it is used as a receiver. From Figs. 3.8 and 3.9, it is found that the OSH-MPT exhibits satisfactory omnidirectivity properties as a transmitter and a receiver, respectively. Some deviations from the perfect omnidirectivity appear to due to some irregularities in coil winding and patch bonding, and the unique properties of the magnetostrictive material such as anisotropy, nonlinear hysteresis. Especially, as it can be implied in Fig. 3.10, the bonding condition and the wound coil of the used transducers (the OSH-MPT, the single-line MPT) dominantly cause

the deviations. Fig. 3.10 (a) shows the installation process of the OSH-MPT on a plate using the bonding material. Because the wound coil and bonding material in the bottom side of the transducer are directly placed on a plate, the uniformity of the transducer bonding can slightly be distorted. Besides, the thirteen single-line MPTs are bonded onto the designated locations and it causes some irregularities. The photo of the single-line MPT is shown in Fig. 3.10 (b). To sum up, in spite of these trivial errors from fabrications and experiments, the radiation patterns by the OSH-MPT are shown to be omnidirectional.

3.3.3 Frequency characteristic

Here, the frequency characteristics of the developed OSH-MPT are investigated with further experiments. The experiments are performed using the transducers having the magnetostrictive patches of different sizes. As mentioned in Subsection 3.2.1, the patch of the developed MPT is so designed as to be tuned at the SH0 wave by making $r_o - r_i$ equal to half its wavelength. The patch geometry with the relation is depicted in Fig. 3.11 (a). The tuned patch size indicates that the maximum wave signal will be obtained due to the constructive interference when half the wavelength of the SH0 wave mode at the excitation frequency is the same as $r_o - r_i$. To check the frequency characteristics, three different patch sizes are considered in making the OSH-MPTs as listed in Table 3.1. The values of θ_s and

the magnet dimensions are adjusted considering the patch size: $\theta_s = 16.36^\circ$ and $d_M = 30$ mm for Case 1, $\theta_s = 20^\circ$ and $d_M = 20$ mm for Case 2 and $\theta_s = 22.5^\circ$ and $d_M = 15$ mm for Case 3. The height of the magnets is 5 mm for all cases. The photos of the actually fabricated patches and the wound coil on it for the three cases are shown in Fig. 3.11 (b).

For the experiments, the excitation frequencies are varied from 60 kHz to 240 kHz in an increment of 10 kHz while the maximum input current to the coil remained the same. The peak-to-peak voltage values were extracted from the measured SH wave signals and normalized with respect to their maximum value for each case. The three curves characterizing the frequency responses for each case are plotted in Fig. 3. 12. The maximum value for each case is marked by the solid circle and it is observed that the relation $r_o - r_i = \lambda / 2$ is shown to be valid. In other words, when the maximized peak-to-peak values are obtained at the target frequency (corresponding to the wavelength), it confirms the effectiveness of the proposed patch size selection scheme. Obviously, smaller-sized patches should be used to excite SH0 wave modes effectively at higher frequencies. Table 3.1 summarizes the experimental results. The frequency and the corresponding wavelength of the SH0 wave mode are listed in Table 3.1 when the maximum peak-to-peak voltage values are obtained for each case.

3.3.4 Optimal static magnetic field strength in patches

In general, the performance of SH wave MPTs highly depends on the applied static magnetic field strength as shown in Fig. 3. 13. The magnitude of the generated SH wave varies nonlinearly according to the bias field [70, 89-94]. Hence, by controlling the value of the static magnetic field, the patches of MPTs can be biased at the optimal operating point and the performance of MPTs can be maximized. Likewise, in configuring the OSH-MPT, supplying the optimal static magnetic field to the patch is important.

To find out the configuration of the magnet that supplies the optimal static magnetic field to the patch, numerical simulations are performed. The optimal value is considered according the Ref. [70]. The axisymmetric model of the OSH-MPT for case 2 is formed as shown in Fig. 3.14 (a). The diameter of the magnet (d_M) and the vertical position of the magnet from the patch (h) are adjusted to apply the optimal static magnetic field. The symbol D represents the radial width of the patch. Fig. 3.14 (b) is the nonlinear magnetization curve of the nickel patch, which is included in the simulations.

The radial distribution of the static magnetic field in the patch is changed by the value of d_M as shown in Fig. 3.15 (a). If the d_M is equal to $2D$, the distribution is symmetric. Because the symmetric distribution results more uniform

deformation of the patch, it is decided that the d_M is fixed to be the same with $2D$. Now, the value of h is changed as shown in Fig. 3.15 (b). Obviously, the applied static magnetic field strength in the patch decreases as the h increases. At this time, the static magnetic field distribution in the radial direction becomes more flat and its mean value is almost same with the optimal value, which is about 10 kA/m, as found in [70]. Therefore, for applying the optimal static magnetic field to the patch, the value of d_M is chosen to be equal to $2D$ first. Then, the vertical position is controlled to adjust the strength of the applied static magnetic field. Note that Figs. 3.15 (a) and (b) is the results of the OSH-MPT for case 2. Fig. 3.15 (c) shows the results for case 1~3 with the proposed scheme. The different h values are found that make the applied field in the patch to be optimal (H_o) as indicated by the dotted circles and the horizontal arrow in Fig. 3.15 (c). The simulation results are also presented in Table 3.2.

For case 2, the proposed scheme for the optimization of static magnetic field is verified by experiments. In this verification, the same experimental setup introduced in the previous sections is used. By increasing the value of h while the value of d_M is chosen to be 20 mm (i. e. the value of D is 10 mm), the measured signals are compared in Fig. 3.16. In consideration of the prediction by the simulation results in Fig. 3.15 and Table 3.2, the largest signal should be measured if the h value is 8 mm for case 2. It is easily observed that the signal at

$h = 8 \text{ mm}$ is the largest as indicated by dotted lines in Fig. 3.16. Accordingly, the proposed scheme for the optimal static magnetic field in the patch is successfully verified via experiments. Even though not shown here, the experiments for the other cases are also carried out and the predictions are well agreed with experimental results.

3.4 OSH-MPT for a Ferromagnetic Plate

As mentioned above, the use of an array of omnidirectional guided wave transducers is an attractive method to efficiently inspect large plate structures [18, 19]. Transducers are essential components of array systems. So, investigations focusing on the development and application of omnidirectional guided wave transducers for various uses in the fields of nondestructive evaluation (NDE) and structural health monitoring (SHM) are commonplace [33, 35, 82, 95-97]. In these previously reported studies, omnidirectional Lamb wave transducers are mainly used, as it is easier to generate Lamb waves than shear-horizontal (SH) waves. The first omnidirectional SH wave transducer was only recently developed [95, 97] using magnetostrictive patch transducer (MPT) technology [39], which is introduced in the above sections referred as OSH-MPT. The performance of the OSH-MPT is successfully evaluated by wave transduction simulations and experiments in a nonferromagnetic (aluminum) plate. The reason why a SH wave transduction mechanism is preferred for NDE and SHM applications is that SH

waves possess several advantages over Lamb waves [47, 52, 98], such as the nondispersive property of the fundamental mode (SH0 mode) and the ability to resist influence from fluid loading on a plate.

For the practical use, the use of OSH-MPTs for the applications of a ferromagnetic plate (such as a steel plate), a widely used material in various industrial applications, needs to be considered. To generate omnidirectional SH waves in a ferromagnetic plate, using an EMAT technique (see Chapter 4) can be an alternative solution. As discussed in Section 2.4, however, the signal to noise ratio (SNR) of MPTs is greater than that of EMATs. Hence, the efforts to use OSH-MPTs for a ferromagnetic plate are needed. Usually, using MPTs installed on ferromagnetic structures is challenging due to the induced magnetic interference by the magnetic flux leakage into the ferromagnetic plate. More specifically, magnets and coils in MPTs produce static and dynamic magnetic fields and it is applied to not only a patch and ferromagnetic structures. Affected by this, the induced magnetic fields on the structures generate some magnetic field interferences between MPTs and structures, which influence on the poor performance of wave transduction. In the case of OSH-MPTs, the similar problem can occur. Therefore, in this section, the issues and difficulties associated with using an OSH-MPT for ferromagnetic plates are fully investigated [99]. Additionally, the practical solutions to overcome these difficulties by controlling the configuration of the transducer are newly proposed.

3.4.1 Issue on OSH-MPT for a ferromagnetic plate

Fig. 3.17 (a) shows a schematic configuration of an OSH-MPT bonded to a ferromagnetic plate. Some geometry parameters considered in the subsequent subsections are also indicated. Note that MPTs operate on the basis of magnetostriction effect [36, 38], a coupling effect between the change in a magnetic field and a mechanical deformation of a magnetostrictive material (patch). The OSH-MPT consists of a thin annular magnetostrictive patch and a magnetic circuit made of a cylindrical permanent magnet and a specially wound coil. The magnetic circuit provides a magnetic field to the patch that is bonded onto a test ferromagnetic plate. The patch functions as an actuating and a sensing unit for wave transduction. If the static magnetic field generated by the magnet and the dynamic magnetic field generated by the coil are orthogonally applied to the patch, a time varying shear deformation is generated in the patch as a result of the Wiedemann effect [73]. This in turn excites the plate and generates the propagating SH waves. It should be noted that the OSH-MPT can also be used to measure SH waves in a plate structure by the reversed Wiedemann.

Now, a case when an OSH-MPT is installed on a ferromagnetic plate for wave transduction is considered. In this case, the magnetic field provided by the magnetic circuit is not applied just to the patch but also to a test ferromagnetic plate. As reported in the previous research using MPTs for a ferromagnetic pipe

[100], such magnetic flux leakage can seriously be problematic.

To demonstrate the problems caused by magnetic flux leakage, SH guided wave experiments using the OSH-MPT in a ferromagnetic plate are performed, as shown in Fig. 3.17 (b). Fig. 3.18 shows the experimental results. It compares the measured SH waves using a pair of OSH-MPTs in the pitch-catch manner in a nonferromagnetic aluminum (case 1) and a ferromagnetic AISI 1008 plate (case2). The experiments are carried out at 150 kHz with a similar setup to that shown in Section 3.3 using the same OSH-MPT and the same input current. From the comparison in Fig. 3.18, two important observations are made. First, the amplitude of the measured signal of the fundamental SH wave mode (SH0 mode), which is the desired wave mode in this research, in the ferromagnetic plate (case 2) is much smaller than that of the wave in the nonferromagnetic plate (case 1). More importantly, an unwanted wave mode (identified as the fundamental symmetric Lamb wave mode, the S0 mode considering the wave speed) is measured prior to the SH0 mode in the ferromagnetic plate.

The decreased transduction efficiency for the SH0 wave mode and the generation of the unwanted S0 mode are likely related to magnetic flux leakage. However, the detailed investigation of the reason for these problems should be conducted and a method to overcome such problem should also be suggested. Previous related investigations [90] show that the reduced magnetic field in the magnetostrictive

material is responsible for the amplitude decrease in the desired wave mode. In this case, the reason for the reduced magnetic field in the patch is the magnetic flux leakage into the ferromagnetic plate. Furthermore, because the generation of the unwanted Lamb wave mode is unique to the application of OSH-MPTs for ferromagnetic plates, it needs to be clearly explained. Then, a method to increase the amplitude of the desired SH wave mode without generating the undesired S0 wave mode can be suggested. Numerical simulations and wave experiments are performed to validate the effectiveness of the proposed method developed to make OSH-MPTs applicable to ferromagnetic plates for practical use.

3.4.2 Investigation of magnetic flux leakage problem

In this subsection, the detailed configuration of an OSH-MPT is first presented. Then, the magnetic flux leakage problems discussed above are investigated with the explanations on the related parts of an OSH-MPT that is installed on a ferromagnetic plate. Fig. 3.19 shows the top view drawings of part A indicated in Fig. 3.17 (a). Fig. 3.19 (a) shows the detailed coil winding and the AC current flow along the coil. The coil is used to supply the circumferential dynamic magnetic field to the patch while the cylindrical permanent magnet is placed on the patch to apply the radial static magnetic field as shown in Fig. 3.17 (a). Therefore, the coil is wound radially all over the patch along the circumferential direction, similarly to toroid coils. For more uniform and robust coil winding, a nonconductive thin

hosting plate with notches along the inner and outer circumferences is placed over the patch. The coil is wound in an “a–b–c–d” order (see Fig. 3.19 (a)) in accordance with the AC current flow. More details on the coil winding are the same with the explanations provided in the previous sections [95, 97].

Several types of magnetic fields generated by the magnet and coil are also shown in Fig. 3.19 (b). Among the indicated magnetic fields, the combination of the radial static magnetic field (H_r^S) and the circumferential dynamic magnetic field (H_θ^D) generate the shear deformation in the patch. The amplitude of the shear deformation is highly affected by the static magnetic field strength in the patch. Therefore, the sensitivity of the OSH-MPT operating on a ferromagnetic plate would decrease rapidly because the applied H_r^S in the patch is not strong enough due to the magnetic flux leakage. In other words, to enhance the transduction efficiency of the OSH-MPT operating on a ferromagnetic plate, H_r^S should mainly be applied to the patch by reducing the leakage. Note that the coil is used to generate H_θ^D . However, the circumferentially wound part of the coil produces an additional dynamic field, the radial dynamic magnetic field (H_r^D) as illustrated in Fig. 3.19 (b). The field H_r^D is an unnecessary part to operate the OSH-MPT, but the use of the circumferentially wound part, an extended part between the radially wound coils, is unavoidable to connect the radially wound part of the coil. If the

OSH-MPT is installed on a nonferromagnetic plate, the H_r^D does not cause any magnetic leakage problems (i. e. no magnetic field interaction between the H_r^D and the plate). However, because the area underneath the circumferentially wound coils is also magnetostrictive in a ferromagnetic plate, this local part of the plate is simultaneously excited in the radial direction by H_r^D . This explains the measurement of the undesired Lamb wave using the OSH-MPT in a ferromagnetic plate.

From the investigation so far, it is clearly found that the performance of the OSH-MPT is significantly influenced by the leakage of static and dynamic magnetic flux into a ferromagnetic plate. Hence, OSH-MPTs should be either reconfigured or properly installed to avoid the adverse effects of the magnetic flux leakage. To this end, the effects of two controllable parameters, the distance between the lower part of the coil wound along the patch and the top surface of a ferromagnetic plate (h_p) and the distance between the magnet and the upper part of the coil wound along the hosting plate (h_m), on the magnetic flux leakage into the ferromagnetic plate are investigated. The mentioned two parameters are defined in Fig. 3.17 (a).

A series of numerical simulations are carried out to investigate the static and dynamic magnetic flux leakages to the ferromagnetic plate using the modeled magnet and coil of the OSH-MPT. For the simulation, a two-dimensional

axisymmetric finite element model of the OSH-MPT is constructed using the COMSOL-Multiphysics 3.5 solver [88]. The magnetization properties of the nickel patch in [101] and a ferromagnetic plate (AISI 1008) in [102] are included in the model. The following numerical values are used for all of the simulations and experiments in this work as

- Nickel patch thickness = 0.15 mm
- Hosting plate thickness = 1 mm
- Diameter of copper coils = 0.3 mm

The simulated static magnetic fields for the OSH-MPT that is installed on the nonferromagnetic (aluminum) and the ferromagnetic plate (AISI 1008) with $h_p = 0$ are compared in Fig. 3.20. Considerable magnetic flux leakage into the ferromagnetic plate is observed. Although the same magnet was used, the averaged value of the radial static magnetic field in the nickel patch (\hat{H}_r^{S-NP}) placed on the ferromagnetic plate is much smaller than that in the patch placed on the non-ferromagnetic plate, which corresponded approximately to 30 kA/m in the non-ferromagnetic plate and 5 kA/m in the ferromagnetic plate, respectively. Here, the superscripts S and NP in \hat{H}_r^{S-NP} stand for “static” and “nickel patch,” respectively. For ferromagnetic plate applications, the maximum value of the leaked static magnetic field in the ferromagnetic plate ($H_r^{S-Plate}$) is approximately

4.2 kA/m, which is comparable with \hat{H}_r^{S-NP} . Because sufficient static magnetic field biasing is needed to ensure good and linear operations of OSH-MPTs as reported earlier in [97], placing the OSH-MPT directly on a ferromagnetic plate considerably decreases the transduction efficiency of SH waves due to the magnetic flux leakage into the plate.

If a larger magnet is employed to supply a stronger static magnetic field to the patch for the compensation of the magnetic flux leakage effect, not only do the overall dimensions of the OSH-MPT increase, but magnetic interference between the transducers forming the array can also be a problem. Moreover, the use of a stronger magnet in a ferromagnetic plate results in the installation of the OSH-MPT being more difficult and dangerous because of the strong magnetic attraction between the magnet and the plate. Accordingly, an alternative method that does not require a strong magnet should be considered.

Now, to examine the adverse effect of the radial dynamic magnetic field (H_r^D) leakage by the circumferentially-wound coils on the generation of unwanted wave modes, the dynamic magnetic field simulations for the OSH-MPT installed on a ferromagnetic plate are carried out similar to the static magnetic field analysis. For the dynamic field simulation, only the circumferentially wound coils are considered because the radially wound coils produce H_0^D that is known to

contribute to shear deformation. Accordingly, radially wound coils are not included in the simulations. The dynamic magnetic field simulation result is given in Fig. 3.21 (a). The circumferentially wound coils induce H_r^D in the ferromagnetic plate, which generates an unwanted axisymmetric Lamb mode (S0) wave as shown before (see Fig. 3.18). It is also interesting to examine how the magnitude of the H_r^D in the plate varies as h_p is changed. As a specific measurement point, the position marked by the red dot in Fig. 3.21 (a) is selected and the normalized values of H_r^D at the point are extracted for various h_p values. A Gabor pulse (the specific form of which is expressed in Eq. (3.1) and [87]) is used as an input AC current, with results are shown in Fig. 3.21 (b). The simulation results in Fig. 3.21 (b) show that the leakage of H_r^D into the plate (which is the reason for the unwanted Lamb wave excitation) is drastically suppressed by lifting the patch and coil slightly off the top surface of the ferromagnetic plate. Because the coil was wound around the patch, the coil is lifted off with the patch simultaneously. For instance, as shown in Fig. 3.21 (c), the peak-to-peak value of the measured dynamic field (H_r^D) decreases about 80% by changing the value of h_p from 0 to 1 mm. It is easily expected that the decreased dynamic field (H_r^D) results the highly suppressed S0 mode.

The numerical studies carried out in this subsection suggest that the leakage

problem can be overcome to a great extent if h_p and h_m are optimally selected. Because the optimal values of h_p and h_m differ depending on the value of the patch size, parameter studies for the different transducer (patch) sizes need to be conducted. It should be noted that the patch size for the OSH-MPT used in this subsection is tuned for 150 kHz, and its specifications are presented in the next subsection.

3.4.3 Design of OSH-MPT for a ferromagnetic plate

As discussed in the previous subsection, the OSH-MPT can be designed for a ferromagnetic plate by adjusting the values of h_p and h_m appropriately. In other words, as a practical means to minimize the adverse effect of magnetic flux leakage, two parameters, h_p and h_m can be optimized. Note that even if h_p is not equal to zero, the shear deformation of the magnetostrictive patch must be transmitted to a ferromagnetic plate. Therefore, by varying the thickness of the epoxy resin bonding layer, the value of h_p can be adjusted. Once the optimal values of h_p and h_m are selected, the radial static magnetic field (H_r^S) can be mainly applied to the patch and the leakage of the radial dynamic magnetic field (H_r^D) is highly suppressed. Numerical simulations, as well as basic experiments are performed to determine the specific values of h_p and h_m .

Prior to choosing the optimal combinations of h_p and h_m , the optimal averaged value of the radial static magnetic field in the nickel patch (\hat{H}_r^{S-NP}), denoted by $^*\hat{H}_r^{S-NP}$, needs to be determined first to identify the maximum patch shear deformation. To find this optimal value, which depends on the material properties of the nickel patch, the basic experiments are conducted first using a pair of OSH-MPTs on a nonferromagnetic (aluminum) plate for various h_m values. For this experiment, h_p is fixed to be zero. The reason to perform the experiment using a nonferromagnetic plate without changing h_p is so that no magnetic flux leakage into the plate occurs in this case.

After carrying out the experiment and simulations for an aluminum plate, the static magnetic field simulations for the OSH-MPT installed on a ferromagnetic plate are performed. The results yield the optimal combinations of h_p and h_m for which the magnetic field in the patch of the OSH-MPT is nearly equal to $^*\hat{H}_r^{S-NP}$. This approach is justified because the actuating and sensing element in the OSH-MPTs is the magnetostrictive patch and the magnitude of the generated SH wave in the plate is affected by the static bias magnetic field in the patch. Furthermore, H_r^D in a ferromagnetic plate is reduced dramatically even for small values of h_p (see

Fig. 3.21), so the effect of h_p on the value of H_r^D may not need to be considered separately as long as the optimal values of h_p making the static radial magnetic field in the patch equal to ${}^* \hat{H}_r^{S-NP}$ are not vanishingly small. Therefore, the optimal values of h_p and h_m in terms of the static magnetic fields in the patch are found first with the reasonable value of h_p (i.e. not too small). Note that for all simulations and experiments, three different OSH-MPT sizes are considered as shown in Table 3.3.

Now, numerical simulations and experiments for a nonferromagnetic plate are performed first to determine the optimal static magnetic fields in the nickel patch of the OSH-MPT. The experiments are conducted using a pair of OSH-MPTs installed on a 1 mm thick nonferromagnetic aluminum plate. The h_m values are varied (with h_p fixed at zero because of the absence of any magnetic field leakage) and, the magnitude variations in measured SH waves are investigated. The experimental setup is shown in Fig. 3. 22. For the experiments, the OSH-MPTs are used as a transmitter and receiver and the distance between the transducers is 200 mm. An input signal to the coil is the Gabor pulse expressed as Eq. (3.1):

The measurement process employed for SH wave transduction in the experiments is as follows. The input signal (Gabor pulse) is generated by a function generator

(33250A, Agilent Technologies Inc., Santa Clara, CA) and amplified by a power amplifier (AG1017L, T&C Power Conversion, Rochester, NY). The amplified signal is then sent to the coil of the transmitter. The SH wave generated by the transmitter is measured by a receiver before being amplified by a preamplifier (SR560, Stanford Research Systems, Sunnyvale, CA). The signal is then recorded by an oscilloscope (WaveRunner 104MXi-A, LeCroy, Chestnut Ridge, NY). For all of the pitch catch wave experiments using OSH-MPTs, the data provided in Subsection 3.4.2 (such as nickel patch thickness = 0.15 mm, etc.) are used. However, the inner and outer radii of the patches, denoted by r_i and r_o , respectively, should be carefully selected because the frequency characteristics of the OSH-MPTs are primarily determined by the patch size. As seen in Fig. 3.19, the width of an annular patch (D) is given by $D = r_o - r_i$. Because the magnitude of the generated SH wave at a specific excitation frequency is maximized as a result of the constructive interference, the patch size is selected to match the wavelength (λ) of the target SH wave mode (SH0 in the present case) in a plate as [97]:

$$D = r_o - r_i \approx \frac{\lambda}{2} \quad \text{and} \quad 2r_i \approx \frac{\lambda}{2}. \quad (3.4)$$

Once the target center frequency (f_c) is determined, the corresponding wavelength in the plate is calculated using the dispersion relation of SH wave modes in a plate.

Table 3.3 lists the center frequencies considered for experiments, the corresponding wavelengths and the selected values of D from Eq. (3.4).

Fig. 3.23 shows the experimental results using the three different sizes of OSH-MPTs for a nonferromagnetic plate. It can be seen that the maximum signal is measured at different h_m values for each case. Using these h_m values for the simulation, the value of ${}^* \hat{H}_r^{S-NP}$ can be calculated. The numerical simulation results for the optimal static magnetic field strength in a patch placed on a nonferromagnetic plate are presented in Table 3.3. Values of ${}^* \hat{H}_r^{S-NP}$, approximately equal to 9 kA/m for the three cases are obtained using a finite element model involving OSH-MPTs when the experimentally measured SH wave signal is largest, according to the various h_m values.

To search for the optimal combinations of h_p and h_m that make the static magnetic field in the nickel patches of OSH-MPTs installed on the ferromagnetic plate (AISI1008) equal to the ${}^* \hat{H}_r^{S-NP}$ values in Table 3.3, numerical simulations are carried out. Because the patch is the key element for shear deformation, applying the same static magnetic field strength to the patch listed in Table 3.3 is most important.

Fig. 3.24 shows how the averaged value of the radial static magnetic field in the nickel patches (\hat{H}_r^{S-NP}) varies with the h_m value of the OSH-MPTs for the three different sizes installed on the ferromagnetic plate. For each plot in Fig. 3.24, h_p is fixed at 0, 1 and 2 mm, respectively. The \hat{H}_r^{S-NP} values are calculated using finite element simulations in which the magnetization property of the ferromagnetic plate is included. The optimal values ($^*\hat{H}_r^{S-NP}$), as given by Table 3.3, are denoted by purple horizontal lines in Fig. 3.24. For instance, in Fig. 3.24 (a), if the patch is not lifted off ($h_p = 0$), all \hat{H}_r^{S-NP} values in the ferromagnetic plate are below the optimal value ($^*\hat{H}_r^{S-NP}$) line. This occurs because of the significant leakage of the static magnetic field into the plate. However, if the patch is slightly lifted off ($h_p = 1.0$ or 2.0 mm), as shown in Figs. 3.24 (b) and (c), the optimal values ($^*\hat{H}_r^{S-NP}$) can be achieved in the patch by adjusting h_m appropriately. In Figs. 3.24 (b) and (c), the optimal combinations of h_p and h_m are indicated by solid dots. From the numerical simulations, the transduction efficiency of SH waves in the ferromagnetic plate are predicted to be maximized if the OSH-MPTs are configured according to the optimal combinations of h_p and h_m . The combinations are found to be optimal, which yield the largest SH wave without the generation of other modes, as follows:

for $D = 7.5$ mm: $(h_p, h_m) \approx (1.0$ mm, 3.0 mm) or (2.0 mm, 4.3 mm),

for $D = 10$ mm: $(h_p, h_m) \approx (1.0$ mm, 2.0 mm) or (2.0 mm, 4.0 mm),

for $D = 15$ mm: $(h_p, h_m) \approx (2.0$ mm, 2.0 mm).

These results will be verified by further experiments in a ferromagnetic plate in the next subsection.

3.4.4 Experimental verification and discussion

For validating the predictions from the simulation results in Subsection 3.4.3, experiments to examine the magnitude variations in the SH waves for different values of h_p and h_m in a ferromagnetic plate are conducted. Moreover, the removal of the unwanted S0 mode is simultaneously confirmed when the patch and coil are lifted off from the plate (in this case, h_p is not zero). To adjust h_p , the thickness of the inserted nonferromagnetic gap (bonding layer) between the patch and the plate needs to be varied. Thus, the OSH-MPTs can be tightly bonded onto the plate by covering the gap with a specially made housing (as shown in Fig. 3.22) to accurately control the thickness of the gap. Epoxy resin is used to form the gap as bonding material. And even if h_p is zero, the minimum amount of epoxy resin is inserted to efficiently transmit the waves from the patch to the plate.

The upper figures in Figs. 3.25, 3.26 and 3.27 show the experimental results for the SH wave transduction in a ferromagnetic plate with varying h_p and h_m values. The normalized peak-to-peak values for the different OSH-MPTs are plotted and the predicted optimal combinations of h_p and h_m values from the simulations in Subsection 3.4.3 are indicated with dotted circles. For the same h_p value, the measured amplitude of the SH waves at the optimal h_p and h_m values (shown with dotted circles) is largest, as predicted by the numerical simulations. However, there is an absolute difference between the amplitudes for the same optimal conditions (the same static magnetic field strength in the patch). For instance, in Fig. 3.26 for the $D = 10$ mm case, the normalized amplitude for $h_p = 1.0$ mm and $h_m = 2.0$ mm is larger than that for $h_p = 2.0$ mm and $h_m = 4.0$ mm. This is considered a reasonable result because the gap thickness also affects the transduction efficiency [93]. A thicker gap (bonding layer) causes more attenuation of the generated waves. Thus, choosing the minimum h_p value under the same static magnetic field conditions is important because of the attenuation that occurs as a result of the gap thickness. Additionally, if $h_p = 0$, the measured signals are significantly smaller than those corresponding to other values for $h_p = 1.0$ mm and 2.0 mm because of the maximized magnetic flux leakage (as examined in Fig. 3.24 (a)). Consequently, to achieve better transduction efficiency

in the ferromagnetic plate, h_p should not be zero.

The lower figures in Figs. 3.25, 3.26 and 3.27 show the measured time signals for a fixed h_m value, as represented by the dashed vertical line (including the optimal condition) in the upper figures. The largest peak-to-peak value of the SH0 modes at the optimal combination is defined as A_{\max} when comparing the transduction efficiency with those from other cases. The amplitudes of the SH modes change according to the h_p value. More importantly, the unwanted S0 mode is measured if h_p is zero due to the radial dynamic magnetic field (H_r^D) leakage, whereas suppression of S0 mode is achieved for $h_p = 1.0$ or 2.0 mm .

The interpretation of the experimental results validates the proposed method for controlling h_p and h_m values. Because not only the static magnetic flux leakage is reduced but the optimized static magnetic field is also applied on the patch by optimally selected combinations of h_p and h_m in the OSH-MPTs operating on the ferromagnetic plate, the transduction efficiency is improved and the unwanted mode excitation is avoided.

The proposed design scheme is validated by simulations and experiments only for the selected h_p and h_m values. To provide useful data for various D values,

numerical simulations are additionally performed as shown in Fig. 3.28. Fig. 3.28 shows the optimal combination of h_p and h_m values that satisfies $^*\hat{H}_r^{S-NP}$ value for the given D values. The corresponding center frequency range can be calculated by the simple dispersion relation of SH waves, $f = \frac{c_{SH0}}{2D}$, where c_{SH0} denotes the wave speed of SH0 wave mode. The frequency range according to the D values in Fig. 3.28 is approximately chosen from 100 kHz to 600 kHz. This is generally concerned range for MPTs based plate applications. Note that there can be several optimal options for the given D value. In that case, choosing the minimum h_p value is important as long as S0 mode is highly suppressed. In other words, the patch should be lifted off from the plate enough to avoid the dynamic field leakage while the attenuation by the bonding layer thickness is minimized. To check the suppression of S0 mode together, numerical wave simulations or experiments should also be conducted as explained in the previous sections.

3.5 Concluding Remarks

In this chapter, an omnidirectional shear-horizontal wave magnetostrictive patch transducer (OSH-MPT) for a plate is newly developed. The specific configuration of the magnetostrictive patch transducer suitable to generate omnidirectional shear-horizontal waves in a plate is proposed. The coil is wound around the thin annular magnetostrictive patch to provide a circumferential dynamic magnetic field in the

patch and the permanent magnet is placed over the center of the patch to provide a radial static magnetic field in the patch. The use of an annular patch shape allows the coil winding over the patch. The specific coil winding strategy is also suggested to provide as uniform circumferential magnetic field as possible in the patch. The omnidirectional SH wave generation by the OSH-MPT is confirmed both numerically and experimentally and no other unwanted wave mode such as the Lamb wave modes is shown to be accompanied by the SH wave. When the difference between the inner and outer radii of the patch is tuned to be half the wavelength of the SH₀ mode at an excitation frequency, the generated SH₀ wave is shown to have the largest magnitude. Using the good omnidirectional property of the developed OSH-MPT, it will be possible to develop a phased array inspection system to cover a wide area of a plate.

The evaluation of the developed transducer is successfully confirmed first for a nonferromagnetic aluminum plate, its application to ferromagnetic plates is also performed. Because ferromagnetic plates such as plates made by various kinds of steel material are widely used and MPTs are not directly applied to ferromagnetic plates for practical use due to the poor performance by magnetic flux leakages, it is worth performing the investigations of OSH-MPTs operating ferromagnetic plate and designing its configuration having the best performance. The reasons for the poor performance of OSH-MPTs installed on a ferromagnetic plate are investigated first and a method to enhance the transducer performance by controlling its

configuration is then proposed. If the OSH-MPT is installed on a ferromagnetic plate, the magnetic fields generated by the magnet and coil substantially leak into the plate. Furthermore, the leakage causes low transduction efficiency of the desired SH wave and an unwanted Lamb wave excitation, which negatively influence the inspection results. To resolve these problems, the configuration of the OSH-MPTs is modified to reduce the magnetic flux leakage and the optimal static magnetic field strength is applied to the patch by adjusting the vertical positions of the patch and magnet. The specific positions of the patch and magnet are optimally selected through numerical simulations and experiments. By doing so, not only is transduction efficiency of the OSH-MPTs considerably enhanced, but the unwanted Lamb wave is also greatly suppressed. The effectiveness of the proposed method is successfully validated through experiments conducted using OSH-MPTs of three different sizes. The experiments are conducted at central frequencies of 100, 150, and 200 kHz. According to these results, the transducer performance is optimized by simply changing the patch and magnet positions by only a few millimeters in the vertical direction. Because the problems encountered when OSH-MPTs are installed on a ferromagnetic plate can be prevented and resolved by employing the proposed method, the details and data in this research will be quite useful when carrying out inspections on ferromagnetic plates using OSH-MPTs.

To sum up, because the previously reported omnidirectional transducers only employ Lamb waves so far, the newly developed OSH-MPT is unique and

meaningful. In addition, the OSH-MPT can be an alternative solution for more effective inspection of plate structures. Through the studies in this chapter, the performance of the transducer is successfully confirmed for a nonferromagnetic and a ferromagnetic plate, respectively, so that various plate applications using OSH-MPTs in practical situation can possibly be made in the future.

Table 3.1 The numerical values of the geometries of considered magnetostrictive patches and the corresponding peak frequency/wavelength of the SH0 wave mode yielding the maximum wave magnitude.

Case	r_o (mm)	r_i (mm)	$r_o - r_i$ (mm)	f_c (kHz) and $\lambda / 2$ (mm)
1	22.5	7.5	15	(100, 15.12)
2	15	5	10	(150, 10.09)
3	11.25	3.75	7.5	(200, 7.56)

Table 3.2 The optimal static magnetic fields applied to the patches for the OSH-MPTs of three different sizes and the corresponding vertical positions of the used cylindrical magnets.

Case	H_o (kA/m)	D (mm)	h (mm)	d_M (mm)
1	10.69	15	9	30
2	10.17	10	8	20
3	9.77	7.5	7	10

Table 3.3 The width of the nickel patch (D) and the corresponding central frequency (f_c)/wavelength(λ) of the SH0 wave mode. The symbol $^*\hat{H}_r^{S-NP}$ denotes the optimal value of the averaged values of the radial static magnetic field in the nickel patch (\hat{H}_r^{S-NP}), when the SH0 signal measured by the pair of OSH-MPTs installed on the 1 mm thick aluminum plate is largest.

f_c (kHz)	$\lambda / 2$ (mm)	D (mm)	$^*\hat{H}_r^{S-NP}$ (kA/m)
100	15.12	15	9.12
150	10.09	10	8.91
200	7.56	7.5	8.75

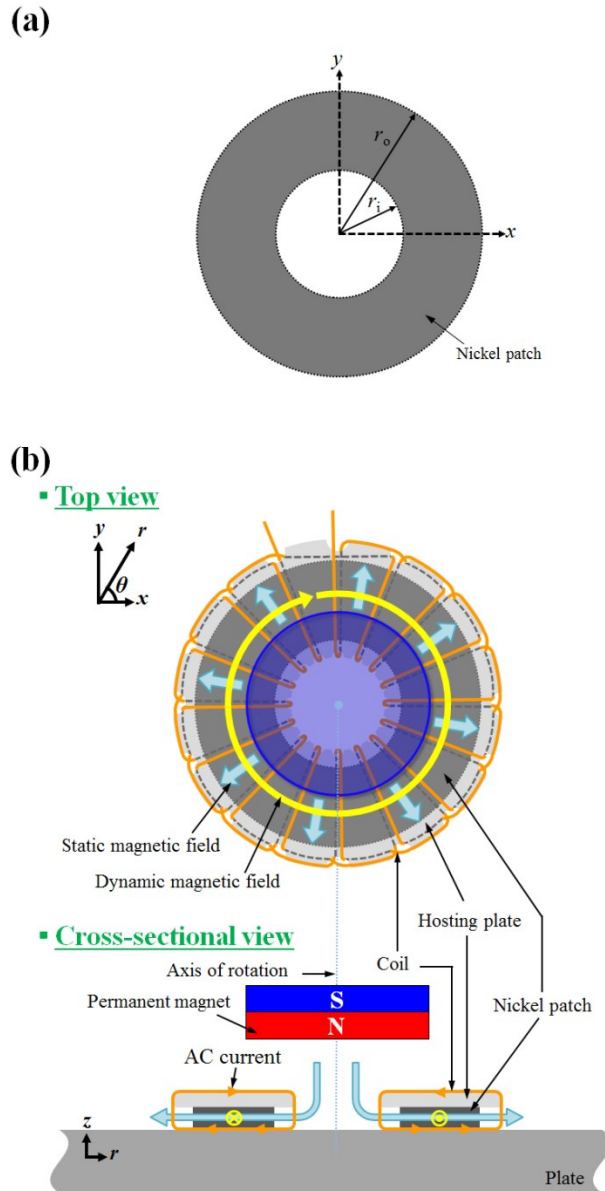


Fig. 3.1 Schematic configuration of (a) thin annular nickel patch used in (b) the developed OSH-MPT on a plate (nonferromagnetic) with the indicated static and dynamic magnetic fields.

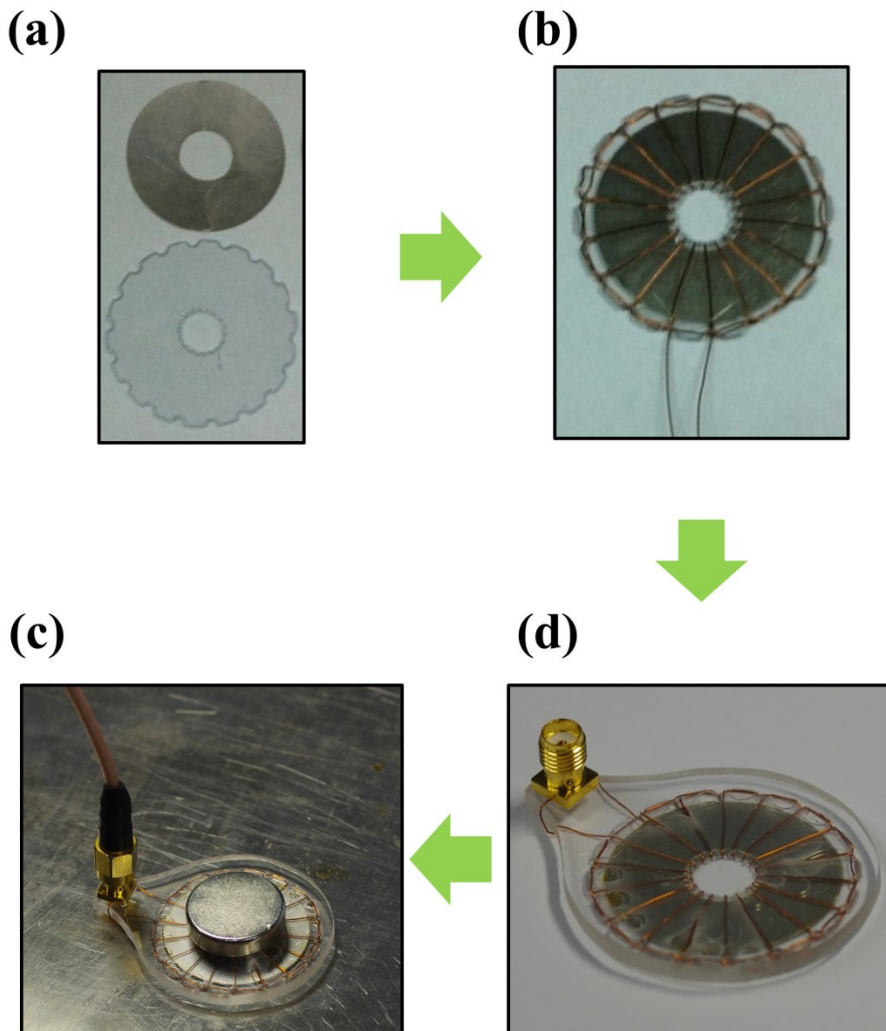
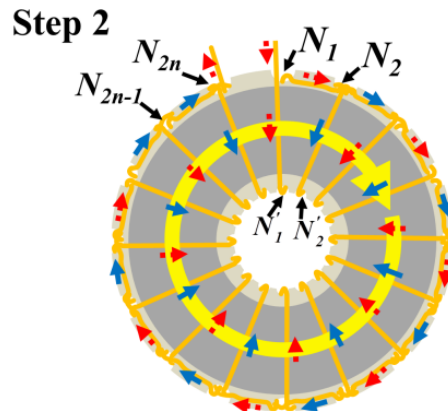
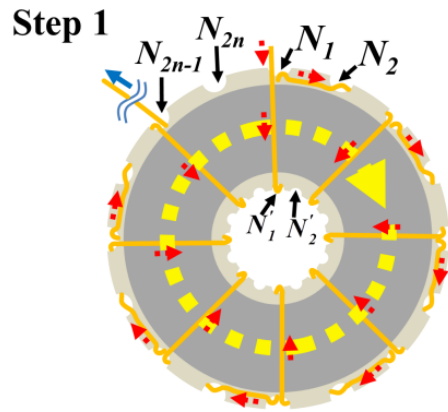


Fig. 3.2 Fabrication process of the OSH-MPT. (a) A thin annular nickel patch and a hosting plastic guide with notches along the circumference. (b) Toroidally wound coil on the set consisting of the patch and the guide. The OSH-MPT connected to an electrical terminal with (c) and without a magnet (d).



···→, → : The direction of current flow
 ···→, → : The direction of dynamic magnetic field

Fig. 3.3 Drawing of the coil winding on the patch and the hosting guide. Step 1 is coil winding for odd numbered notches while Step 2 is for even numbered notches after finishing Step 1. The directions of the current and magnetic field by the coil are indicated by the arrows.

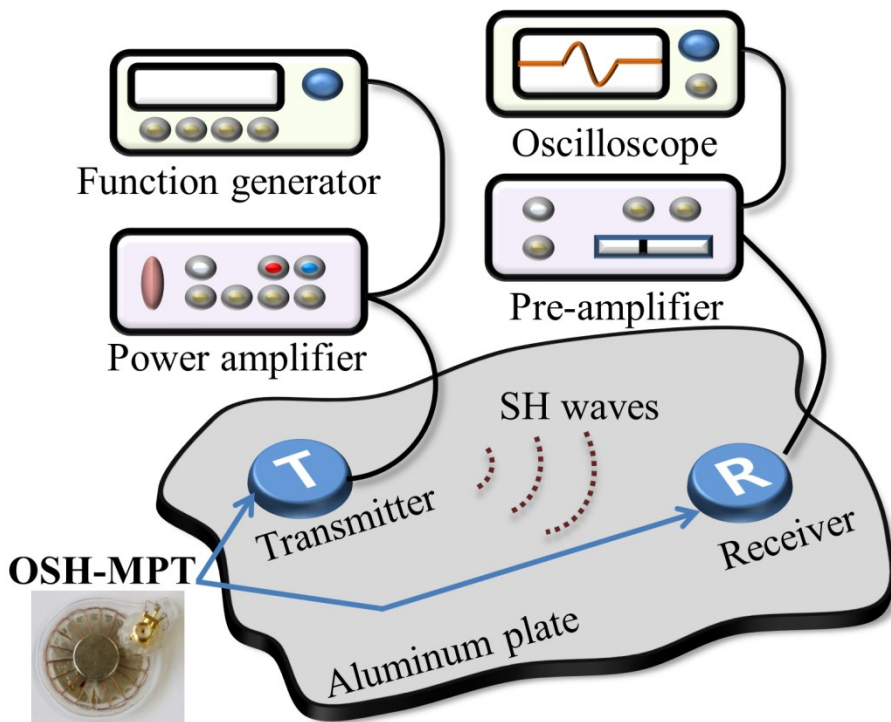


Fig. 3.4 Pitch-catch type experimental setup for SH wave transduction in an aluminum plate using a pair of OSH-MPTs.

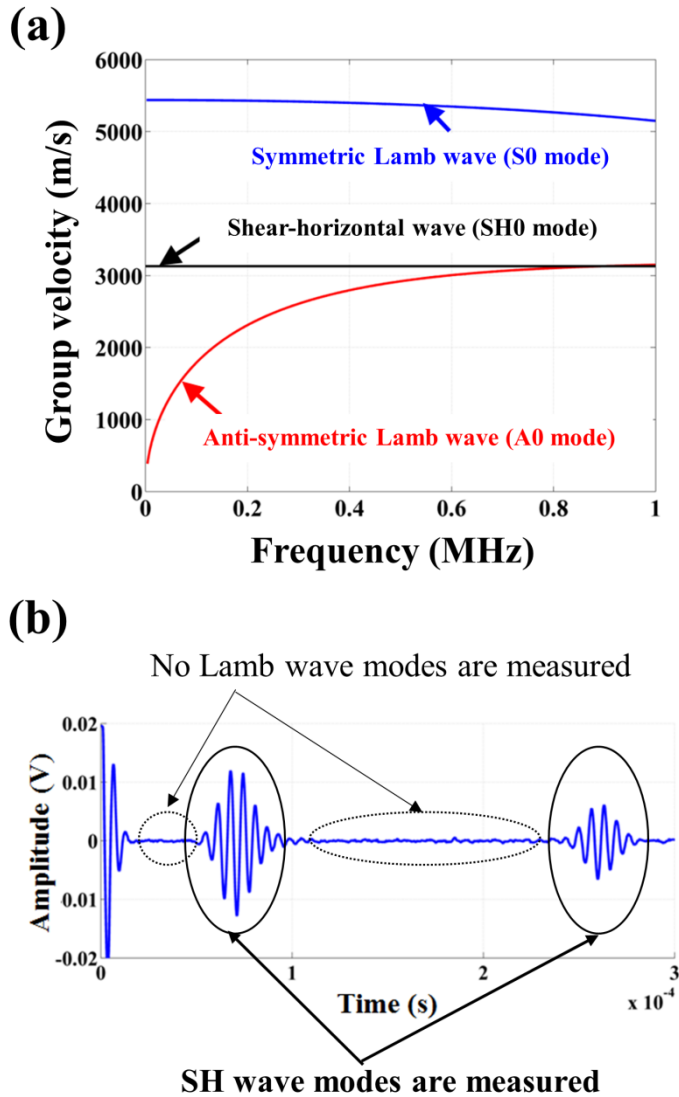


Fig. 3.5 (a) Dispersion curves in terms of group velocity and frequency for Lamb and SH wave modes in a 1 mm thick aluminum plate. (b) Measured wave signal of the generated SH waves using the OSH-MPTs.

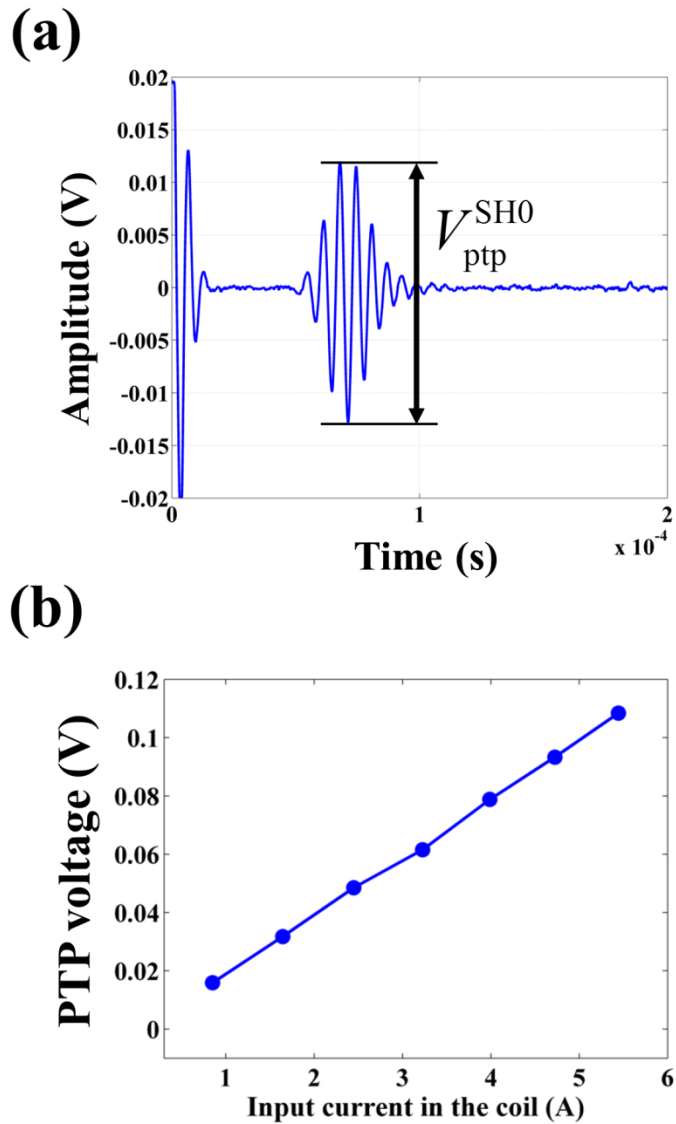


Fig. 3.6 (a) Measured waveform of the first arrival of SH0 mode by the OSH-MPTs. (b) Sensitivity characteristic of the OSH-MPT checked by varying input current in the transmitter coil.

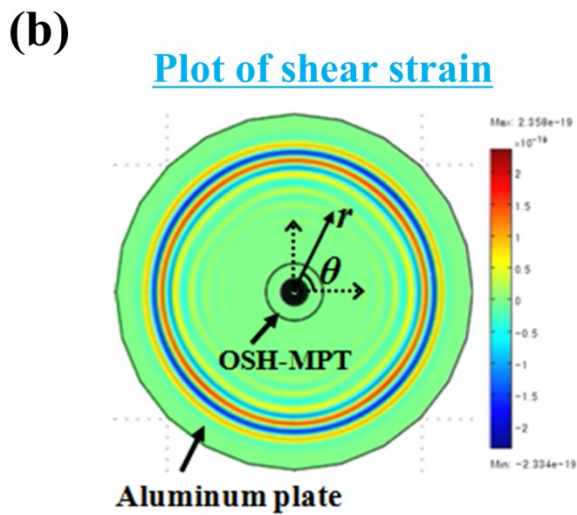
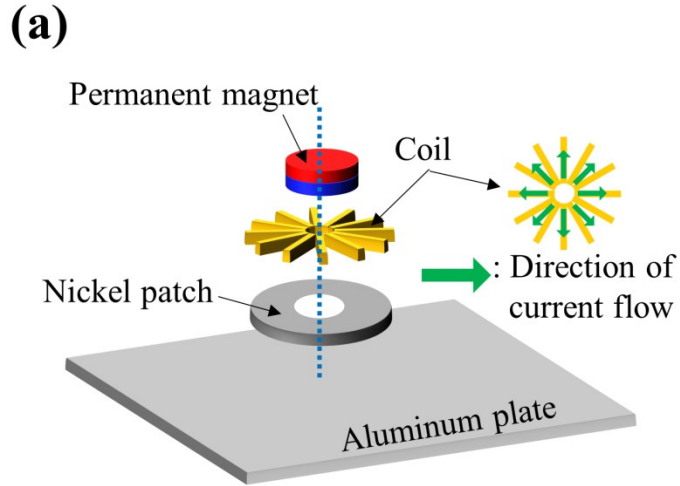


Fig. 3.7 (a) Illustration of schematic model of OSH-MPT for finite element analysis in an aluminum plate. (b) Snapshot of omnidirectionally propagating shear strain $\varepsilon_{r\theta}$ (SH wave) by numerical simulation conducted in an aluminum plate.

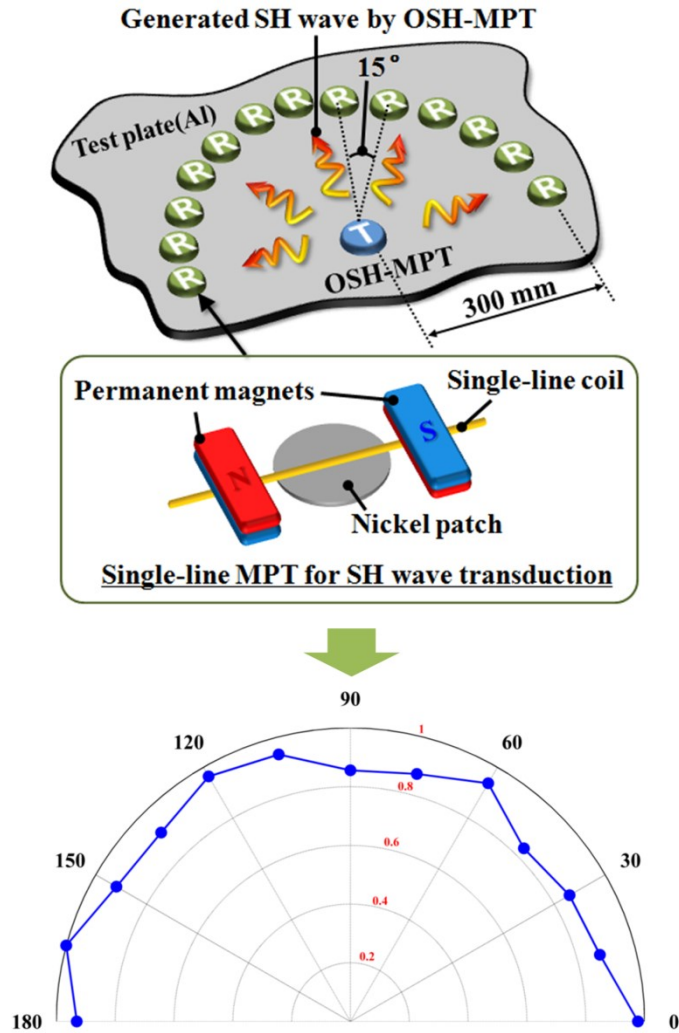


Fig. 3.8 Experimental setup to check the omnidirectional generation of SH wave by the transmitting OSH-MPT and experimentally measured radiation pattern.

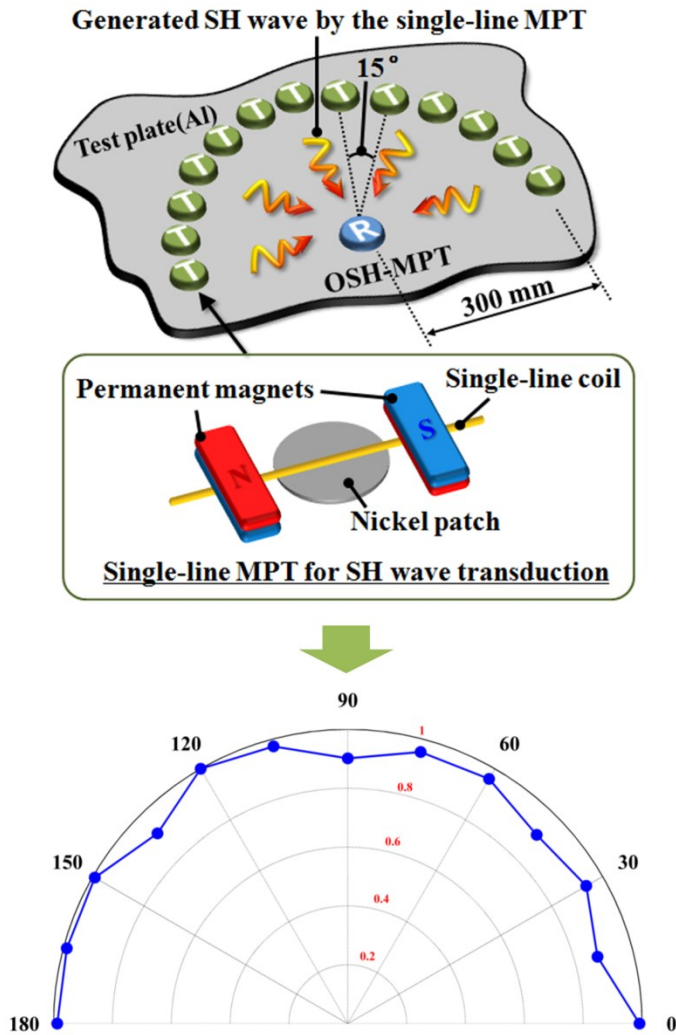


Fig. 3.9 Experimental setup to check the omnidirectional measurement of SH waves using the receiving OSH-MPT and experimentally measured radiation pattern.

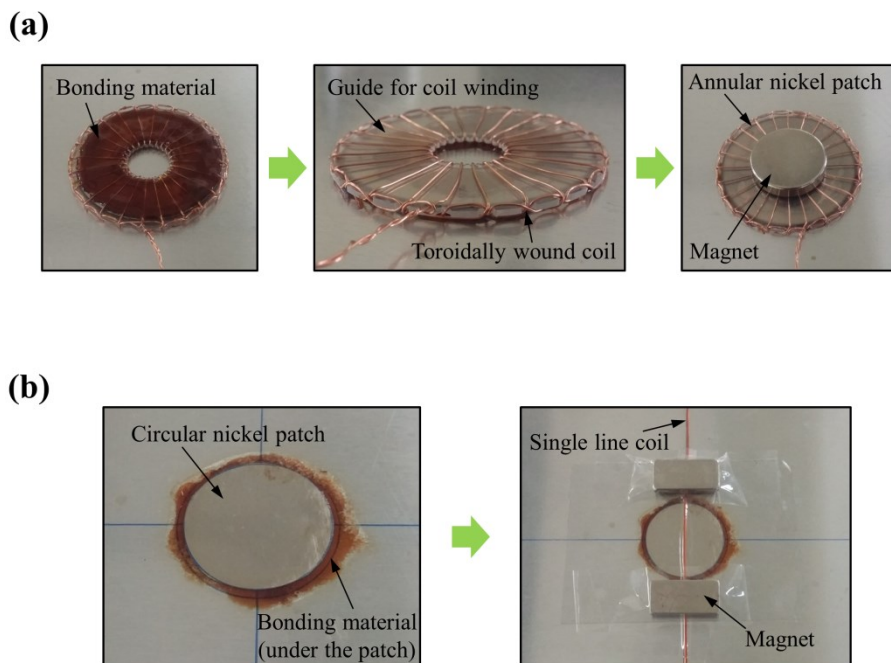
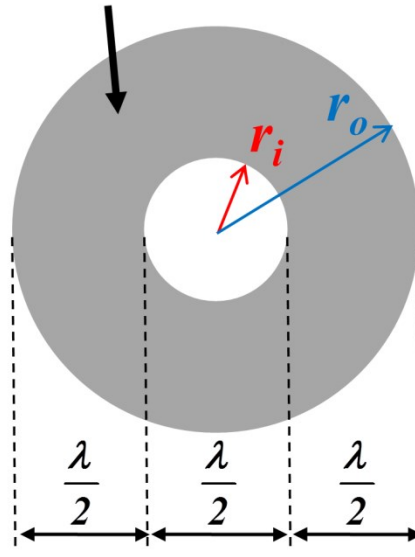


Fig. 3.10 (a) The installation process of the OSH-MPT used for the radiation pattern experiments. The bonding material and the wound coil are directly placed on the plate. (b) The used single-line MPT for the radiation pattern experiments.

(a)

Nickel patch



(b)

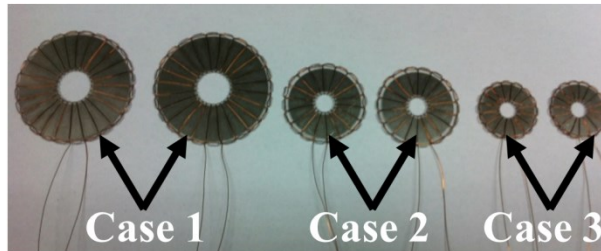


Fig. 3.11 (a) Illustration of an annular nickel patch. The inner diameter ($2r_i$) and the difference between the outer and inner radius ($r_o - r_i$) of the patch are equal to half the wavelength (0.5λ) of target frequencies for SH wave modes. (b) Fabricated OSH-MPTs of three different patch sizes (target wavelengths)

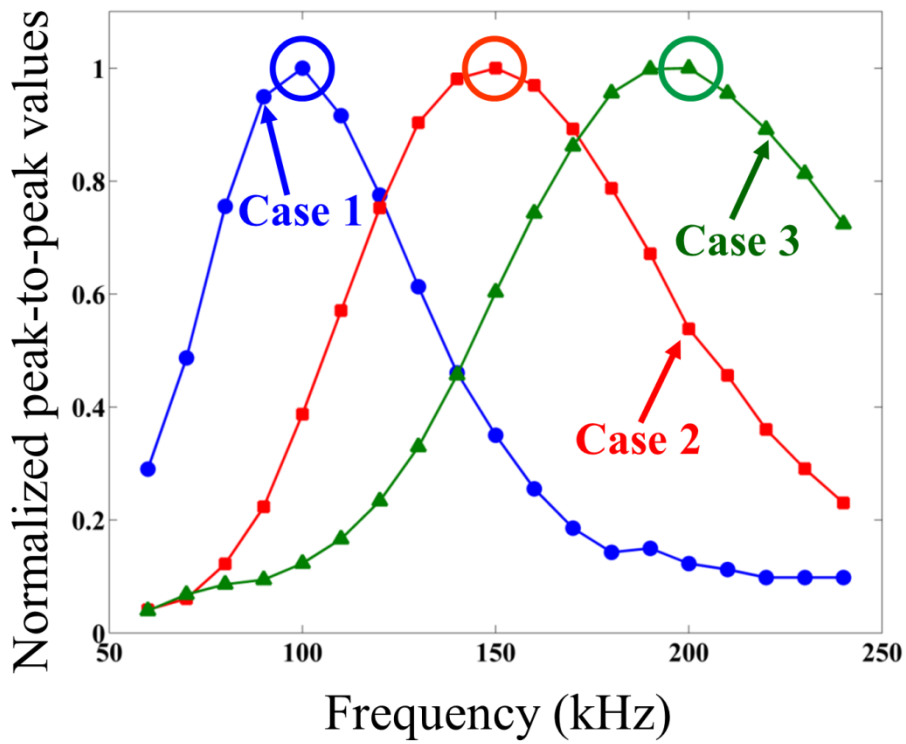


Fig. 3.12 Experimental results of the frequency characteristics of the three different sizes of OSH-MPTs. The peak frequency for each case is indicated by solid line circles.

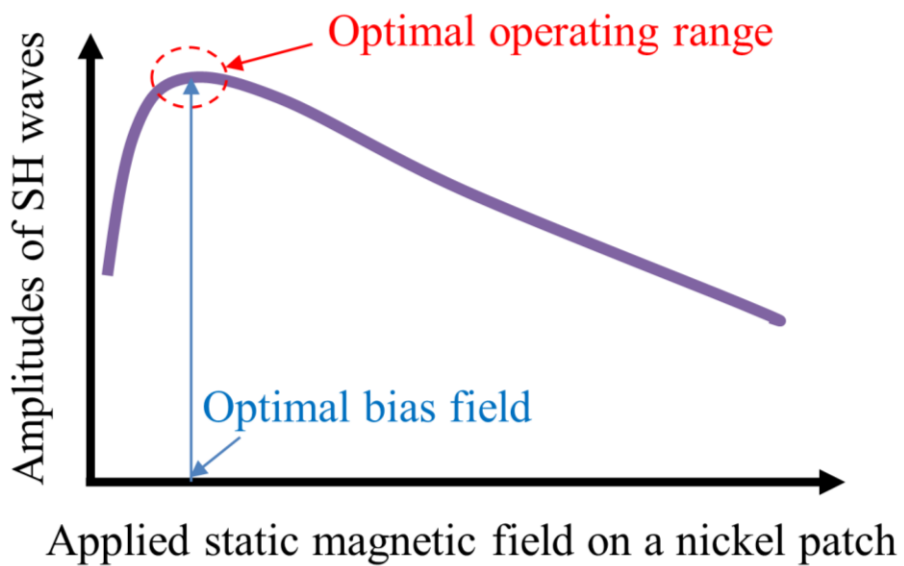


Fig. 3.13 Schematic diagram of the nonlinear amplitude variation of SH wave MPTs according to varying static magnetic fields applied to patches.

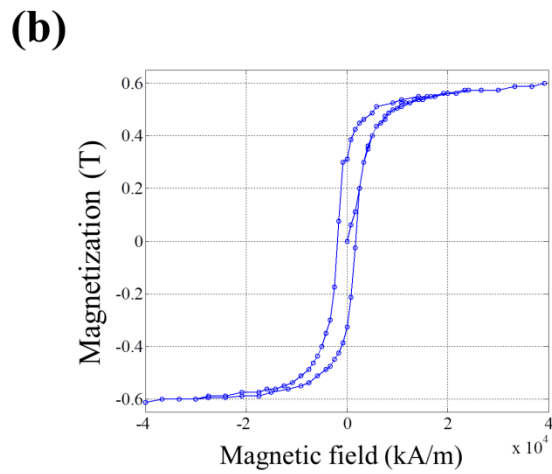
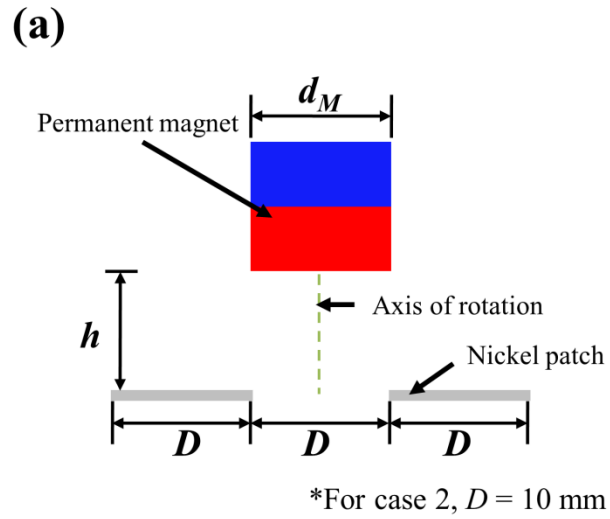


Fig. 3.14 (a) Two dimensional axisymmetric configuration of the OSH-MPT for the static magnetic field analysis including (b) magnetization curve of pure nickel in [101].

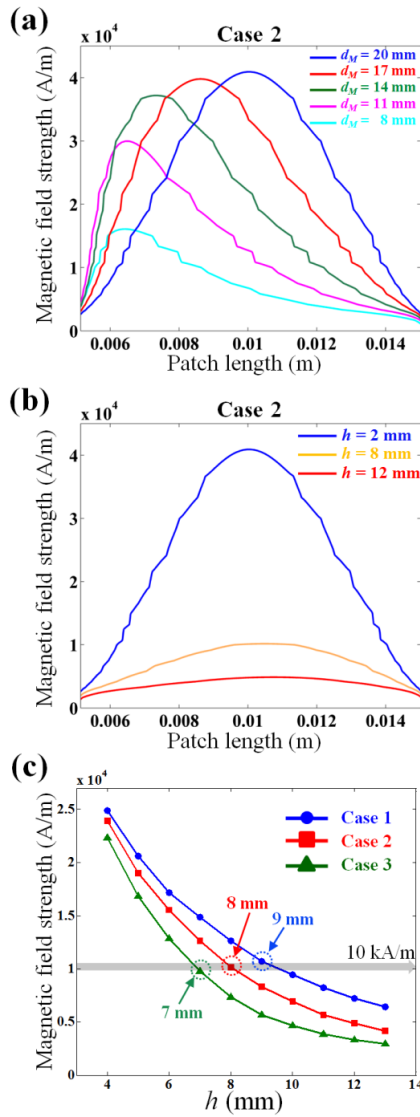


Fig. 3.15 Static magnetic field distribution in the patch along the radial direction by varying (a) the diameter (d_M) and (b) the vertical position (h) of the magnet for Case 2 model. (c) Simulations results of static magnetic fields in the patches for Case 1~3 to find the optimal value (H_o), which is indicated by dotted circles.

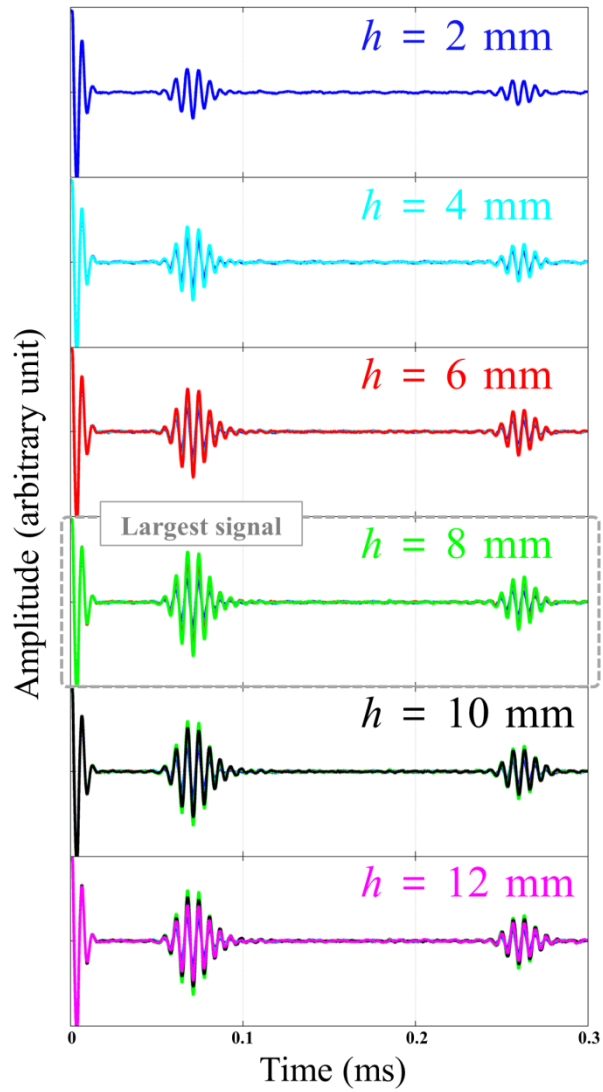


Fig. 3.16 Measured SH wave signals using the OSH-MPT for case 2 according to various h values. The largest first arrival signal of SH0 mode is measured at $h = 8$ mm .

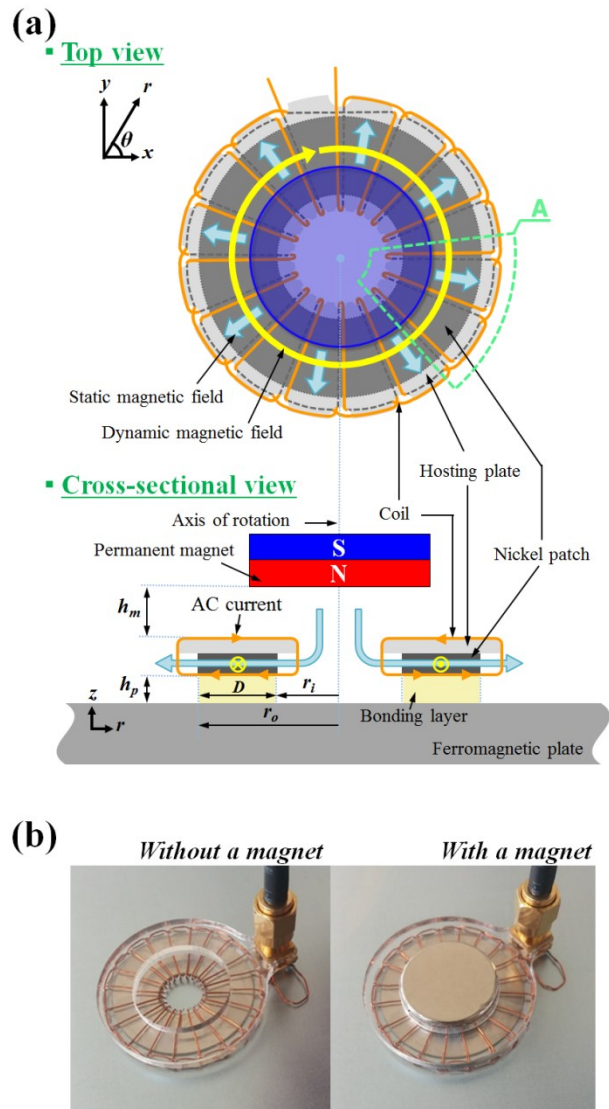


Fig. 3.17 (a) Schematic illustration of the OSH-MPT bonded onto a ferromagnetic plate with the bonding layer of (h_p) in thickness. The parameters related to geometries are defined and the generated static and dynamic magnetic fields are indicated. (b) Photos of OSH-MPT prototypes on a ferromagnetic plate with and without a magnet.

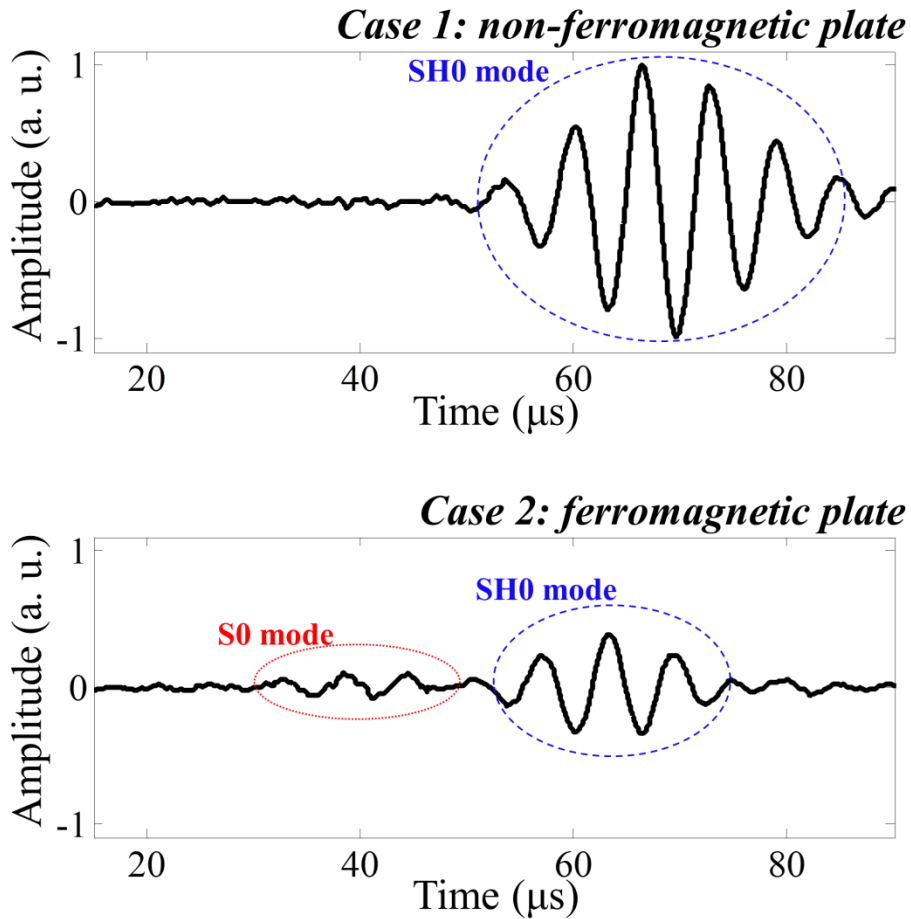


Fig. 3.18 Experimentally measured signals using a pair of OSH-MPTs installed on a non-ferromagnetic (aluminum) and a ferromagnetic (AISI1008) plate in the pitch catch manner, respectively. For the ferromagnetic plate (Case 2), the amplitude of the SH0 mode substantially decreased and the unwanted S0 mode was measured.

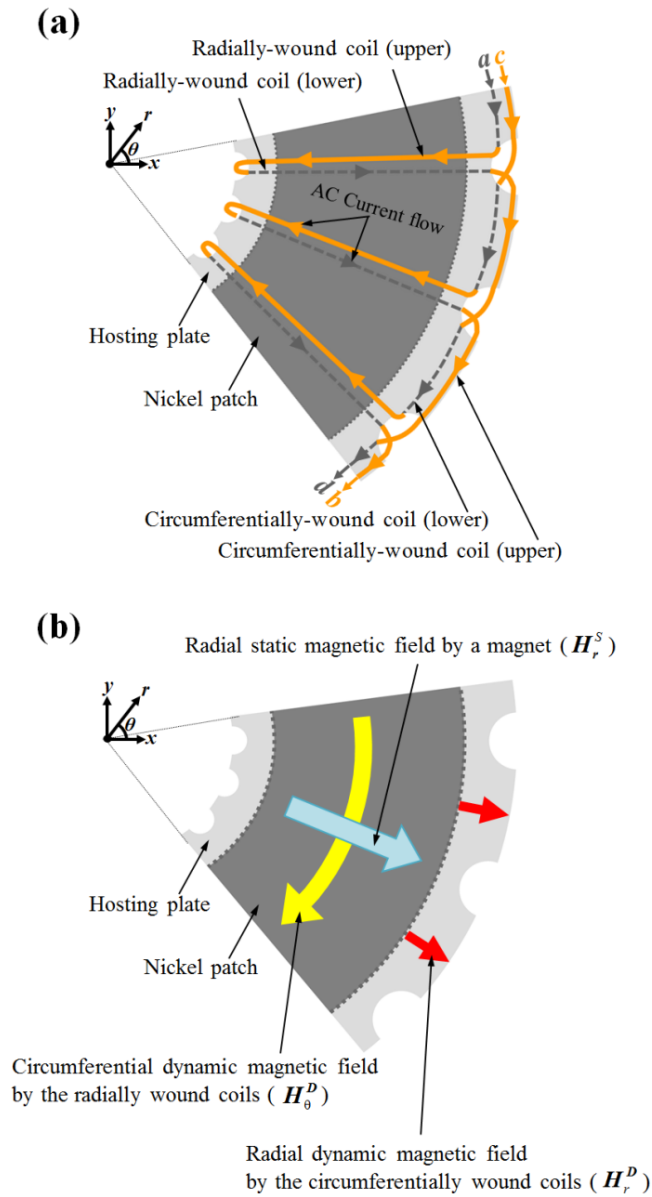


Fig. 3.19 Detailed drawings of part A shown in Fig. 3.16 (a). Specific coil configuration and current flow in the coil are indicated. (b) The several types of magnetic fields generated by the magnet and coils are illustrated.

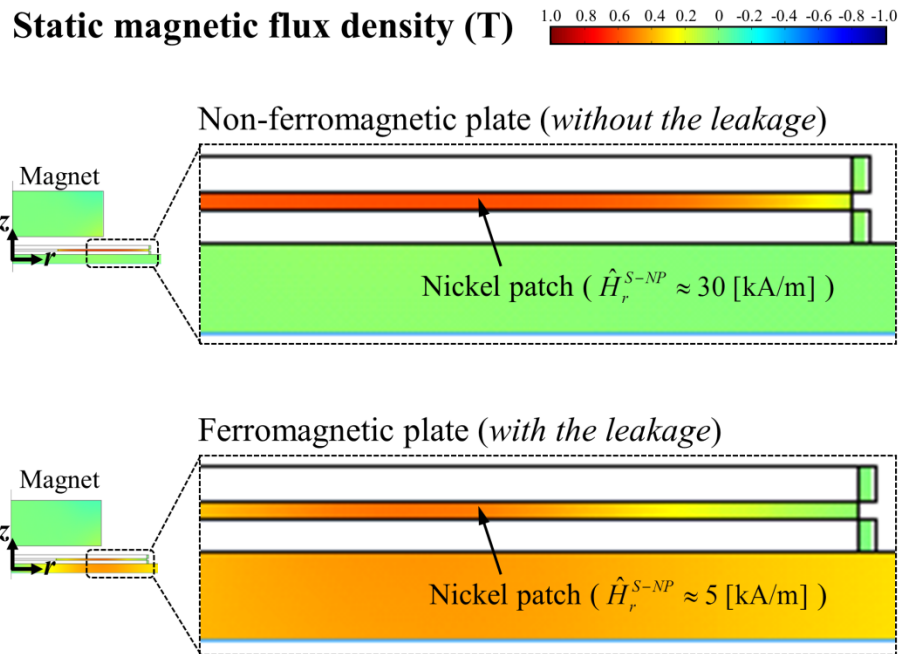


Fig. 3.20 Numerical simulation results for the static magnetic field of the OSH-MPTs installed on a nonferromagnetic and a ferromagnetic plate, respectively. Owing to the leakage, the averaged value of the radial static magnetic field in the nickel patch (\hat{H}_r^{S-NP}) placed on the ferromagnetic plate is smaller than that in the patch placed on the nonferromagnetic plate

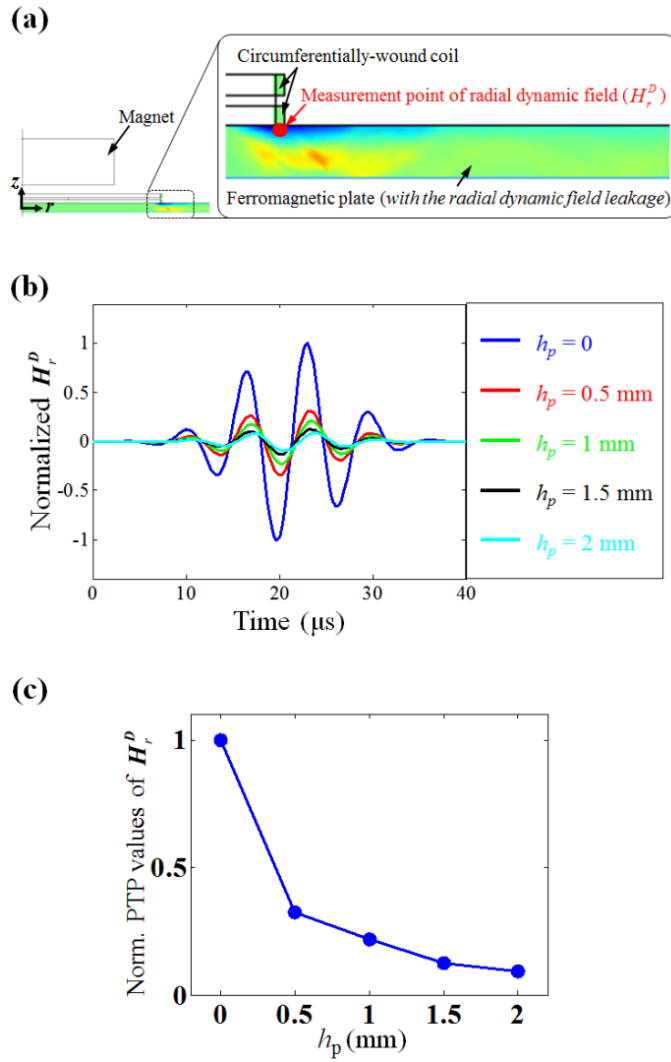


Fig. 3.21 (a) Numerical simulation results for the radial dynamic magnetic field (H_r^D) generated by only the circumferentially wound coil of the OSH-MPT (150 kHz, $D=10$ mm) placed on the ferromagnetic plate. (b) Normalized signals of H_r^D at the measurement point indicated by the red dot in Fig. 3.20 (a) and (b) its peak-to-peak values for various h_p values.

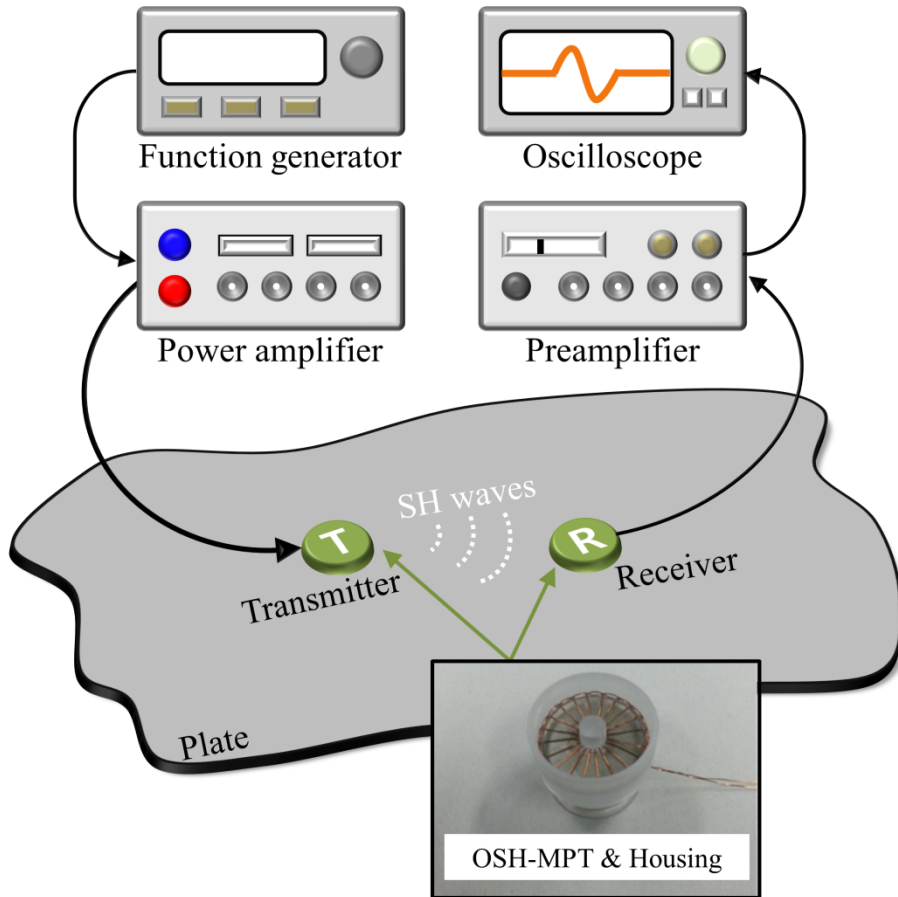


Fig. 3.22 Experimental setup for the SH wave transduction using a pair of OSH-MPTs in the pitch-catch manner. A photo in the inset shows the specially fabricated housing to accurately control the thickness of the bonding layer (epoxy resin) between the patch and the plate.

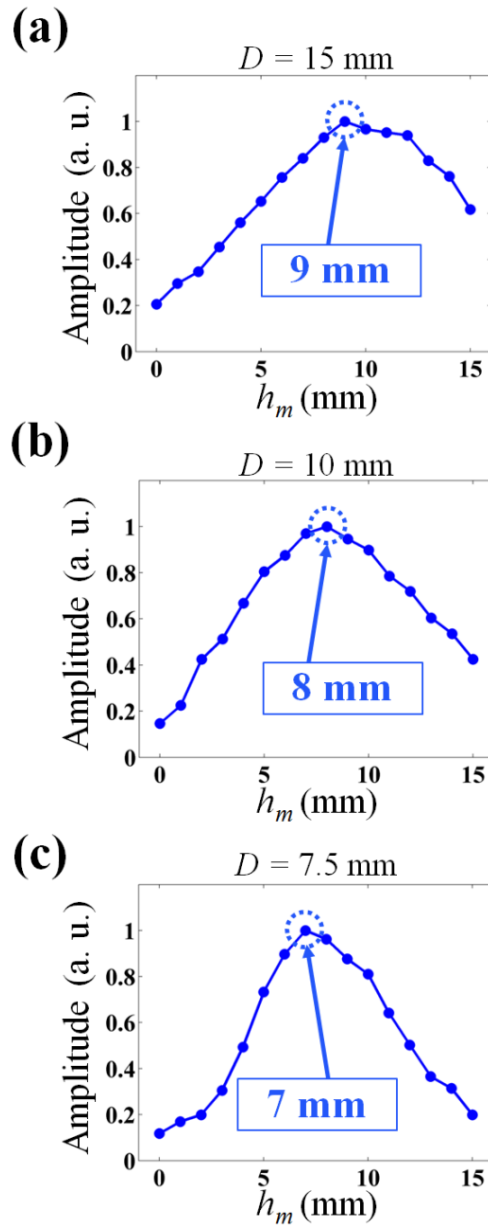


Fig. 3.23 Amplitude variation of measured SH waves using the three different sizes of OSH-MPTs installed on a nonferromagnetic plate. The peak values for each case are marked by the dotted circles.

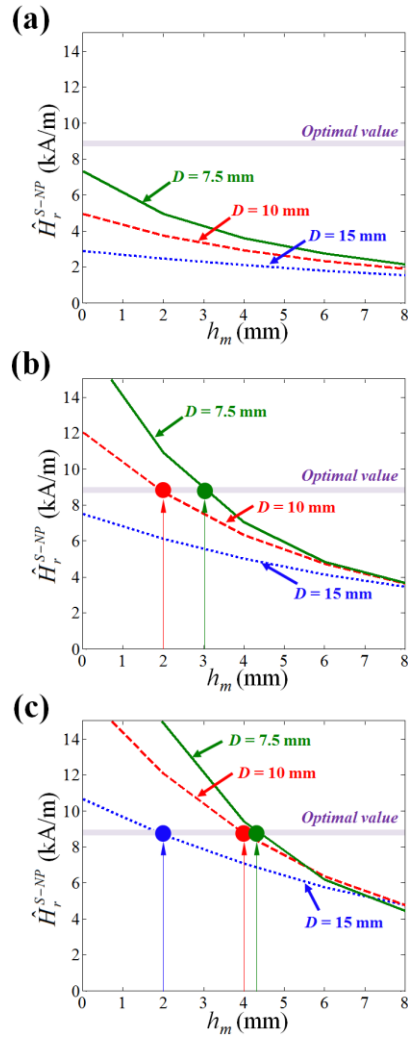


Fig. 3.24 Numerical simulation results for the \hat{H}_r^{S-NP} values of the OSH-MPTs placed on the ferromagnetic plate for different D and various h_m values when (a) $h_p = 0$, (b) 1.0 mm and (c) 2.0 mm. The optimal value listed in Table 3.2 (${}^* \hat{H}_r^{S-NP}$) is denoted by the purple horizontal line. The solid dots denote the points of the optimal combinations of (h_p, h_m) yielding ${}^* \hat{H}_r^{S-NP}$.

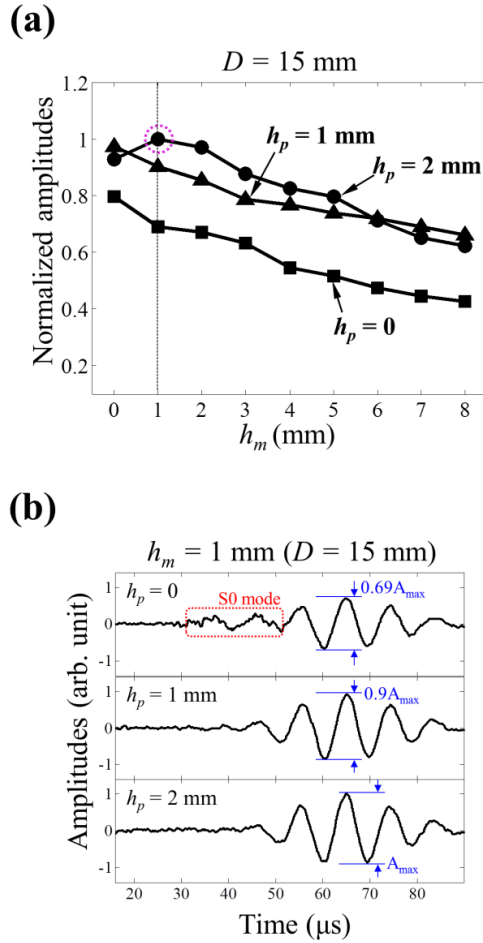


Fig. 3.25 Experimental results for the OSH-MPT ($D = 15 \text{ mm}$). (a) Normalized Peak-to-peak values are shown. The optimal combination of h_p and h_m from the simulation results are indicated by the dotted circles. The time signals for the fixed h_m values (shown as a dashed vertical line) are also shown in (b). At the optimal condition, not only is the SH mode enhanced, but the S0 mode is also greatly suppressed. The A_{\max} is the largest value of the SH0 mode at the optimal condition for comparing the transduction efficiency with those from other cases.

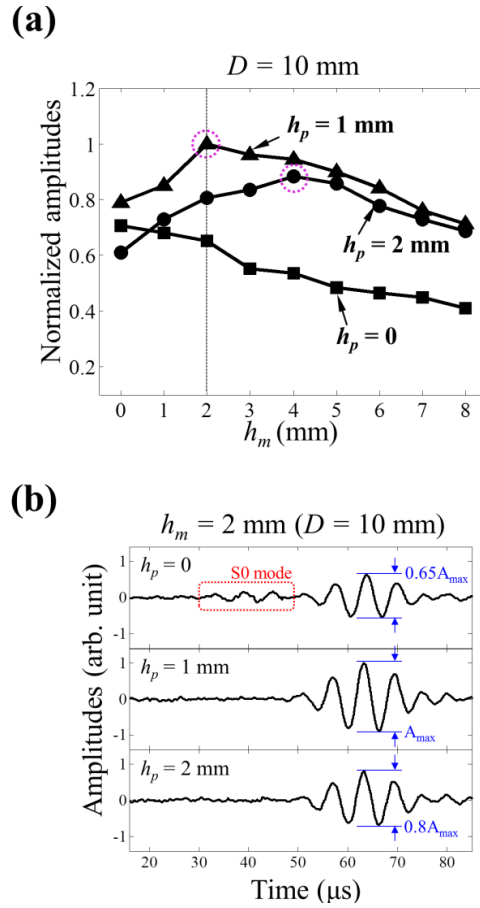


Fig. 3.26 Experimental results for the OSH-MPT ($D = 10 \text{ mm}$). (a) Normalized Peak-to-peak values are shown. The optimal combination of h_p and h_m from the simulation results are indicated by the dotted circles. The time signals for the fixed h_m values (shown as a dashed vertical line) are also shown in (b). At the optimal condition, not only is the SH mode enhanced, but the S0 mode is also greatly suppressed. The A_{\max} is the largest value of the SH0 mode at the optimal condition for comparing the transduction efficiency with those from other cases.

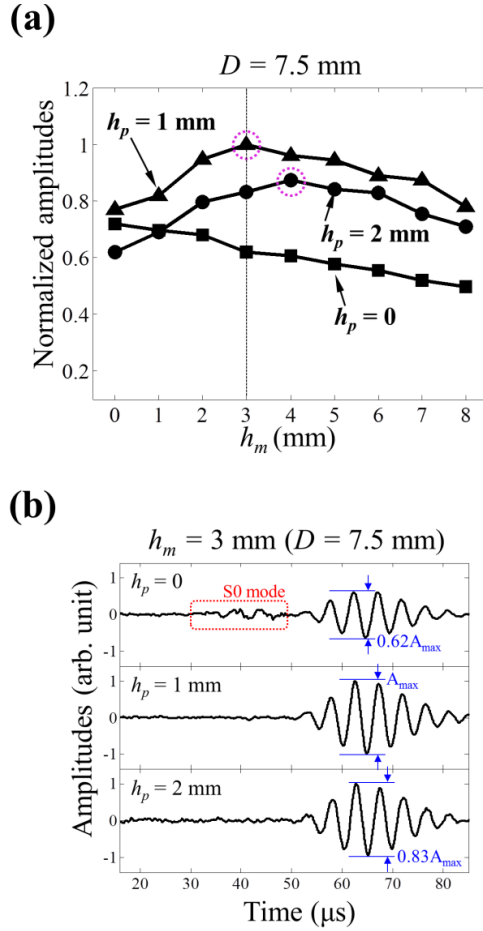


Fig. 3.27 Experimental results for the OSH-MPT ($D = 7.5 \text{ mm}$). (a) Normalized Peak-to-peak values are shown. The optimal combination of h_p and h_m from the simulation results are indicated by the dotted circles. The time signals for the fixed h_m values (shown as a dashed vertical line) are also shown in (b). At the optimal condition, not only is the SH mode enhanced, but the S0 mode is also greatly suppressed. The A_{max} is the largest value of the SH0 mode at the optimal condition for comparing the transduction efficiency with those from other cases.

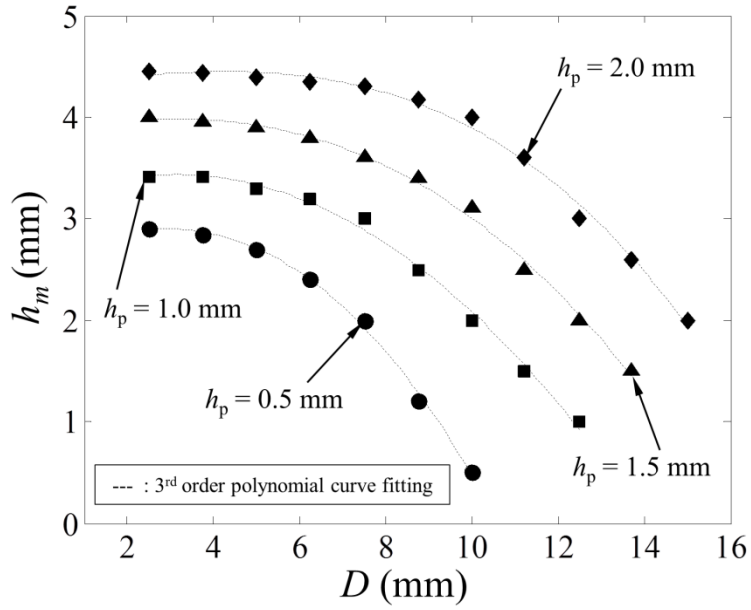


Fig. 3.28 The numerical simulation results of the optimal combination of h_p and h_m (satisfying $^* \hat{H}_r^{S-NP}$ value) for various D values. The corresponding frequency range for the used D values is approximately from 100 kHz to 600 kHz.

CHAPTER 4

OMNIDIRECTIONAL SHEAR-HORIZONTAL WAVE ELECTROMAGNETIC ACOUSTIC TRANSDUCER (OSH-EMAT)

4.1 Overview

This chapter newly proposes an electromagnetic acoustic transducer (EMAT) for generation and measurement of omnidirectional shear-horizontal (SH) guided waves in a metallic plate. While various EMAT configurations are previously developed, there is no omnidirectional SH wave EMAT so far. The proposed EMAT requires a magnetic circuit configuration that allows uniform SH wave transduction in all direction. The EMAT consists of a pair of ring-type permanent magnets that supply static magnetic fluxes and a specially wound coil that induces eddy currents in a plate. The cross product of the static magnetic flux by the magnet in the vertical direction and the induced eddy current by the coil in the

radial direction generates the Lorentz force acting along the circumferential direction, resulting in the generation of omnidirectional SH waves in a metallic plate. To maximize the transducer output at given excitation frequencies, optimal EMAT configurations are determined by numerical simulations and validated by experiments. The omnidirectivity of the proposed EMAT is also confirmed by the simulations and experiments.

The inspection of large plate structures using ultrasonic guided waves is very useful and active in nondestructive evaluation (NDE) and structural health monitoring (SHM) fields because a guided wave based inspection covers a wide range of a structure with a single installation of guided wave transducers and thus detects defects efficiently [1, 12, 47, 50]. The research in this chapter is concerned with a new development of an omnidirectional SH guided wave EMAT which can be used to form a phased array system for plate inspections. The advantage of using omnidirectional guided waves for the phased array system is reported in [18, 19]; it is easy to focus wave energy at any point on a plate when omnidirectional transducers are used.

An omnidirectional transducer must generate and measure a desired guided wave mode uniformly in all directions. Therefore, many investigations are concerned with the development of various omnidirectional guided wave transducers using piezoelectric elements [24-28], magnetostrictive patches [35, 64, 95, 97] and the

electromagnetic acoustic principle [29-34]. Among these transducers, EMATs operated by the Lorentz force mechanism [44] allow noncontact transduction of guided waves in metallic plates. In other words, EMATs do not require any physical contact or bonding layers to transmit wave energy from the transducers to plates. Therefore, EMATs are much preferred for most applications as long as they are applicable. Various practical applications using EMATs can be found in [74-79].

At this point, it is noted again that in all of previously developed omnidirectional EMATs employ the Lamb wave mode only; however, there exists an alternative wave mode, the SH wave mode to be considered. As shown in Fig. 4.1 (a), there exist more than two wave modes for any frequency in the Lamb wave case and they are dispersive for all frequency range. Consequently, dispersion compensation may be necessary for accurate signal processing [51] and wave mode interference may occur [52]. On the other hand, as indicated in Fig. 4.1 (b), there only exists a single nondispersive wave mode (SH₀ mode) for a certain frequency range if the shear-horizontal wave is used [98, 103]. Some cumbersome difficulties inherent in using Lamb waves can be avoided if the fundamental SH wave mode (SH₀ mode) is utilized. Hence, the aim of this investigation is to newly propose an omnidirectional SH wave EMAT.

4.2 Fundamentals of OSH-EMAT

Fig. 4.2 (b) shows the photo of the proposed omnidirectional SH wave EMAT [104, 105]. It generates SH waves omnidirectionally from the center of the EMAT when it is installed on a metallic plate. In developing the proposed EMAT, the key is how to design its magnetic circuit so that it can generate and measure SH wave omnidirectionally. The details of the proposed magnetic circuit configuration and coil winding strategy will be explained in Subsection 4.3.1. Here, it is noted that the proposed EMAT consists of a pair of ring type permanent magnets and a specially wound coil.

In the following subsequent subsections, the detailed configuration of the proposed EMAT along with its working principle is presented first. Then numerical studies are performed to investigate the omnidirectivity of the generated SH waves by the EMAT. Furthermore, the frequency characteristics of the proposed EMAT are studied. By doing so, the relation between the magnet size and the corresponding wavelength of the SH wave is found. Experiments are also performed with the proposed EMATs of three different sizes that are determined by the proposed magnet size-wavelength relation. Through the experiments, various transducer performances, including omnidirectivity, are successfully verified. The experimental findings are compared with the predictions by numerical simulations. The proposed EMAT will be called OSH-EMAT (Omnidirectional Shear-

Horizontal ElectroMagnetic Acoustic Transducer) in the subsequent subsections.

4.2.1 Configuration and coil winding

In this subsection, the detailed configuration of the newly proposed OSH-EMAT is described. After presenting the key components of the OSH-EMAT such as the magnets and coil, the explanation that how the Lorentz forces are developed by the proposed magnetic circuit and generate omnidirectional SH waves in a plate will be addressed.

As shown in Fig. 4.2, the proposed OSH-EMAT consists of two ring magnets and a toroidal coil wound over the magnets. A smaller inner ring magnet (Magnet 1) is inserted inside of a larger outer ring magnet (Magnet 2). The width of both magnets is the same and the outer diameter of Magnet 1 is almost equal to the inner diameter of Magnet 2. Fig. 4.4 sketches the polarization of two ring magnets and the current direction in the toroidal coil. It should be noted that the two magnets are polarized oppositely. The coil is radially wound on the magnets and extended along the circumferential direction [104, 105] as shown in Fig. 4.3 (a). The circumferentially extended parts of coils are attached to the side of Magnet 2. Fig. 4.3 (b) shows the wound coil on the ring magnets after the winding is finished. Although the details are not shown here, to facilitate coil winding, a thin hosting plastic guide having uniform notches along the circumference is placed on the top

surface of the two magnets.

4.2.2 Working principle

Fig. 4.4 describes how the Lorentz forces acting along the circumferential direction are generated. The reason why the circumferential force is needed to generate omnidirectional SH waves will briefly be introduced in Section 4.3. Now, the working principle of the proposed EMAT should be explained. Because EMATs generate guided waves through the Lorentz force, the well-known formula of the Lorentz force mechanism [44] is considered which can be written as

$$\vec{j} = \vec{J} \wedge \vec{D}, \quad (4.1)$$

where \vec{j} , \vec{J} and \vec{D} are the Lorentz force, the induced eddy current density and the static magnetic flux density, respectively. As illustrated in Fig. 4.4, the ring magnets supply the static magnetic flux as marked by dotted lines. Especially in the skin depth layer of a metallic plate, the applied static magnetic flux (B_z^s) directs in the z direction. Because the polarities of the inner and outer magnets are opposite each other, the magnetic flux directions below the two magnets are opposite. If the current direction in the toroidal coil is the direction indicated by a solid complete line, the eddy current (J_r^e) in the radial direction is induced in the skin depth layer

of a metallic plate. Then by using Eq. (4.1), the induced Lorentz force becomes:

$$\vec{J} = J_r \vec{e}_r + J_z \vec{e}_z + J_\theta \vec{e}_\theta, \quad (4.2)$$

where \vec{e}_r , \vec{e}_z and \vec{e}_θ are the unit vectors in the radial, axial and circumferential directions. Therefore, the component of the induced Lorentz force f_θ^L in the circumferential direction (circumferential component) is:

$$f_\theta^L = J_r^c B_z^s. \quad (4.3)$$

Note that f_θ^L can be assumed to be a uniformly distributed force along the circumferential direction as long as the winding distance in the circumferential direction of the toroidal coil is small, as suggested in Fig. 4.3 (b). Because the generated Lorentz forces act perpendicular to the propagation direction (\vec{e}_r), the generated wave by the OSH-EMAT is an omnidirectional shear-horizontal wave. The width (a) of the two magnets may be so adjusted that the resulting constructive interference becomes maximized to obtain the largest output signal at a given center frequency of excitation. The determination of the width a is discussed in the next section.

So far, the SH wave generation mechanism of the OSH-EMAT is explained. Now, the EMAT for measuring SH waves is considered as a sensor. In this case, the inversed Lorentz force mechanism is applied [44]. It can be expressed as

$$\vec{J} = \gamma \vec{v} \times \vec{B}, \quad (4.4)$$

where \vec{J} and \vec{v} are the induced current density in the receiving EMAT and the velocity of a particle in a metallic plate subjected to the static magnetic flux \vec{B} , respectively. The symbol γ denotes the electrical conductivity of the plate. If $\vec{v} = v_{\theta} \vec{e}_{\theta}$ and $\vec{B} = B_z \vec{e}_z$, \vec{J} will become $\vec{J} = J_r \vec{e}_r = \gamma v_{\theta} B_z \vec{e}_r$. Therefore, the circumferential particle motion resulting from an omnidirectional SH wave induces the current density in the coil of the receiving EMAT.

4.3 Design of OSH-EMAT

The proposed OSH-EMAT is designed to generate and measure omnidirectional SH waves in a metallic plate as conceptually illustrated in Fig. 4.5. To this end, an axisymmetric configured transducer that can be installed on a plate is needed without bonding layers so that the noncontact transduction of guided wave is realized. The induced force by the axisymmetric transducer should be formed in the circumferential direction. In other words, the circular force is applied to the plate

for the generation of omnidirectional SH waves. Therefore, the transducer is designed according to these features. This section mainly presents the detailed design process of the OSH-MPT by simulations considering target frequencies. To check the omnidirectional SH wave transduction first using the EMAT by simulations, a finite element model is developed and numerical calculations are carried out. Further numerical simulations are carried out to find the relation between the magnet size and the wavelength of the SH₀ wave mode. Note that the operating frequency is assumed be lower than the first cutoff frequency of the SH wave modes.

4.3.1 Design issue on the magnet size and wavelength

Before presenting the simulation results of the developed OSH-EMATs, it is worth comparing generation mechanisms of EMATs for unidirectional and omnidirectional SH wave cases, respectively. Figs. 4.6 and 4.7 sketch how unidirectional and omnidirectional SH waves in a metallic plate are generated by EMATs. To facilitate the comparison, coils are not sketched but the induced eddy currents by the coil in a plate are depicted. For unidirectional SH wave transduction, the EMAT is equipped with a pair of rectangular magnets having different polarization as suggested in Fig. 4.6. Assuming that the coil is so wound that the eddy current as indicated in Fig. 4.6 is induced, the Lorentz force in the y direction is generated. The resulting wave is an SH wave propagating along the x

direction. If the width of the two magnets (a) is chosen to be equal to the wavelength of the SH wave (λ_{SH}) for a target excitation frequency [93], i.e. if the magnet size holds the relation $a \approx \lambda_{\text{SH}}$, the output of the unidirectional EMAT will be maximized.

In case of the omnidirectional SH wave EMAT (OSH-EMAT), two sets of the generated Lorentz forces in the θ direction are axisymmetric, as sketched in Fig. 4.7. It is reported earlier in [106] that in annular array type transducers, such as the proposed OSH-EMAT, $a \approx \lambda_{\text{SH}}$ does not hold because of uneven mutual interference between outward and inward waves generated by transducer elements of different radii. Therefore, some modification is needed to determine the optimal width (a) of the two ring magnets that maximizes the EMAT output for a given center frequency or wavelength (λ_{SH}) in a test plate as

$$a \approx s\lambda_{\text{SH}}, \quad (4.5)$$

where s is a scaling factor. The value of the scaling factor s is dominantly dependent on the inner radius (r_i) of the inner ring magnet [106]. Note that it is assumed that there is no gap between the two ring magnets in the case of OSH-EMATs.

4.3.2 Transducer design by simulations

In this subsection, numerical simulations for wave transduction by the OSH-EMAT are performed. For the simulation, a commercial finite element package, COMSOL Multiphysics 3.5a [88] is used. The three-dimensional finite element model of the EMAT is depicted on the top figure of Fig. 4.8; both the transmitting and receiving EMATs are modeled and they are assumed to be installed on a 1 mm thick aluminum plate. Note that aluminum plates are preferred for the transduction of guided wave using EMATs because of its relatively great conductivity among generally used metal materials. The coil is modeled by a thin copper annular plate. The AC current in the coil-simulating plate is set to flow radially outward. Because the coil underneath the magnets contributes to the radial eddy current generation, only this part is modeled by a thin annular plate. This is a reasonable approach if the radial distance between each wound coil of the fabricated EMAT is sufficiently small to generate uniform eddy current in the radial direction. The pitch-catch type wave transduction is simulated by transient finite element analysis. The input current into the coil of the transmitting EMAT is a Gabor pulse [87], expressed as

$$f_G(t) = e^{-\frac{t^2}{2\sigma^2} + j(2\pi\eta t)}, \quad (4.6)$$

where σ is the spread in the time axis. The symbols η and t denote the center frequency of the excitation pulse and the time, respectively.

Now, the numerical simulation results obtained for the input Gabor pulse are presented. For simulations, the following EMAT configurations are taken. First, two ring magnets are employed for all OSH-EMATs. Second, $r_i = 0.25a$ is chosen to facilitate coil winding and standardization. Because the scaling factor is varied depending both on a and r_i , it is convenient to work with only one parameter by setting $r_i = 0.25a$. For simulations, the following five cases are considered with $r_i = 0.25a$ as

Case 1: $(a, r_i) = (30 \text{ mm}, 7.5 \text{ mm})$,

Case 2: $(a, r_i) = (25 \text{ mm}, 6.25 \text{ mm})$,

Case 3: $(a, r_i) = (20 \text{ mm}, 5 \text{ mm})$,

Case 4: $(a, r_i) = (15 \text{ mm}, 3.75 \text{ mm})$,

Case 5: $(a, r_i) = (10 \text{ mm}, 2.5 \text{ mm})$.

The bottom figure of Fig. 4.8 and Fig. 4.9 (a) show the snapshots of shear strain ($\varepsilon_{r\theta}$) at $t = 20 \mu\text{s}$ and $t = 60 \mu\text{s}$, respectively. The two OSH-EMATs

functioning as a transmitter and a receiver, respectively, are 175 mm apart. From the simulation results, It can be estimated that the wave speed of the generated wave. It is found to be about 3122 m/s, which is almost identical to the theoretical wave speed of the SH0 mode in the used aluminum plate. Although not shown here, the magnitudes of ε_{rr} and $\varepsilon_{\theta\theta}$ (normal strains in the radial and circumferential directions) are found to be negligible compared with that of $\varepsilon_{r\theta}$. The snapshots in Fig. 4.8 and Fig. 4.9 (a) clearly show the propagating SH0 wave in omnidirectional. Although the reflected waves from the boundaries of the aluminum plate are seen from Fig. 4.9 (a), the arrival of the omnidirectional SH wave at the receiver location is apparent. The induced current (J^i) in the receiver coil is also illustrated in the inset of Fig. 4.9 (b). The induced current in the coil represents the measured SH wave signal by the transmitting EMAT.

Fig. 4.10 shows the peak-to-peak values of the measured current density J^i in the receiver coil for a wide range of excitation frequencies. The peak frequency (f_{SH}^{peak}) yielding the largest peak-to-peak values increases as the width (a) of the ring magnets reduces. The peak wavelengths ($\lambda_{SH}^{\text{peak}}$) corresponding to the peak frequencies are also listed in Fig. 6. Table 4.1 lists $\lambda_{SH}^{\text{peak}}$ values from the simulation results. For all cases tested here satisfying $r_i = 0.25a$, the scaling factor s is nearly equal to 0.63, resulting in:

$$a \approx 0.63\lambda_{SH}^{\text{peak}}. \quad (4.7)$$

The scaling factor s will be changed if a different relation between r_i and a is chosen. In the next section, the findings from the numerical simulations are checked by the pitch-catch type experiments in an aluminum plate using the OSH-EMAT.

4.3.3 The effect of magnet width ratio

In this subsection, to examine the effect of magnet width ratio, each width of the ring magnets is varied through numerical simulations. The widths of the inner and outer ring magnets are defined w_1 and w_2 , respectively, as shown in Fig. 4.11. Now, by varying the ratio $r_m = w_1 / w_2$ for the fixed a value, how the performance of the OSH-EMAT changes is studied. For the simulation, OSH-EMAT for Case 3 (tuned for approximately 100 kHz) is considered.

First, the wave transduction simulations for $r_m < 1$ (i.e. inner width is smaller than outer width) are carried out when the excitation frequency is 100 kHz. Fig. 4.12 shows the results and it can be observed that not only the measured signals decrease but the waveforms are highly distorted according to decreasing r_m value

(A_{Ref} refers to the peak-to-peak value of the reference signal at $r_m = 1$). Because the bottom area of the inner magnet is smaller than that of the outer magnet, the symmetry of magnetic flux distribution under the magnets becomes more asymmetric and thus the signal is reduced and distorted. However, in the case of $r_m > 1$ (i.e. inner width is larger than outer width,) the measured signal is similar to the reference signal for slightly increased r_m values as shown in Fig. 4.13. This is because the symmetry of magnetic flux distribution under the magnets becomes more symmetric unlike $r_m < 1$ case. Then, as the r_m value increases more, the measured signals slowly decrease.

Now, the frequency characteristic of the OSH-EMAT for $r_m > 1$ is investigated. In the case of $r_m < 1$, the measured signal is highly reduced and distorted as mentioned above. So, the transducers for $r_m < 1$ case are not suitable for actual applications. Otherwise, because the amplitude variation of the measured signal is very slight for the case of $r_m > 1$, it is worth observing the change of the frequency characteristic. The simulation result for frequency sweep is shown in Fig. 4.14. As it is seen in Fig. 4.14, the peak frequency is shifted to lower frequency range as r_m increases. Therefore, if the value of w_1 is slightly larger than w_2 value, the transducer performance is almost same with the reference case. In other words, in the design process of OSH-EMATs, the value of w_1 should be chosen to

be equal or slightly larger than w_2 so that the transducer output is maximized at the desired frequency. Note that the OSH-EMATs for $r_m = 1$ are only considered in this chapter because of the convenient fabrication.

4.4 Experiments

This section presents experiments performed with the actually fabricated OSH-EMAT. Using the fabricated EMATs of different sizes corresponding to Cases 3 to 5, as introduced in Subsection 4.3.2, SH wave transduction experiments are carried out for various frequencies. For the experiments, the EMATs consist of two ring type NdFeB permanent magnets of 10 mm in height and a copper coil of 0.3 mm in diameter. The coil is wound twice in the radial direction. The radially wound coil is extended in the circumferential direction by connecting each radially wound part as illustrated in Fig. 4.3. The experimental results will be also compared with the simulation results.

4.4.1 SH wave transduction using OSH-EMAT

The experimental setup is shown in Fig. 4.15. As in the numerical simulations in Section 4.3, the two proposed OSH-EMATs having the same configuration are installed on a 1 mm thick aluminum plate as a transmitter and a receiver, respectively. The generated SH wave from the transmitter is propagated and

measured by the receiver located 175 mm away from the transmitter in the pitch-catch manner.

For experiments, the following procedure is taken. The input pulse signal given in Eq. (4.5) is generated by a function generator (33250A, Agilent Technologies Inc., Santa Clara, CA) and amplified by a power amplifier (AG1017L, T&C Power Conversion, Rochester, NY) before being sent to the coil of the transmitting EMAT. The measured SH wave signal in the receiving EMAT is then amplified by a preamplifier (SR560 low-noise pre-amplifier, Stanford Research Systems, Sunnyvale, CA). Then, the amplified SH wave signal is recorded by an oscilloscope (WaveRunner 104MXi-A, LeCroy, Chestnut Ridge, NY).

Fig. 16 (a) shows the time signal of the measured SH0 mode from the experiment using the two EMATs corresponding to Case 4. The center frequency of excitation is 130 kHz. The short time Fourier transform (STFT) [107] of the measured signal is also plotted in Fig. 16 (b). Fig. 16 (b) shows that the generated SH0 mode from the transmitter is measured with its energy concentrated at the actuation frequency, 130 kHz. The reflected SH0 mode from the nearest plate boundary is also shown at around $t = 120 \mu\text{s}$. The plate dimension used in the experiment is 1000 mm \times 600 mm. Note that the locations of the EMATs are intentionally adjusted to efficiently measure the reflected wave. The calculated group velocity of the measured SH0 mode using the distance between the two EMATs and the arrival

time is almost equal to 3122 m/s, which confirms the proper transduction of the desired SH0 mode at the excitation frequency.

4.4.2 Frequency characteristic

Here, the experimental investigation for verifying that the relation $a \approx 0.63\lambda_{SH}^{peak}$ given by Eq. (4.7) is valid. So, the excitation frequencies are varied and the corresponding peak-to-peak voltage values from the receiving EMAT are collected. The experimental results are marked in dots in each top figure of Figs. 4.17, 4.18 and 4.19 for Case 3, Case 4 and Case 5, respectively. In these figures, the peak frequencies, $f_{SH}^{peak}|_{sim.}$ predicted by the simulation results from Section 4.3 are marked by the vertical dotted line arrows. It shows that the values of $f_{SH}^{peak}|_{sim.}$ agree well with the experimental results. The comparison with the experimental and simulation results in Figs. 4.17, 4.18 and 4.19 suggests that the relation given by Eq. (4.7) is a useful formula to optimally design the OSH-EMATs proposed to generate SH waves in a plate. Moreover, the measured time signals at selected excitation frequencies by the experiments and simulations are also compared on the bottom side of Figs. 4.17, 4.18 and 4.19. Note that the selected excitation frequencies for the signals on the bottom side are chosen to be almost equal to the values of $f_{SH}^{peak}|_{sim.}$ for each case.

4.4.3 Radiation pattern of the SH wave by OSH-EMAT

This subsection presents the experimental results to verify the omnidirectional radiation pattern of the generated and measured SH waves by the OSH-EMAT. To check the omnidirectivity of the EMAT as a transmitter and a receiver, respectively, two sets of experiments described in Fig. 4.20 and Fig. 4.21 are carried out. The EMATs corresponding to Case 4 are used and the excitation frequency is 130 kHz.

In the first experiment as depicted in Fig. 4.20 (a), the omnidirectivity of the OSH-EMAT as a transmitter is investigated. Thus, as shown in Fig. 4.20 (a), the transmitting EMAT is rotated by 180° in an increment of 15° . A magnetostrictive patch transducer (MPT) designed to measure and generate unidirectional SH waves [39, 40, 43] is used as a receiver. Because Refs. [39, 40, 43] explain the working principle and detailed configuration of the MPT employed here, it is only briefly described here. The MPT consists of a thin rectangular nickel patch bonded onto the plate, a pair of rectangular magnets and a figure-of-eight coil. The patch size of the MPT is so determined as to be highly sensitive to the SH wave excited at 130 kHz along a designated direction. The EMAT and the MPT are installed 300 mm away from each other on a 1 mm thick aluminum plate. The wave radiation pattern by the transmitting EMAT is plotted in Fig. 4.20 (b). The measured signals by the MPT at the orientation angles of the OSH-EMAT transmitter, $\theta = 165^\circ$ and $\theta = 75^\circ$, respectively, have the maximum (A_{\max}) and minimum (A_{\min}) amplitudes.

They are plotted in Fig. 4.20 (c). As shown in Fig. 4.20 (c), the difference between A_{\max} and A_{\min} is about 8%. Considering various error sources especially from the fabrication process of the transducers and also from the bonding state between the MPT and the plate, the radiation pattern shown in Fig. 4.20 (b) can be regarded to be omnidirectional.

In the second experiment, the omnidirectivity of the OSH-EMAT as a receiver is investigated; see the experimental setup in Fig. 4.21 (a). This time, the EMAT functions as a receiver and the MPT, as a unidirectional SH wave transmitter. For the radiation pattern experiment, the receiving EMAT is rotated from 0 to 180° in an increment of 15°. The radiation pattern is shown in Fig. 4.21 (b). The difference between the largest amplitude of the measured signal at $\theta = 15^\circ$ and the smallest amplitude at $\theta = 60^\circ$ is about 9%. Fig. 4.21 (c) compares the two signals of the largest and smallest amplitudes. The results in Fig. 4.21 confirm that the OSH-EMAT also works as an omnidirectional SH wave receiver although it has slight fluctuation.

From the radiation pattern experiments, it can be concluded that the newly proposed OSH-EMAT successfully generates and measures omnidirectional SH waves.

4.5 Concluding Remarks

An electromagnetic acoustic transducer (EMAT) capable to generate and measure omnidirectional shear-horizontal (SH) guided waves in a metallic plate is newly developed and tested by numerical simulations and experiments. Compared with available omnidirectional Lamb wave EMATs, the omnidirectional SH wave EMAT (OSH-EMAT) proposed here has a unique magnetic circuit; it uses two ring magnets of opposite polarities over which a toroidal coil is wound. The two magnets produce the static magnetic flux in the thickness direction of a test metallic plate and the coil underneath the bottom of the magnets induces the radially-directing eddy current in the plate. Thus, the uniformly-distributed Lorentz forces are produced in the circumferential direction and generate the omnidirectional SH wave in the plate.

The OSH-EMATs in the frequency range below the first cutoff frequency of the SH wave mode are tested. Great omnidirectivity of the EMAT as a transmitter and a receiver is confirmed numerically and experimentally. The difference between the maximum and minimum amplitudes of the generated SH wave in all direction is found to be less than 9% by transmitting and receiving experiments. The design scheme for maximizing the EMAT output at a given excitation frequency is also suggested and verified by simulations and experiments. By investigating the frequency characteristics of the OSH-EMAT for varying magnet sizes, it is possible

to find a scaling factor between the total width (a) of the two ring magnets and the wavelength (λ_{SH}) of the SH wave that gives the maximum output of the EMAT. If $r_i = 0.25a$ where r_i is the inner radius of the inner ring magnet, the relation is found to be $a \approx 0.63\lambda_{\text{SH}}$, which can be useful to design an omnidirectional SH wave EMAT for a target frequency or wavelength. In the future, It may be considered that the imaging of a damaged plate using an array of the proposed OSH-EMATs.

Table 4.1 The peak wavelengths of SH waves for varying widths of the ring magnets satisfying the condition $r_i = 0.25a$ and the corresponding scaling factor.

Case number	a (mm)	r_i (mm)	$\lambda_{\text{SH}}^{\text{peak}}$ (mm)	s
1	30	7.5	48.03	0.63
2	25	6.25	40.03	0.63
3	20	5	31.54	0.63
4	15	3.75	23.65	0.63
5	10	2.5	15.61	0.64

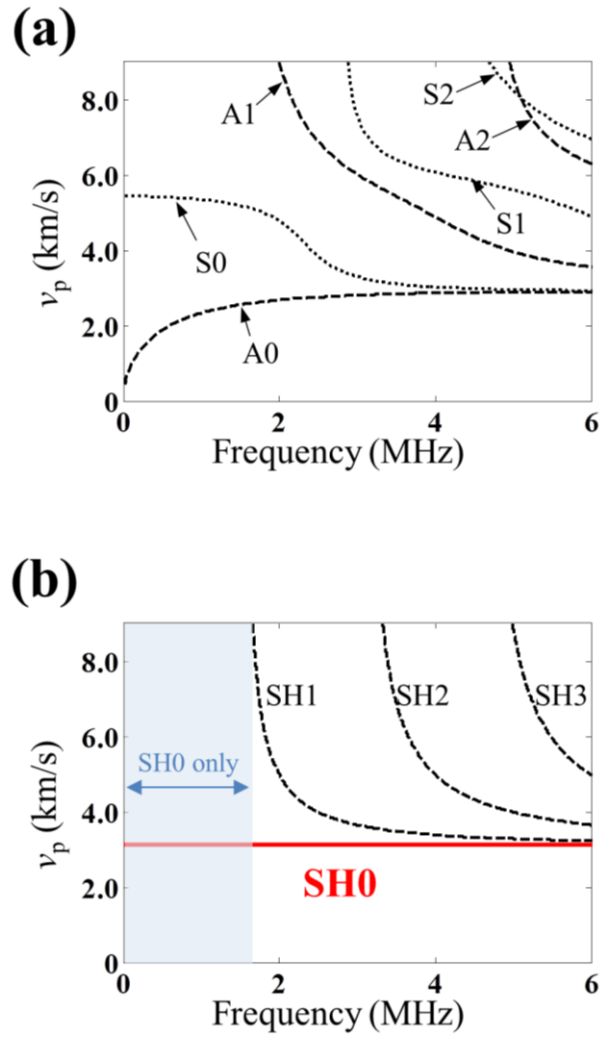


Fig. 4.1 Dispersion curves of phase velocities for (a) Lamb and (b) SH waves in a 1 mm thick aluminum plate.

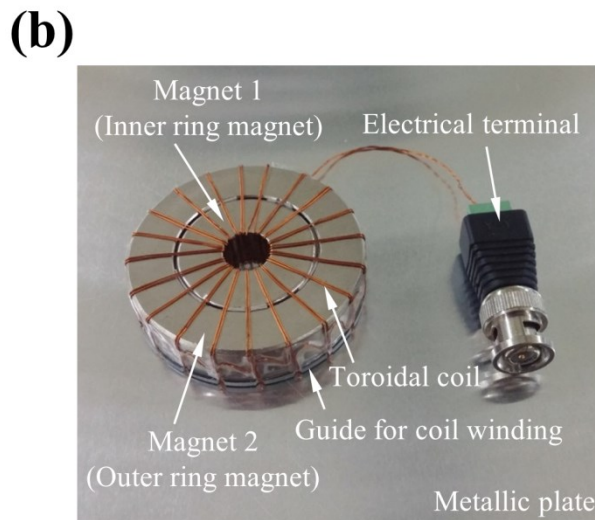
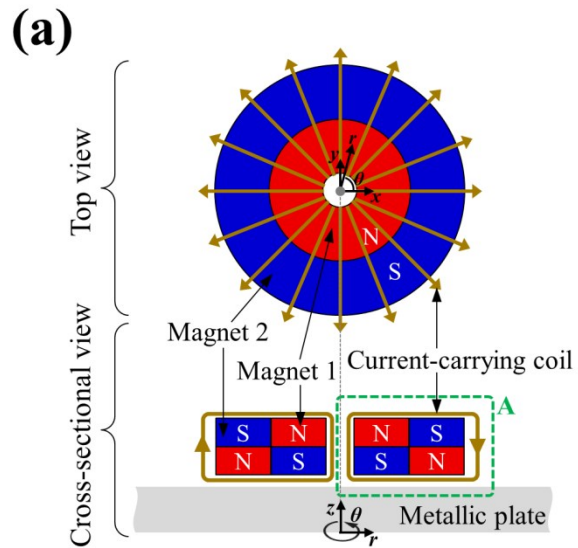
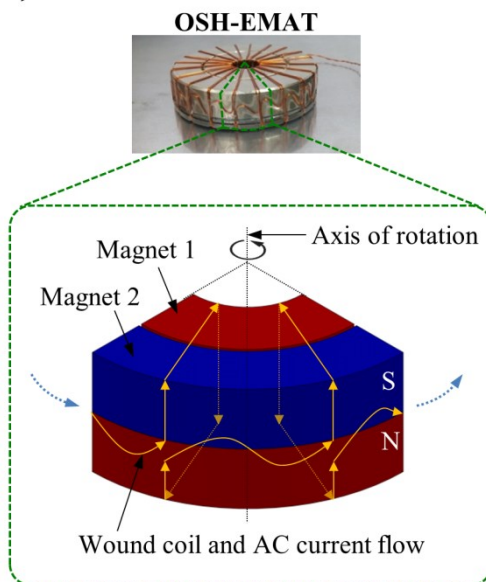


Fig. 4.2 (a) Schematic configuration of the OSH-EMAT in the top and cross-sectional views. (b) Photo of a prototype of the OSH-EMAT placed on an aluminum plate.

(a)



(b)

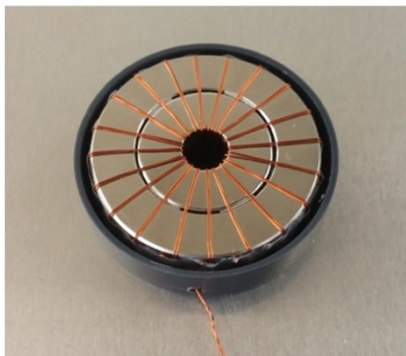


Fig. 4.3 (a) Illustration of coil winding with the direction of AC current flow. (b) Photo of the finished coil winding on the magnets.

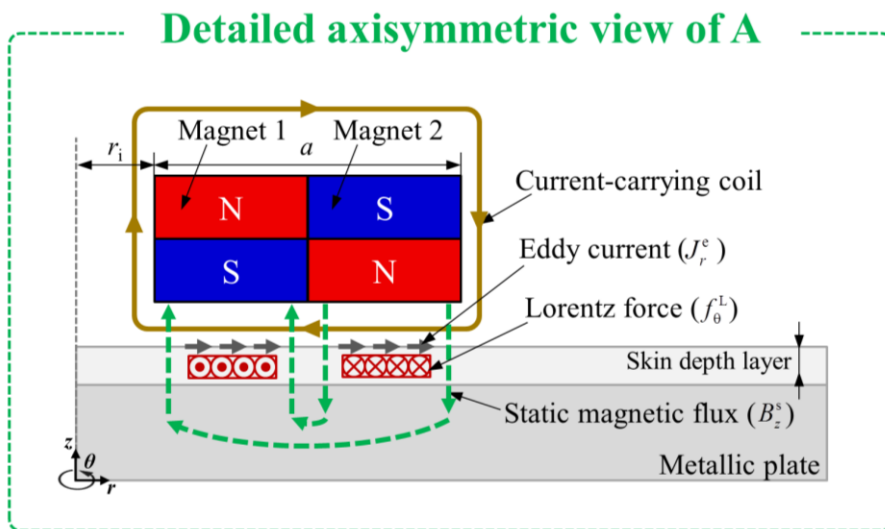


Fig. 4.4 Illustration of the static magnetic flux lines and AC current flow in the coil.

The Lorentz force (f_θ^L) in the circumferential direction generated in the plate is also sketched

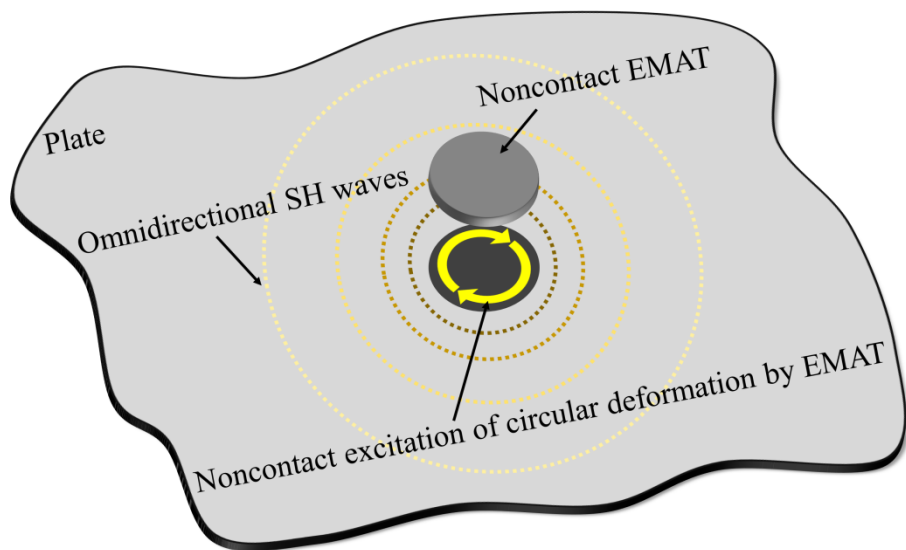


Fig. 4.5 Schematic drawing of a noncontact EMAT that generates omnidirectional SH waves in a metallic plate.

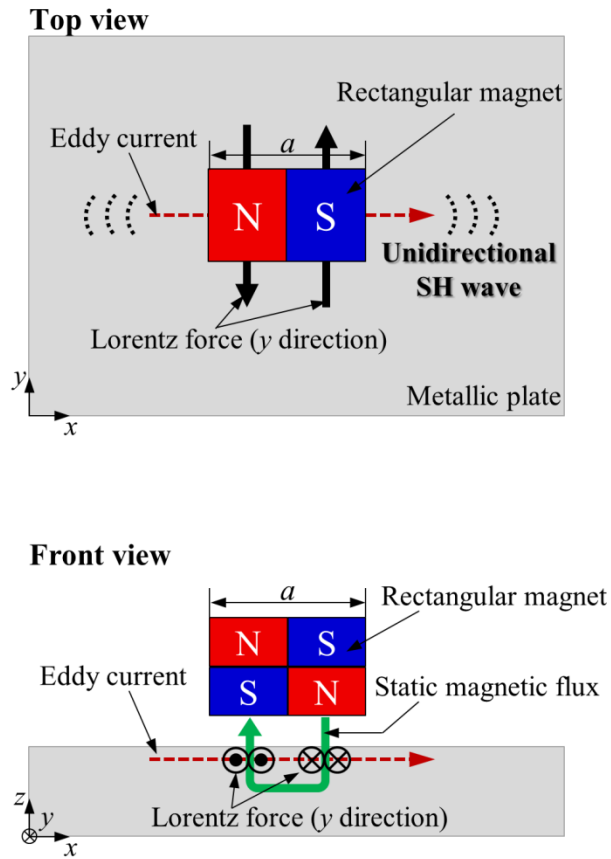


Fig. 4.6 Schematic configurations of the conventional EMAT equipped with rectangular magnets used to generate unidirectional SH waves.

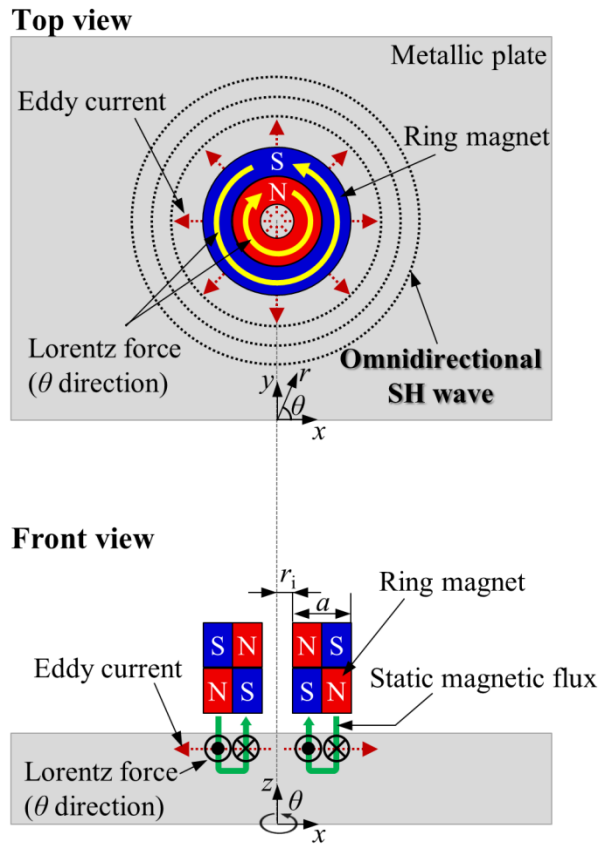


Fig. 4.7 Schematic configurations of the proposed OSH-EMAT equipped with ring magnets developed to generate omnidirectional SH waves.

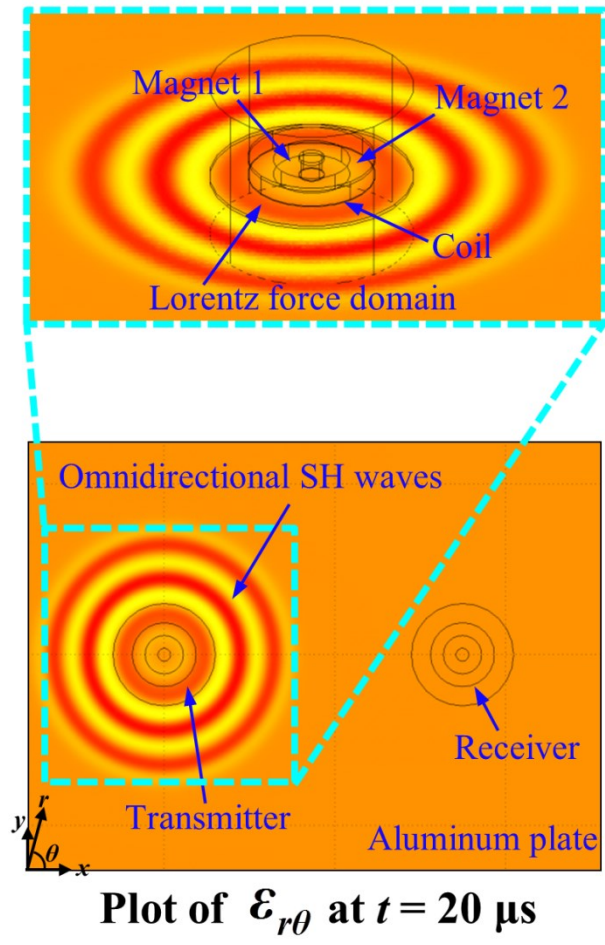
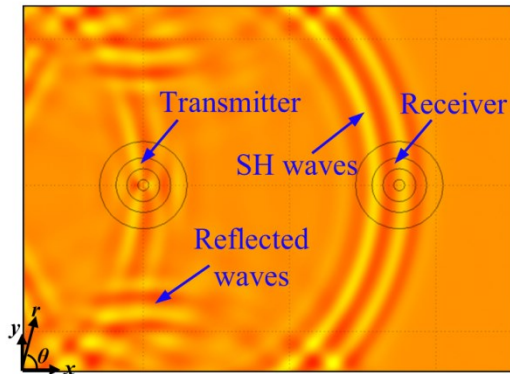


Fig. 4.8 A three-dimensional finite element model of the proposed EMAT and the snapshot of the shear strain ($\epsilon_{r\theta}$) distributions at $t = 20 \mu s$ by time transient simulation.

(a)



Plot of $\epsilon_{r\theta}$ at $t = 60 \mu\text{s}$

(b)

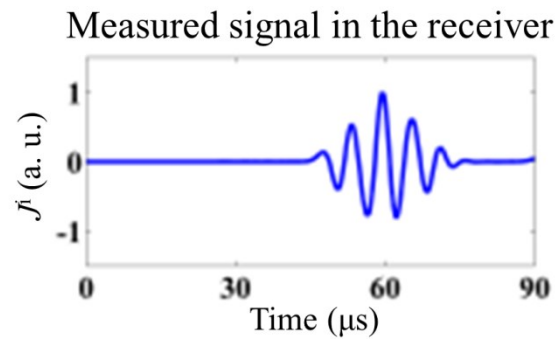


Fig. 4.9 (a) The snapshot of the shear strain ($\epsilon_{r\theta}$) distributions at $t = 60 \mu\text{s}$ by time transient simulation. (b) The signal of the induced current in the receiver coil.

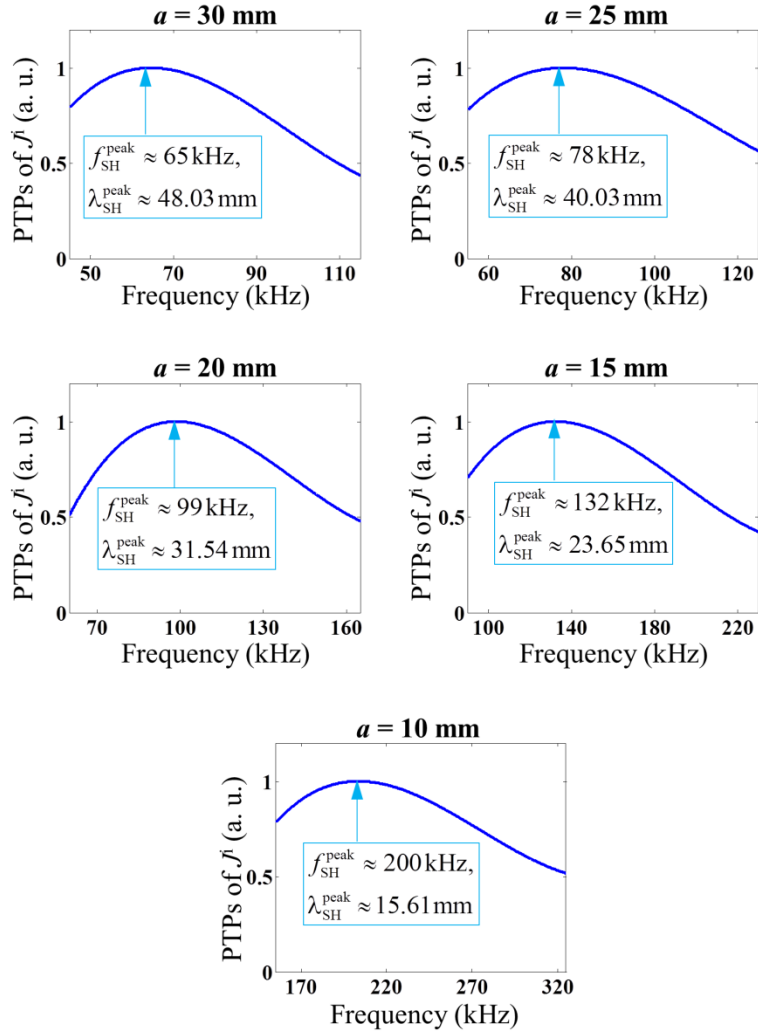


Fig. 4.10 Frequency characteristics of the OSH-EMAT by the simulations for the five cases. PTPs of J^i : the peak-to-peak values of the induced current density in the coil of the receiving EMAT, f_{SH}^{peak} : the peak frequency yielding the largest PTP value, λ_{SH}^{peak} : the peak wavelength of the SH0 wave mode corresponding to

$$f_{SH}^{peak}$$

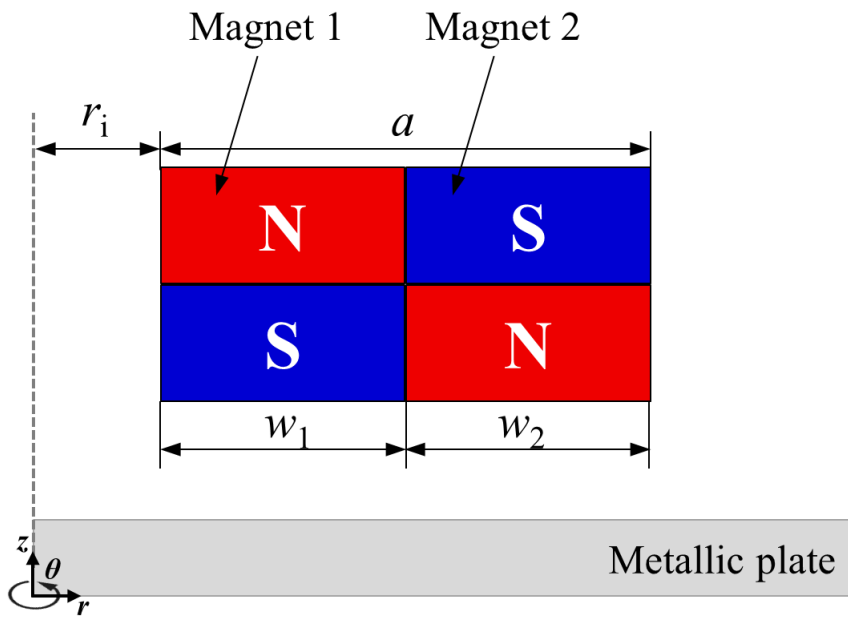


Fig. 4.11 Schematic figure of OSH-EMAT for defining the widths of the inner and outer ring magnets.

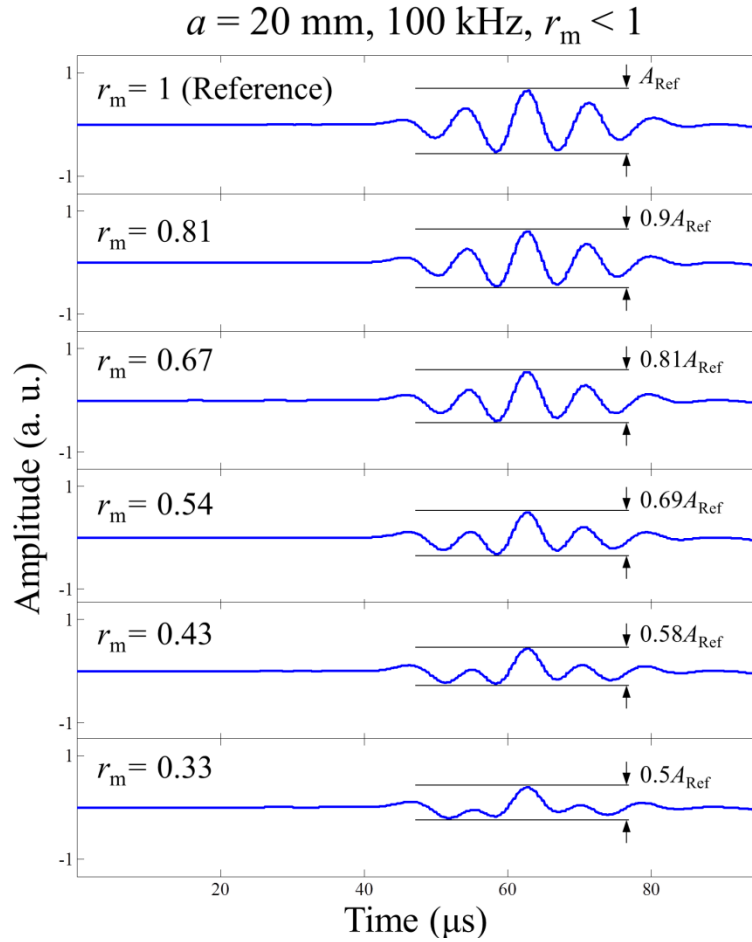


Fig. 4.12 The measured signals by simulations for various r_m values ($r_m = w_1 / w_2$). The simulations are performed for $r_m < 1$ using the OSH-EMAT for Case 3. The symbol A_{Ref} represents the peak-to-peak amplitude of the measured signal for $r_m = 1$ case.

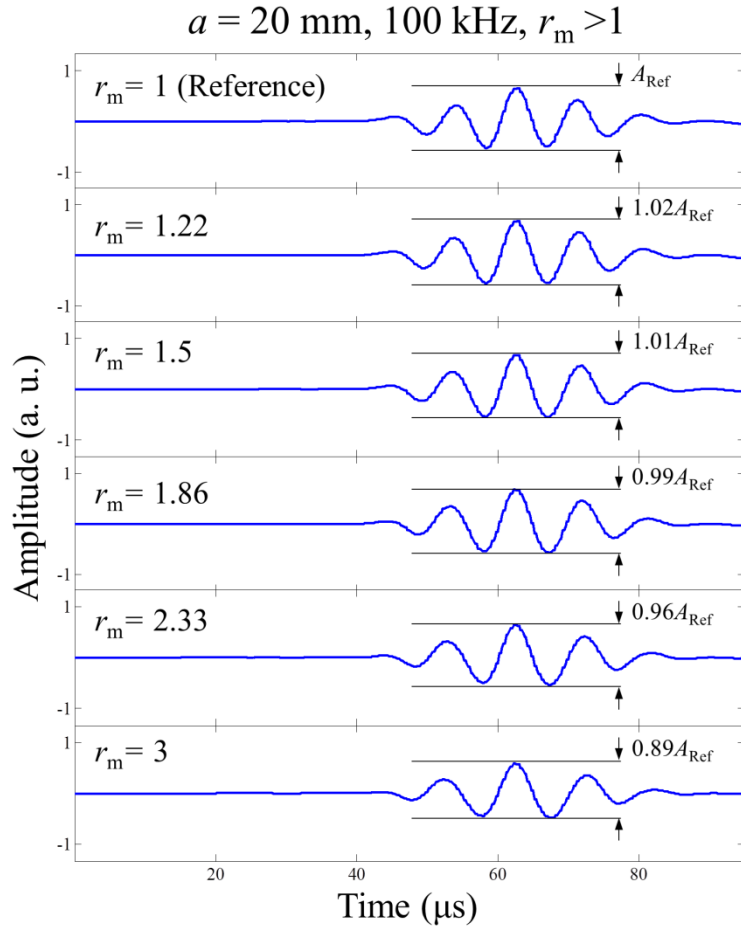


Fig. 4.13 The measured signals by simulations for various r_m values ($r_m = w_1 / w_2$). The simulations are performed for $r_m > 1$ using the OSH-EMAT for Case 3. The symbol A_{Ref} represents the peak-to-peak amplitude of the measured signal for $r_m = 1$ case.

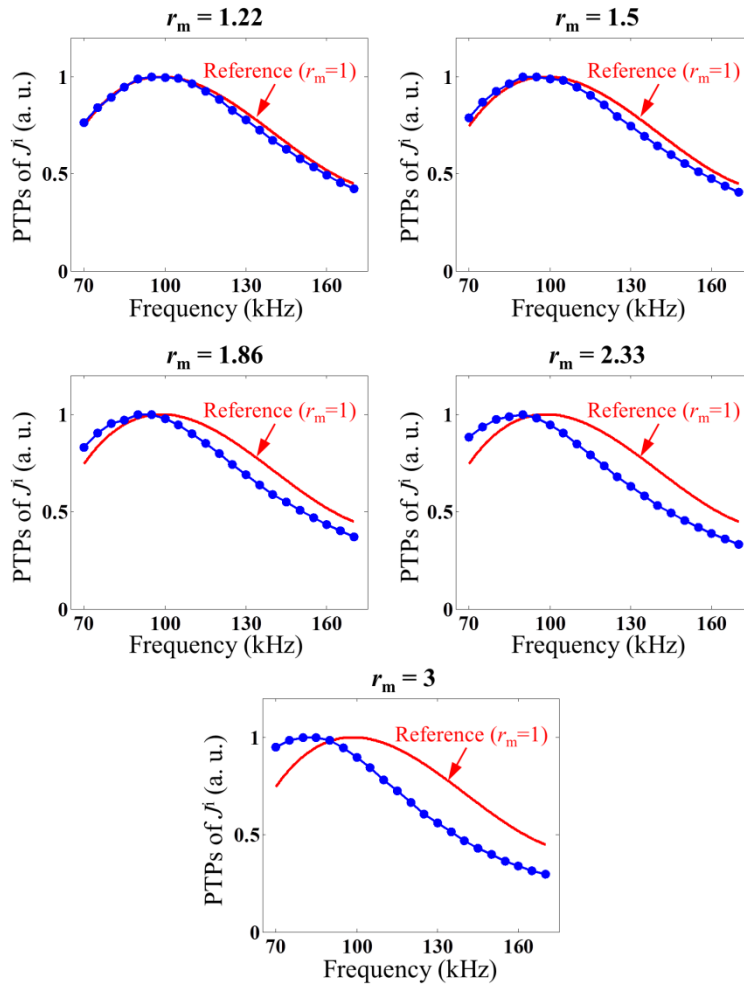


Fig. 4.14 Frequency characteristics calculated by numerical simulations for $r_m > 1$ case. The used OSH-EMAT is Case 3.

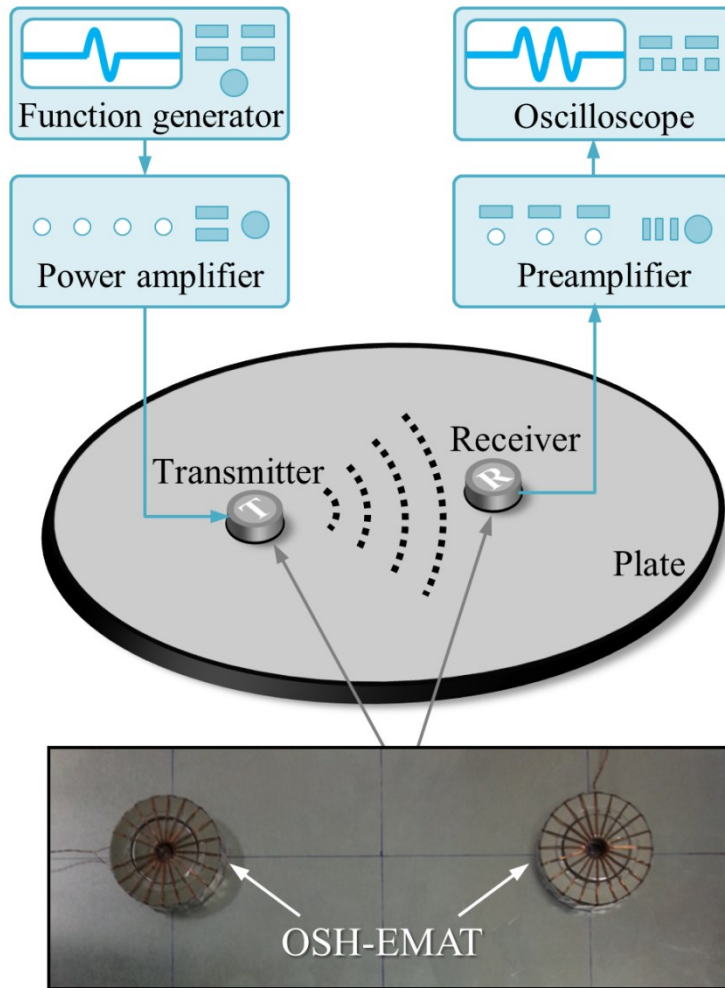
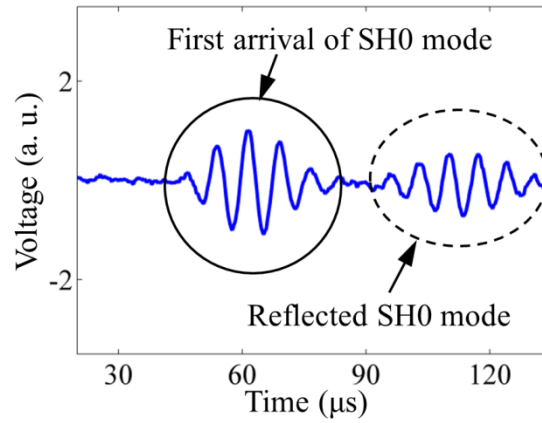


Fig. 4.15 Experimental setup for SH wave transduction using the two OSH-EMATs (one: transmitter, the other: receiver) installed on a 1 mm thick aluminum plate.

(a)



(b)

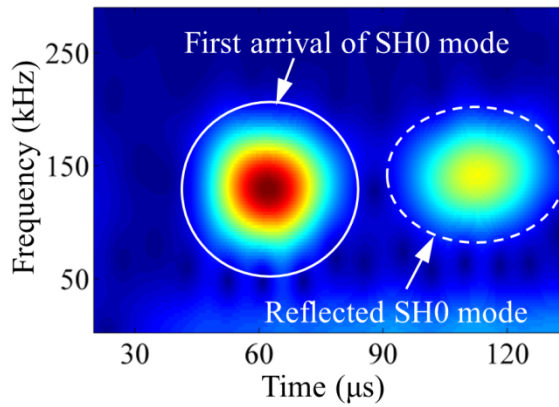


Fig. 4.16 (a) The measured SH0 mode signal by the EMAT at 130 kHz and (b) its short time Fourier transform (STFT) result.

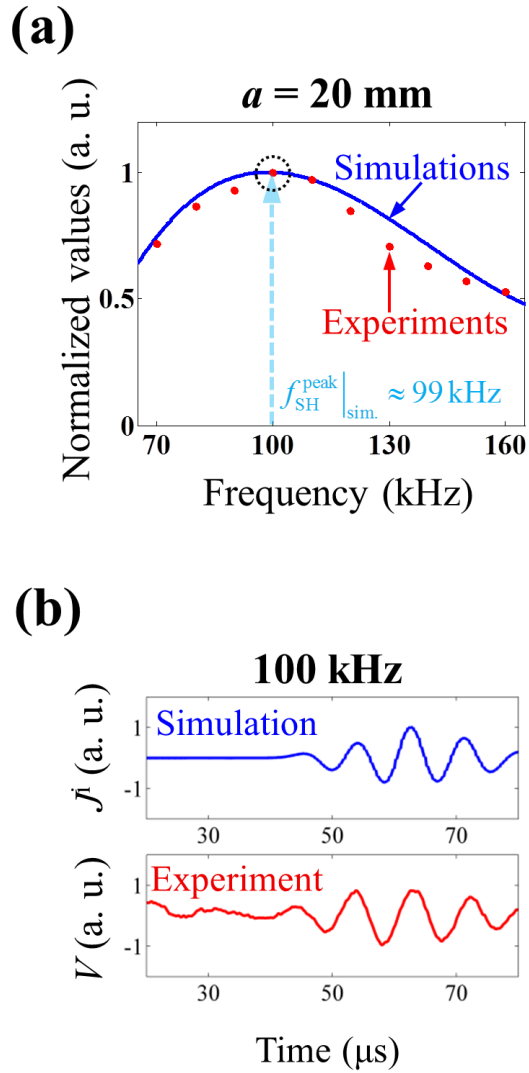


Fig. 4.17 (a) Comparison of the frequency characteristics of the EMATs by experiments and simulations. The width of the two magnets is $a = 20 \text{ mm}$. (b) SH wave signals are chosen at around the peak frequencies ($f_{SH}^{\text{peak}} \Big|_{\text{sim.}}$) as indicated with dotted circles in (a).

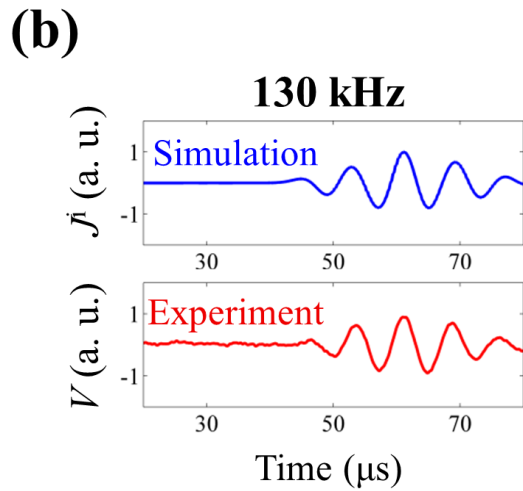
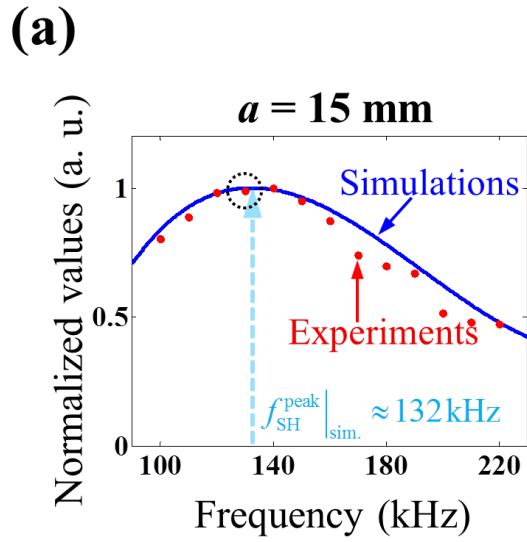


Fig. 4.18 (a) Comparison of the frequency characteristics of the EMATs by experiments and simulations. The width of the two magnets is $a = 15 \text{ mm}$. (b) SH wave signals are chosen at around the peak frequencies ($f_{SH}^{\text{peak}}|_{\text{sim.}}$) as indicated with dotted circles in (a).

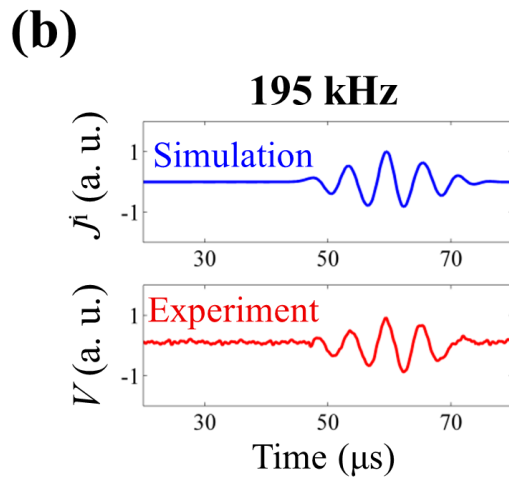
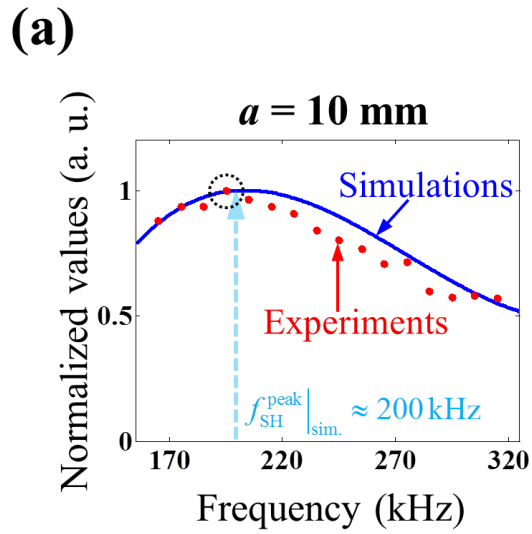


Fig. 4.19 (a) Comparison of the frequency characteristics of the EMATs by experiments and simulations. The width of the two magnets is $a = 10 \text{ mm}$. (b) SH wave signals are chosen at around the peak frequencies ($f_{SH}^{\text{peak}}|_{\text{sim.}}$) as indicated with dotted circles in (a).

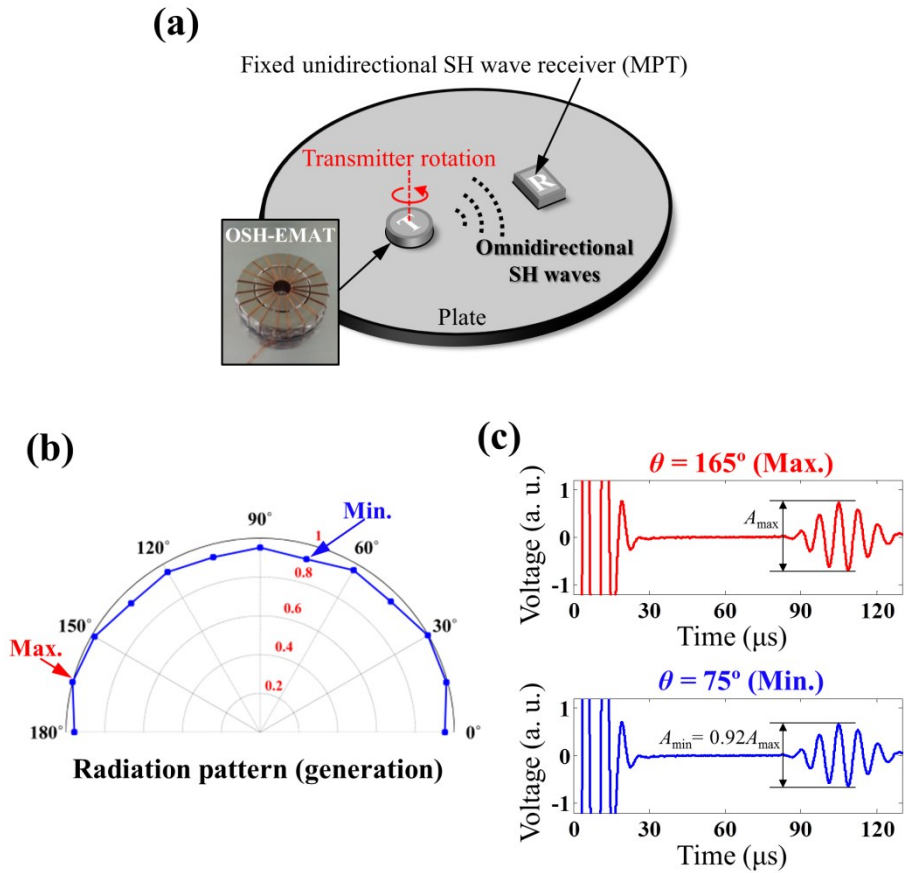


Fig. 4.20 The radiation pattern experiment of the transmitting OSH-EMAT at 130 kHz. (The unidirectional SH wave magnetostrictive patch transducer (MPT) is used as a receiver.) (a) The experimental setup, (b) the radiation pattern determined by the experimental results and the comparison of the signals with the maximum and minimum amplitudes.

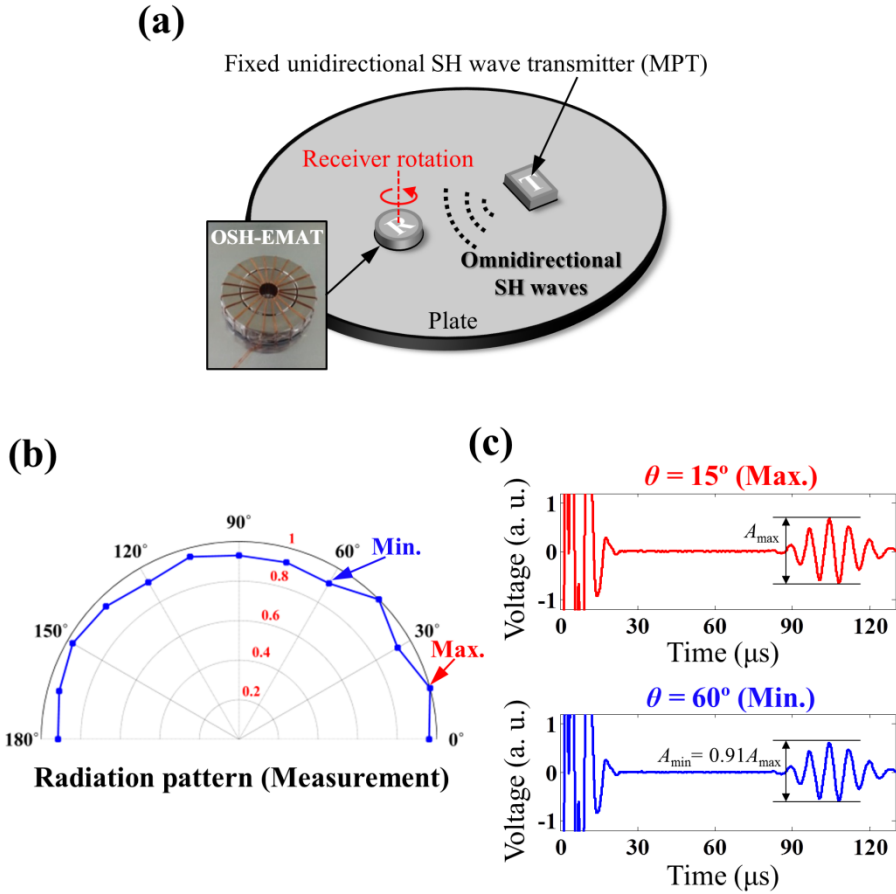


Fig. 4.21 The radiation pattern experiment of the receiving OSH-EMAT at 130 kHz. (The unidirectional SH wave magnetostrictive patch transducer (MPT) is used as a transmitter.) (a) The experimental setup, (b) the radiation pattern determined by the experimental results and the comparison of the signals with the maximum and minimum amplitudes.

CHAPTER 5

CONCLUSIONS

This study presents the development and characterization of the ultrasonic transducers that can generate and measure omnidirectional shear-horizontal guided waves in elastic plate structures. Two types of the transducers are developed as a magnetostrictive patch transducer (MPT) and an electromagnetic acoustic transducer (EMAT), respectively. The newly developed transducers can be an alternative solution to overcome the limitations and disadvantages inherent in using omnidirectional Lamb wave transducers, which are the omnidirectional transducers for plate structures that have only been developed so far. Therefore, it is worth firstly proposing the two omnidirectional SH wave transducers through this study. Considering the possible application using the transducers for practical uses, not only the transducer performance is evaluated but the various characteristics of the transducers are investigated by numerical analysis and experiments. By doing so, the successful development of the MPT and EMAT for omnidirectional SH wave transduction is achieved.

Firstly, an omnidirectional SH wave MPT (OSH-MPT) for an aluminum plate is proposed. The OSH-MPT consists of a cylindrical permanent magnet, a specially wound coil and a thin annular nickel patch that is tightly bonded onto the surface of plates. The measured signal using the transducers is identified only the desired SH wave mode and its linear sensitivity is checked. Furthermore, the frequency characteristic for the OSH-MPTs made of different sizes is investigated. It shows the transduction efficiency of the transducer can be maximized if the patch size is properly chosen according to the wavelength corresponding to the target frequency. More importantly, the measured radiation patterns of the generated and measured SH waves by the OSH-MPT shown to be omnidirectional. The effect of static magnetic field on the sensitivity of the transducer is also examined.

Although the developed OSH-MPT is successfully applied to an aluminum (nonferromagnetic) plate, its direct application to a ferromagnetic plate is challenging due to the adverse effect of the magnetic flux leakage into a ferromagnetic plate. In consideration of the wide use of a ferromagnetic material, this problem should be resolved. So, the configuration of the transducer installed on a ferromagnetic plate is optimally adjusted to reduce the leakage and improve the transducer performance. To this end, numerical and experimental investigations are performed to determine the accurate data for the reconfiguration. According to the results, it is found that the transducer can also be operated on a ferromagnetic plate with great performances.

Secondly, an omnidirectional SH wave EMAT (OSH-EMAT) is proposed. If the transducer is used for metallic structures, it works without any physical contact to the structures unlike the contact type OSH-MPT. Although the sensitivity of EMATs is less sensitive than that of MPTs, the noncontact operation is a predominant advantage of EMATs which makes various practical applications possible. Consequently, the OSH-EMAT can be a useful tool to inspect metallic plates.

The OSH-EMAT is simply formed with a pair of ring magnets and a coil wound on the magnets. The induced Lorentz forces by the transducer on an aluminum plate are axisymmetric and thus the generated SH wave by the forces is omnidirectional. It is successfully confirmed through numerical simulations and a series of experiments. Moreover, by examining the relation between the transducer size and the desired wavelength, the frequency characteristics is investigated so that the transducer output is maximized at a certain target frequency. The effectiveness of the studied frequency characteristic is experimentally verified using the three different sizes of OSH-MPTs in an aluminum plate.

In overall conclusion, because SH waves have several advantages over Lamb waves and cover the limitations of using Lamb waves, the newly developed OSH-MPT and OSH-EMAT can be used to more effectively and efficiently inspect large

plate structures by forming an omnidirectional SH wave based imaging system such as a phased array system. In addition, the combination of OSH-MPT and OSH-EMAT may be useful if the advantages of each transducer are properly considered. Using the developed OSH-MPT and OSH-EMAT in this study, hopefully, there will be many interesting and meaningful researches on the applications for plate structures in the future.

APPENDIX A.

EFFECT OF STATIC MANGETIC FIELD STRENGTH ON THE PERFORMANCE OF LAMB AND SH WAVE MANGETOSTRICTIVE PATCH TRANSDUCERS

A.1 Overview

Effects of the static magnetic field strength on magnetostrictive patch transducers (MPTs) for the transduction efficiencies of the fundamental symmetric Lamb wave mode (S0 mode) and shear horizontal mode (SH0 mode) are investigated. In general, magnetostriction effect of a ferromagnetic material has nonlinear properties so that the performance of MPTs highly depends on the applied static magnetic field strength. Besides, because the directions of applied magnetic fields and deformation of ferromagnetic materials are different to each other for the S0 mode and SH0 mode cases, different characteristics should be observed. Several

wave transduction experiments of the S0 and SH0 wave modes are carried out with respect to the static magnetic field strength variation and the experimental results are analyzed by the piezomagnetic theory. The results show that the transduction efficiency of the S0 wave mode is approximately proportional to the slope of magnetostriction while that of the SH0 wave mode is approximately proportional to magnetostriction itself.

As an effective tool for generating and measuring ultrasonic guided waves, MPTs which can be effectively used even in nonferromagnetic and nonmetallic materials has received considerable attention [40, 43, 53, 54, 56-58, 61, 92]. The working principle of the transducer is magnetostriction effect which refers to the coupling effect between the applied magnetic field to the ferromagnetic patch and its mechanical deformation [38]. Therefore, the performance of the transducer highly depends on the magnetic property of the patch and the applied magnetic field strength. Especially, the static magnetic field applied for biasing of the magnetic field is very important because magnetostriction of the patch generally has the nonlinear properties. However, no research on the effect of the static magnetic field strength on Lamb and SH wave MPTs has been reported so far even though some investigations on the bulk-type magnetostrictive transducer have been carried out [89, 90, 108, 109].

In this paper, hence, the effect of the static magnetic field strength on Lamb and SH wave MPTs is experimentally investigated first for two wave modes, the fundamental symmetric Lamb wave mode (S0 mode) and shear horizontal (SH0 mode) modes, in an aluminum plate. Then, the experimental results are analyzed and the related discussions are addressed through the piezomagnetic theory.

A.2 Experimental investigation

The experimental investigation is conducted first for checking the magnitude variation of the measured Lamb and SH waves by a MPT with respect to varying static magnetic fields in the patch. The specific configuration of the transducer used in this investigation is shown in Fig. A.1. It consists of a thin magnetostrictive (nickel) patch, an electromagnet using a pair of solenoids and a figure-of-eight coil. A static magnetic field for biasing is applied to the patch by the electromagnet and its strength is controlled by the DC current flowing into the solenoids. A dynamic magnetic field for actuating is applied by the AC current flowing into the figure-of-eight coil. Using these two magnetic fields, the transducer can effectively generate guided waves and the generated wave mode can also be easily selected by controlling the directions of two magnetic fields [40]. When the directions of the applied static and dynamic magnetic fields are the same, the S0 wave mode can be generated while the SH0 wave mode can be generated when the directions of two magnetic fields are perpendicular to each other.

For wave transduction using the proposed MPT, another important component that should be contemplated is the dimension of the patch [40, 56]. Unlike the bulk-type magnetostrictive transducer using magnetostriction of the waveguide itself [86, 110-112], the dimension of the patch highly affects the transduction efficiency of MPTs. This is because that the deformed region related to the wavelength is restricted and the direction of the magnetic field in the patch can also be changed by the dimension of the patch. Therefore, the dimension of the patch must be carefully determined taking into account the actuating frequency (or the wavelength) and the direction of the magnetic field in the patch. In this investigation, a 0.15 mm thick nickel patch of 20 mm in length and 10 mm in width which is the same as the width of the yoke is used and placed in parallel with the yoke as shown in Fig. A.1. To generate and measure the SH0 wave mode, therefore, the figure-of-eight coil is perpendicularly installed to that of the S0 wave mode case. The wave transduction experiments are conducted changing the static magnetic field strength of the transmitter and the receiver, respectively. Once the experiments are carried out, the results are analyzed by the piezomagnetic theory in the next sections [44].

Fig. A.2 shows the overall experimental setup for guided wave transduction using two MPTs. The same configurations of the transducers are used for both a transmitter and a receiver, and installed on a 1 mm thick aluminum plate. The static

magnetic field is controlled by the DC current flown into a pair of solenoids of the transducers from 0.1 A to 2.0 A in increment of 0.1 A, resulting in the variation of the magnetic flux density from 0.021 T to 0.209 T. An input signal from a function generator is amplified by a power amplifier (RAM-5000, Ritec Inc. Warwick, RI) and then sent to the transmitter. In the experiment, the Gabor pulse is used as the input signal [87]:

$$f(t) = e^{-\frac{t^2}{2\sigma^2}} \cos(2\pi\eta t + \varphi), \quad (\text{A.1})$$

where σ is the spread in the time axis and η is the center frequency. In the present work, $\sigma = 5.3 \times 10^{-6}$ and $\eta = 150$ kHz are selected for both the S0 and SH0 wave modes. φ is the phase shift and it is fixed to be zero in the experiment.

The actuating frequency is chosen taking account of the dimension of the patch because it highly affects the transduction efficiency of the transducer as mentioned above. From the dispersion relations of the S0 and SH0 wave modes in a test aluminum plate, the actuating frequency is determined as 150 kHz where the length (l_p) and the width (w_p) of the patch correspond to half the wavelengths of the S0 and SH0 modes, respectively. Once the wave is generated by the transmitter, it is

measured by the receiver located 500 mm away from the transmitter. Then, the measured signal is amplified by a preamplifier (SR560 low-noise pre-amplifier, Stanford Research Systems, Sunnyvale, CA) before being recorded by an oscilloscope.

To effectively indicate the tendency of the transduction efficiency due to the static magnetic field strength variation, the peak-to-peak values (V_{p-p}) are extracted from measured signals and normalized by their maximum values. Figs. A.3 ~ A.6 show the results of the S0 and SH0 wave transduction experiments according to various static magnetic field strengths in the transmitter and in the receiver, respectively. In Figs. A.3 and A.4, the static magnetic flux density of the receiver (\mathbf{B}_R^S) is fixed with three different values while that of the transmitter (\mathbf{B}_T^S) is varied from 0.021 T to 0.209 T for both wave modes. Conversely, normalized V_{p-p} values for varying \mathbf{B}_R^S according to three fixed \mathbf{B}_T^S are shown in Figs. A.5 and A. 6.

From the figures, it is can be observed that the different tendencies are shown for the S0 and SH0 wave modes. Specifically, V_{p-p} values are increased in small values of the static magnetic flux density and then decreased rapidly in the S0 wave case (see Figs. A.3 and A.5). In case of the SH0 wave, meanwhile, rapidly increased V_{p-p} values in small values of the static magnetic flux density are

starting to decrease slightly (see Figs. A.4 and A.6). These results will be analyzed by the piezomagnetic theory in the following sections.

A.3 Piezomagnetic theory

The strain resulting from the magnetostriction can be estimated by the piezomagnetic theory [44] as

$$S_I = d_{Ij}^{(MS)} H_j + s_{IJ}^H \sigma_J \quad (I, J = 1, 2, \dots, 6; j = x, y, z), \quad (\text{A.2})$$

$$d_{Ij}^{(MS)} = \left(\frac{\partial S_I}{\partial H_j} \right), \quad (\text{A.3})$$

where S_I is a component of the engineering strain, $d_{Ij}^{(MS)}$ is piezomagnetic strain coefficients. H_j is the applied magnetic field and s_{IJ}^H is a compliance matrix at a constant field and. If the stress-free condition is assumed, say $\sigma_J = 0$, the Eq. (A.2) will simply be

$$S_I = d_{Ij}^{(MS)} H_j . \quad (\text{A.4})$$

To analyze the experimental results with Eq. (A.3), the coordinate system and

magnetic fields supplied by the electromagnet and the figure-of-eight coil indicated in Fig. A.7 are considered.

In case of S0 wave mode transduction, the direction of the two magnetic fields are the same (H_x^B : the bias (static) magnetic field, H_x : the dynamic magnetic field) as shown in Fig. A.7 (a). Accordingly, the static parameters by the bias magnetic field is expressed as

$$H^B = (H_x^B, 0, 0), \quad (\text{A.5})$$

$$S_1^B = \varepsilon^M (H_x^B)^2, S_2^B = S_3^B = -\nu \varepsilon^M (H_x^B)^2, S_4^B = S_5^B = S_6^B = 0, \quad (\text{A.6})$$

where the superscript B represents the bias field and the symbols ν and ε^{MS} denote the poisson's ratio of the patch and the magnetostriction, respectively. Then, when the dynamic magnetic field is also applied to patch in x direction, according to Eq. (A.3), the dynamic strains and the piezomagnetic strain coefficients, respectively, can be approximated as

$$S_1 = \left(\frac{\partial S_1}{\partial H_x} \right) H_x, S_2 = S_3 = -\nu \left(\frac{\partial S_1}{\partial H_x} \right) H_x, S_4 = S_5 = S_6 = 0, \quad (\text{A.7})$$

$$d_{1x} = \left(\frac{\partial S_1}{\partial H_x} \right) \Big|_{\sigma} \equiv \alpha, d_{2x} = d_{3x} = -\nu \alpha, d_{4x} = d_{5x} = d_{6x} = 0, \quad (\text{A.8})$$

where α is the slope of the magnetostriction curve of the patch. Note that the negative sign is used due to the negative magnetostriction effect of the patch.

For the SH0 wave mode case, however, the two magnetic fields are perpendicular each other (H_x^B : the bias (static) magnetic field, H_y : the dynamic magnetic field and) as shown in Fig. A.7 (b). So, the angle between the static and total magnetic fields θ is considered for the transformation. Since the experiments are conducted for various static magnetic flux densities, θ cannot be negligible especially in small values of the static magnetic flux density. Then, the related static strains in the new coordinate according to the total magnetic field is given by

$$S'_1 = \varepsilon^{\text{MS}}(H_t) \equiv \varepsilon_t^{\text{MS}}, S'_2 = S'_3 = -v\varepsilon^{\text{MS}}(H_t) = -v\varepsilon_t^{\text{MS}}, S'_4 = S'_5 = S'_6 = 0, \quad (\text{A.9})$$

where $\varepsilon_t^{\text{MS}}$ is the magnetostriction along the direction of H_t which is the sum of static and dynamic magnetic fields. Now, by taking the coordinate transformation, the induced displacements in this system can be written in a matrix form as

$$\begin{bmatrix} u_1 \\ u_2 \end{bmatrix} = \begin{bmatrix} \cos \theta & \sin \theta \\ -\sin \theta & \cos \theta \end{bmatrix} \begin{bmatrix} u'_1 \\ u'_2 \end{bmatrix}. \quad (\text{A.10})$$

Considering the strain-displacement relation and Eq. (A.10), the strains induced by the piezomagnetic theory are derived by

$$\begin{aligned}
S_1 &= \frac{\partial u_1}{\partial x} = \frac{\partial}{\partial x} (u'_1 \cos \theta + u'_2 \sin \theta) = S'_1 \cos^2 \theta + S'_2 \sin^2 \theta, \\
S_2 &= \frac{\partial u_2}{\partial y} = \frac{\partial}{\partial y} (-u'_1 \sin \theta + u'_2 \cos \theta) = S'_2 \cos^2 \theta + S'_1 \sin^2 \theta, \\
S_3 &= S'_3, \\
S_4 &= S_5 = 0, \\
S_6 &= \frac{\partial u_2}{\partial x} + \frac{\partial u_1}{\partial y} = (S'_2 - S'_1) \sin 2\theta.
\end{aligned} \tag{A.11}$$

Note that the symbolic notation for the coordinate system in [44] is adopted. Finally, using Eqs. (A.3), (A.11) and the following relations,

$$\sin \theta = \frac{H_y}{\sqrt{(H_x^B)^2 + H_y^2}}, \quad \cos \theta = \frac{H_x^B}{\sqrt{(H_x^B)^2 + H_y^2}}, \tag{A.12}$$

$$\frac{\partial S_i}{\partial H_y} = \frac{\partial S'_i}{\partial H'_x} \frac{\partial H'_x}{\partial H_y}, \quad (i = 1, 2, 3), \tag{A.13}$$

the piezomagnetic coefficients for SH wave case can be expressed as

$$\begin{aligned}
d_{1y} &= \frac{3\varepsilon_t^{\text{MS}}}{H_x^{\text{B}}} \cos^3 \theta \sin \theta + \alpha \sin \theta (-\nu \cos^2 \theta + \sin^2 \theta) , \\
d_{2y} &= -\nu \alpha \sin \theta , \\
d_{3y} &= -\frac{3\varepsilon_t}{H_x^{\text{B}}} \cos^3 \theta \sin \theta + \alpha \sin \theta (-\nu \cos^2 \theta + \cos^2 \theta) , \\
d_{4y} &= d_{5y} = 0, \\
d_{6y} &= (1 + \nu) (\alpha \sin 2\theta \sin \theta + \frac{2\varepsilon_t^{\text{MS}}}{H_x^{\text{B}}} \cos^2 \theta \cos 2\theta).
\end{aligned} \tag{A.14}$$

To facilitate the analysis of the experimental results of the used MPT system by the derived piezomagnetic theory so far, it can be regarded and simplified in a matrix form as

$$\begin{bmatrix} S_1 \\ S_2 \\ S_3 \\ S_4 \\ S_5 \\ S_6 \end{bmatrix} = \begin{bmatrix} d_{1x} & 0 & 0 \\ -\nu d_{1x} & 0 & 0 \\ -\nu d_{1x} & 0 & 0 \\ 0 & 0 & 0 \\ 0 & 0 & d_{6y} \\ 0 & d_{6y} & 0 \end{bmatrix} \begin{bmatrix} H_x \\ H_y \\ H_z \end{bmatrix}. \tag{A.15}$$

Therefore, in cases of S0 and SH modes in the given system, respectively, the corresponding strains S_1 and S_6 should be mainly considered as follows:

$$S_1 = d_{1x} H_x, \tag{A.16}$$

$$S_6 = d_{6y} H_y, \quad (\text{A.17})$$

where

$$d_{1x} = \alpha, \quad (\text{A.18})$$

$$d_{6y} = (1 + \nu) \left(\alpha \sin 2\theta \sin \theta + \frac{2\varepsilon_t^{\text{MS}}}{H_x^{\text{B}}} \cos^2 \theta \cos 2\theta \right). \quad (\text{A.19})$$

A.4 Analysis

When the MPT is used for wave transduction, the measured signal is proportional to the time derivative of the strain (S) in the patch, which is also proportional to an input signal [58]. Especially, if the input signal is time harmonic, then the amplitude of the measured signal is directly proportional to the strain in the patch as

$$V \propto S, \quad (\text{A.20})$$

and substituting Eqs. (A.16) and (A.17) into Eq. (A.20) yields

$$V^{\text{S0}} \propto \alpha H_x, \quad (\text{A.21})$$

$$V^{\text{SH0}} \propto d_{6y} H_y, \quad (\text{A.22})$$

where V^{S0} and V^{SH0} are the amplitudes of measured signals for the S0 and SH0 wave modes, respectively. Therefore, it can be concluded that the amplitudes of measured signals for the S0 and SH0 wave modes are proportional to α and d_{6y} , respectively, for given dynamic magnetic fields.

To validate Eqs. (A.21) and (A.22), the magnetostriction curve indicated in [36] is used and the computational simulation of the magneto-static model of the nickel patch is carried out using COMSOL Multiphysics 3.5 [88] to find the magnetic field strength along the nickel patch under the applied magnetic field. In the simulation, a correlation between the magnetic flux density and the magnetic field strength under the stress-free condition is also considered [101]. The experimentally obtained magnetic flux density is used to calculate the induced magnetic field strength along the nickel patch.

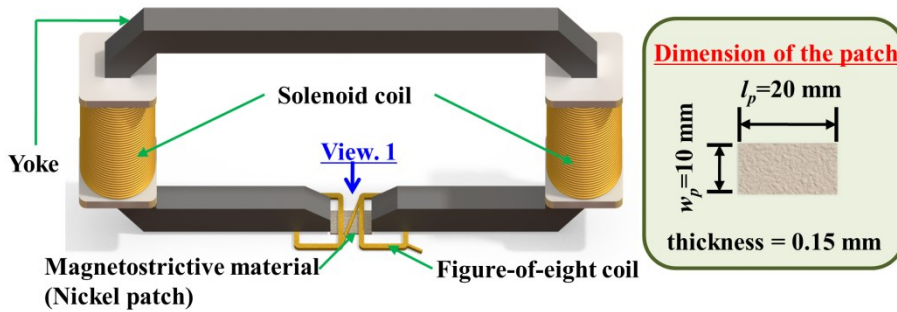
Figs. A.8 (a) and (b) compare the experimental results of the S0 and SH0 mode cases with the theoretical results obtained from Eqs. (A.21) and (A.22), respectively. All results are normalized by their maximum values. From the figures, it can be seen that the experimental results agree well with the theoretical results although a little difference between them is observed at a large magnetic field

strength (\mathbf{H}_T^S) especially for the SH0 wave case. The difference comes from the discrepancy between the magnetic properties of nickel used in the analysis and those used in the experiment. Nevertheless, the experimental and theoretical results show the similar tendency for the effect of the static magnetic field strength.

A.5 Discussion

The effect of the static magnetic field strength on the performance of the magnetostrictive patch transducer is investigated. In experiments, the dimension of the patch is carefully determined because it highly affects not only the generated and measured wave modes but also the magnetic field distribution in the patch unlike bulk-type magnetostrictive transducers. The different tendency of the effect of the static magnetic field strength on the S0 and SH0 wave modes is observed; the transduction efficiency of the S0 wave mode is approximately proportional to the slope of magnetostriction while that of the SH0 wave mode is approximately proportional to magnetostriction of the patch itself. To explain these different characteristics, the piezomagnetic theory is adopted. Although a little difference between the experimental and theoretical results is observed at a large static magnetic field strength range due to the discrepancy between the magnetostrictive properties of the nickel patch used in the analysis and in the experiment, the similar tendency between them is shown. For the optimum transduction efficiencies of the S0 and SH0 wave modes using the magnetostrictive patch transducer, therefore, the

appropriate static magnetic field strengths for both wave modes should carefully be determined.



View. 1 : Different configurations for S0 and SH0 modes

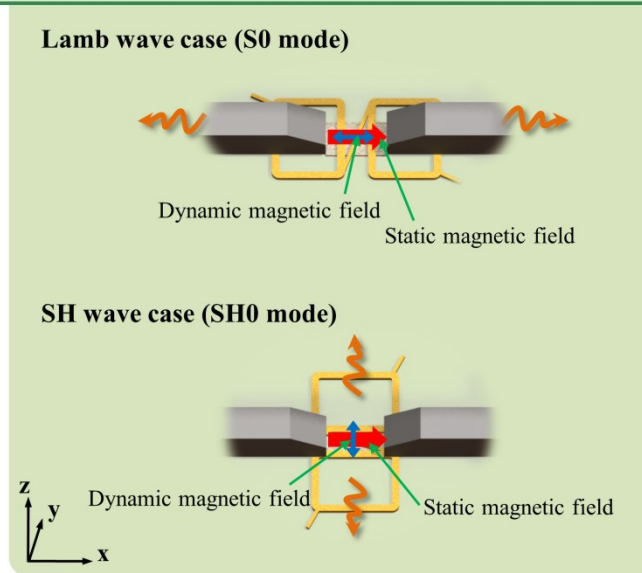


Fig. A.1 The configuration of the magnetostrictive patch transducer and the specification of the patch used in this investigation. Different configurations of figure-of-eight coils for the S0 and SH0 wave modes are also indicated.

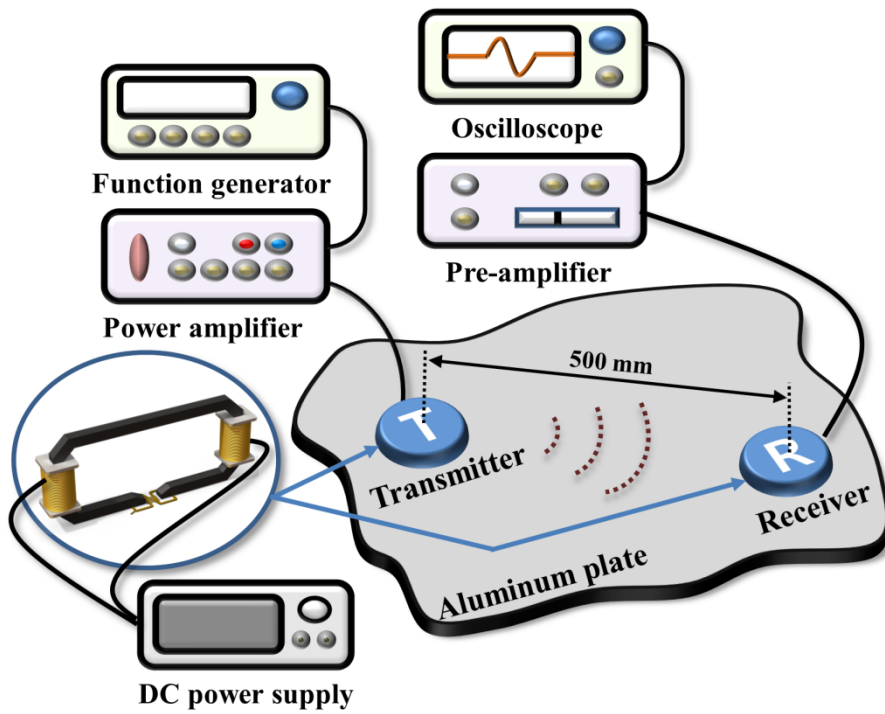


Fig. A.2 The overall experimental setup for guided wave transduction using a pair of the proposed magnetostrictive patch transducers.

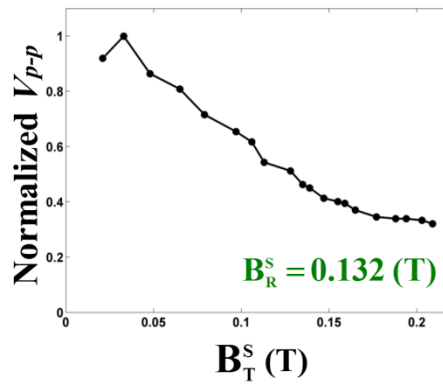
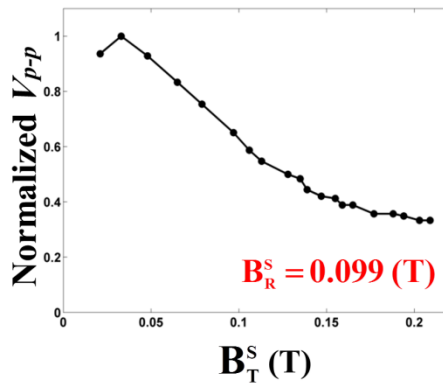
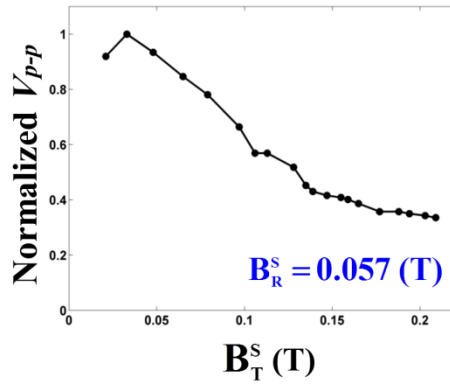


Fig. A.3 Normalized peak-to-peak values (V_{p-p}) of the S0 wave mode corresponding to various static magnetic flux densities in the transmitter (\mathbf{B}_T^S) for three different static magnetic flux densities in the receiver (\mathbf{B}_R^S).

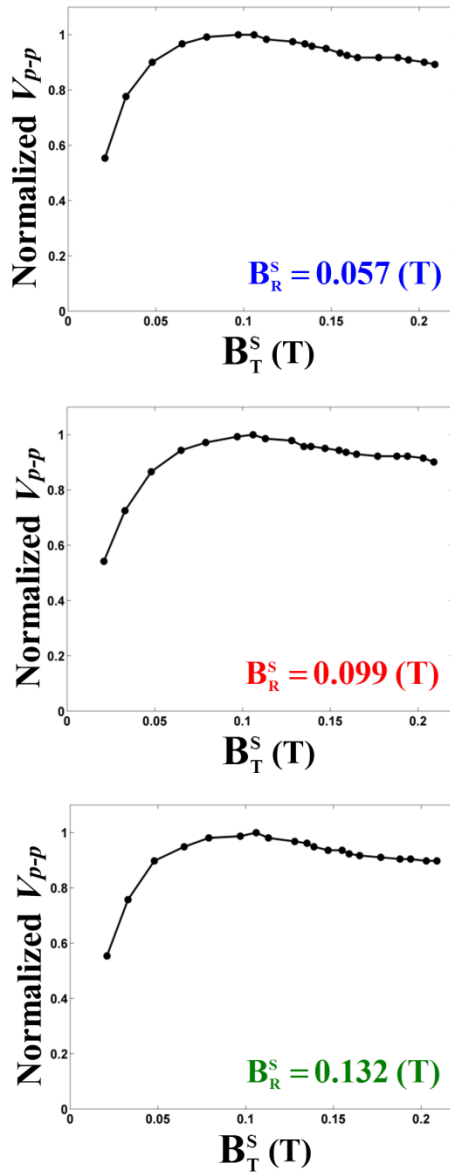


Fig. A.4 Normalized peak-to-peak values (V_{p-p}) of the SH0 wave mode corresponding to various static magnetic flux densities in the transmitter (B_T^S) for three different static magnetic flux densities in the receiver (B_R^S).

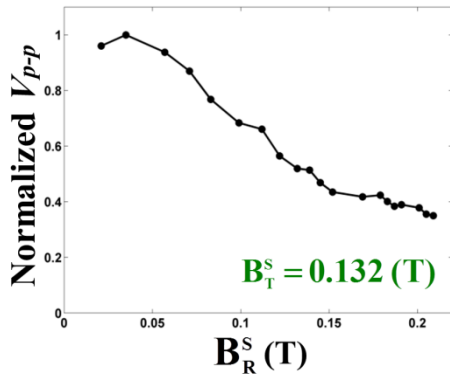
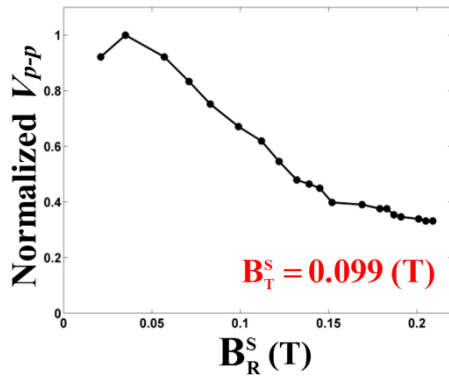
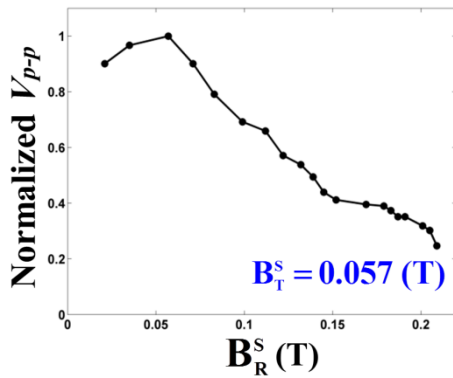


Fig. A.5 Normalized peak-to-peak values (V_{p-p}) of the S0 wave mode corresponding to various static magnetic flux densities in the receiver (B_R^S) for three different static magnetic flux densities in the transmitter (B_T^S).

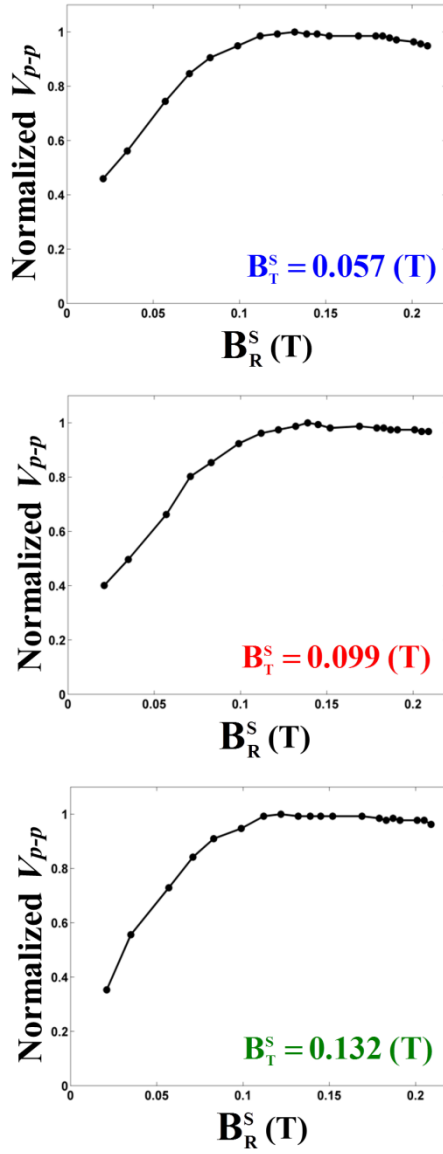
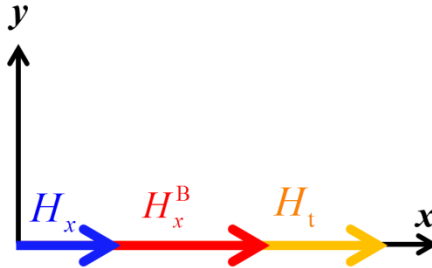


Fig. A.6 Normalized peak-to-peak values (V_{p-p}) of the SH0 wave mode corresponding to various static magnetic flux densities in the receiver (B_R^S) for three different static magnetic flux densities in the transmitter (B_T^S).

(a)



(b)

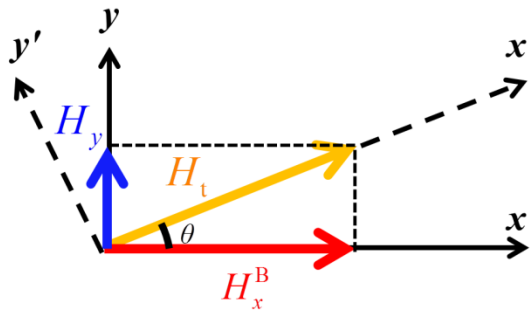


Fig. A.7 Coordinate systems for the piezomagnetic theory analysis of (a) Lamb and (b) SH wave cases. Static, dynamic and total magnetic fields are depicted for both case.

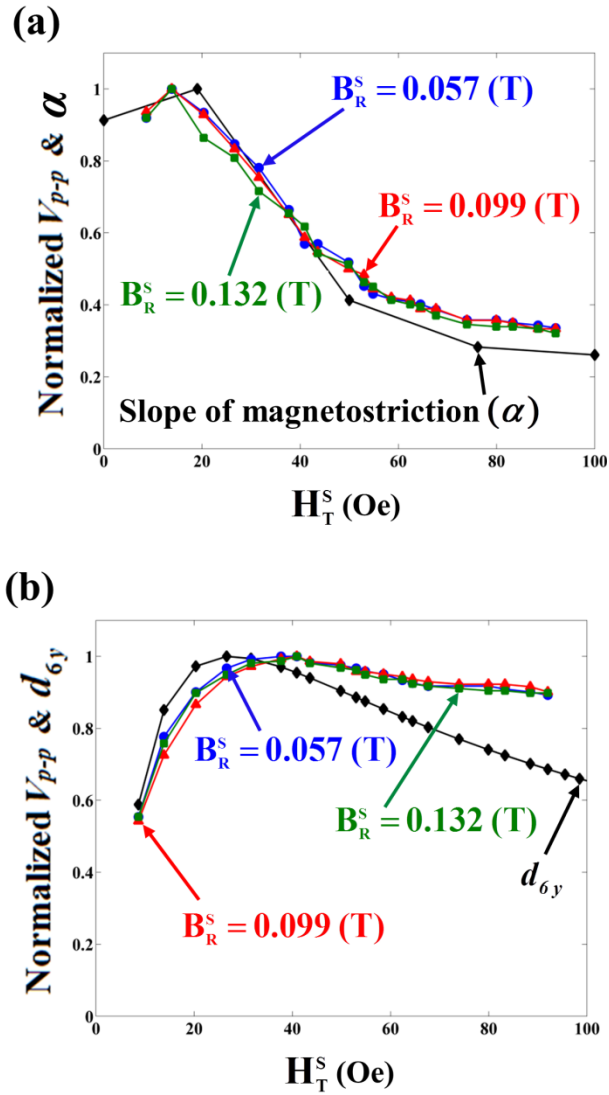


Fig. A.8 Comparison between experimental and theoretical results for (a) the S0 wave mode and (b) the SH0 wave mode according to various static magnetic field strengths in the transmitter (H_T^S)

REFERENCES

- [1] J. Rose, A. Pilarski, J. Ditri, An approach to guided wave mode selection for inspection of laminated plate, *J. Reinf. Plast. Compos.*, 12 (1993) 536-544.

- [2] R. Dalton, P. Cawley, M. Lowe, The potential of guided waves for monitoring large areas of metallic aircraft fuselage structure, *J. Nondestruct. Eval.*, 20 (2001) 29-46.

- [3] S.M. Prasad, K. Balasubramaniam, C. Krishnamurthy, Structural health monitoring of composite structures using Lamb wave tomography, *Smart Mater. Struct.*, 13 (2004) N73.

- [4] P. Fromme, P. Wilcox, M.J. Lowe, P. Cawley, On the development and testing of a guided ultrasonic wave array for structural integrity monitoring, *IEEE Trans. Ultrason. Ferroelectr. Freq. Control*, 53 (2006) 777-785.

- [5] A. Raghavan, C.E. Cesnik, Review of guided-wave structural health monitoring, *SHock Vib. Dig.*, 39 (2007) 91-116.

- [6] X. Zhao, H. Gao, G. Zhang, B. Ayhan, F. Yan, C. Kwan, J.L. Rose, Active health monitoring of an aircraft wing with embedded piezoelectric sensor/actuator network: I. Defect detection, localization and growth monitoring,

Smart Mater. Struct., 16 (2007) 1208.

- [7] J. Li, J.L. Rose, Implementing guided wave mode control by use of a phased transducer array, *IEEE Trans. Ultrason. Ferroelectr. Freq. Control*, 48 (2001) 761-768.
- [8] Y.-M. Cheong, D.-H. Lee, H.-K. Jung, Ultrasonic guided wave parameters for detection of axial cracks in feeder pipes of PHWR nuclear power plants, *Ultrasonics*, 42 (2004) 883-888.
- [9] J. Davies, P. Cawley, The application of synthetic focusing for imaging crack-like defects in pipelines using guided waves, *IEEE Trans. Ultrason. Ferroelectr. Freq. Control*, 56 (2009) 759-771.
- [10] A.C. Cobb, H. Kwun, L. Caseres, G. Janega, Torsional guided wave attenuation in piping from coating, temperature, and large-area corrosion, *NDT E Int.*, 47 (2012) 163-170.
- [11] C. Willey, F. Simonetti, P. Nagy, G. Instanes, Guided wave tomography of pipes with high-order helical modes, *NDT E Int.*, 65 (2014) 8-21.
- [12] W. Zhu, J. Rose, J. Barshinger, V. Agarwala, Ultrasonic guided wave NDT for hidden corrosion detection, *Res. Nondestructive. Eval.*, 10 (1998) 205-225.

- [13] R. Long, M. Lowe, P. Cawley, Attenuation characteristics of the fundamental modes that propagate in buried iron water pipes, *Ultrasonics*, 41 (2003) 509-519.
- [14] T. Vogt, M. Lowe, P. Cawley, The scattering of guided waves in partly embedded cylindrical structures, *J. Acoust. Soc. Am.*, 113 (2003) 1258-1272.
- [15] W. Deutsch, A. Cheng, J. Achenbach, Self-focusing of Rayleigh waves and Lamb waves with a linear phased array, *Res. Nondestruct. Eval.*, 9 (1997) 81-95.
- [16] S.-C. Wooh, Y. Shi, Optimum beam steering of linear phased arrays, *Wave motion*, 29 (1999) 245-265.
- [17] P. Malinowski, T. Wandowski, I. Trendafilova, W. Ostachowicz, A phased array-based method for damage detection and localization in thin plates, *Struct. Health Monit.*, (2008).
- [18] P.D. Wilcox, Omni-directional guided wave transducer arrays for the rapid inspection of large areas of plate structures, *IEEE Trans. Ultrason. Ferroelectr. Freq. Control*, 50 (2003) 699-709.
- [19] P. Wilcox, M. Lowe, P. Cawley, Omnidirectional guided wave inspection of large metallic plate structures using an EMAT array, *IEEE Trans. Ultrason. Ferroelectr. Freq. Control*, 52 (2005) 653-665.

- [20] L. Yu, V. Giurgiutiu, In-situ optimized PWAS phased arrays for Lamb wave structural health monitoring, *J. Mech. Mater. Struct.*, 2 (2007) 459-487.
- [21] M. Engholm, T. Stepinski, Adaptive beamforming for array imaging of plate structures using Lamb waves, *IEEE Trans. Ultrason. Ferroelectr. Freq. Control*, 57 (2010) 2712-2724.
- [22] F. Yan, R.L. Royer, J.L. Rose, Ultrasonic guided wave imaging techniques in structural health monitoring, *J. Intell. Mater. Syst. Struct.*, 21 (2010) 377-384.
- [23] B. Yoo, A. Purekar, Y. Zhang, D. Pines, Piezoelectric-paint-based two-dimensional phased sensor arrays for structural health monitoring of thin panels, *Smart Mater. Struct.*, 19 (2010) 075017.
- [24] K. Salas, C.E. Cesnik, Guided wave excitation by a CLoVER transducer for structural health monitoring: theory and experiments, *Smart Mater. Struct.*, 18 (2009) 075005.
- [25] E. Glushkov, N. Glushkova, O. Kvasha, R. Lammering, Selective Lamb mode excitation by piezoelectric coaxial ring actuators, *Smart Mater. Struct.*, 19 (2010) 035018.
- [26] C.M. Yeum, H. Sohn, J.B. Ihn, Lamb wave mode decomposition using concentric ring and circular piezoelectric transducers, *Wave motion*, 48 (2011)

358-370.

- [27] H.-S. Yoon, D. Jung, J.-H. Kim, Lamb wave generation and detection using piezoceramic stack transducers for structural health monitoring applications, *Smart Mater. Struct.*, 21 (2012) 055019.
- [28] J.P. Koduru, J.L. Rose, Transducer arrays for omnidirectional guided wave mode control in plate like structures, *Smart Mater. Struct.*, 22 (2013) 015010.
- [29] S. Dixon, S. Palmer, Wideband low frequency generation and detection of Lamb and Rayleigh waves using electromagnetic acoustic transducers (EMATs), *Ultrasonics*, 42 (2004) 1129-1136.
- [30] P.D. Wilcox, M.J. Lowe, P. Cawley, The excitation and detection of Lamb waves with planar coil electromagnetic acoustic transducers, *IEEE Trans. Ultrason. Ferroelectr. Freq. Control*, 52 (2005) 2370-2383.
- [31] K. Ho, D. Billson, D. Hutchins, Ultrasonic Lamb wave tomography using scanned EMATs and wavelet processing, *Nondestruct. Test. Eval.*, 22 (2007) 19-34.
- [32] X. Jian, S. Dixon, R. Edwards, K. Quirk, I. Baillie, Effect on ultrasonic generation of a backplate in electromagnetic acoustic transducers, *J. Appl. Phys.*, 102 (2007) 024909.

- [33] P.B. Nagy, F. Simonetti, G. Instanes, Corrosion and erosion monitoring in plates and pipes using constant group velocity Lamb wave inspection, *Ultrasonics*, 54 (2014) 1832-1841.
- [34] M. Seher, P. Huthwaite, M. Lowe, P. Nagy, P. Cawley, Numerical design optimization of an EMAT for A0 Lamb wave generation in steel plates, *Rev. Prog. 40th Quant. NDE*, 1581 (2014) 340-347.
- [35] J.K. Lee, H.W. Kim, Y.Y. Kim, Omnidirectional Lamb waves by axisymmetrically-configured magnetostrictive patch transducer, *IEEE Trans. Ultrason. Ferroelectr. Freq. Control*, 60 (2013) 1928-1934.
- [36] R.M. Bozorth, *Ferromagnetism*, IEEE press, New York, 1993.
- [37] D. Jiles, Theory of the magnetomechanical effect, *J. Phys. D: Appl. Phys.*, 28 (1995) 1537.
- [38] D.C. Jiles, *Introduction to magnetism and magnetic materials*, 2nd ed., Chapman & Hall, London, 1998.
- [39] Y.Y. Kim, Y.E. Kwon, Review of magnetostrictive patch transducers and applications in ultrasonic nondestructive testing of waveguides, *Ultrasonics*, 62 (2015) 3-19.

- [40] S.H. Cho, J.S. Lee, Y.Y. Kim, Guided wave transduction experiment using a circular magnetostrictive patch and a figure-of-eight coil in nonferromagnetic plates, *Appl. Phys. Lett.*, 88 (2006) 224101.
- [41] I.K. Kim, W. Kim, Y.Y. Kim, Magnetostrictive grating with an optimal yoke for generating high-output frequency-tuned SH waves in a plate, *Sensors Actuat. A*, 137 (2007) 141-146.
- [42] I.K. Kim, Y.Y. Kim, Shear horizontal wave transduction in plates by magnetostrictive gratings, *J. Mech. Sci. Technol.*, 21 (2007) 693-698.
- [43] J.S. Lee, Y.Y. Kim, S.H. Cho, Beam-focused shear-horizontal wave generation in a plate by a circular magnetostrictive patch transducer employing a planar solenoid array, *Smart Mater. Struct.*, 18 (2009) 015009.
- [44] M. Hirao, H. Ogi, EMATs for science and industry: noncontacting ultrasonic measurements, Kluwer Academic Publishers, Boston, 2003.
- [45] J. Achenbach, *Wave propagation in elastic solids*, Elsevier, New York, 1973.
- [46] K.F. Graff, *Wave motion in elastic solids*, Dover Publications Inc., New York, 1991.
- [47] J.L. Rose, *Ultrasonic waves in solid media*, Cambridge university press, New

York, 1999.

[48] J. Szilard, Ultrasonic testing: Non-conventional testing techniques, John Wiley & Sons, Inc., New York, 1982.

[49] J. Blitz, G. Simpson, Ultrasonic methods of non-destructive testing, Chapman & Hall, London, 1996.

[50] V. Giurgiutiu, Structural health monitoring: with piezoelectric wafer active sensors, Academic Press, United States of America, 2007.

[51] R. Sicard, J. Goyette, D. Zellouf, A numerical dispersion compensation technique for time recompression of Lamb wave signals, Ultrasonics, 40 (2002) 727-732.

[52] H. Sohn, H.W. Park, K.H. Law, C.R. Farrar, Damage detection in composite plates by using an enhanced time reversal method, J. Aerosp. Eng., 20 (2007) 141-151.

[53] H. Kwun, S.Y. Kim, J.F. Crane, Method and apparatus generating and detecting torsional wave inspection of pipes or tubes, US patent 6429650 B1, August 6, 2002.

[54] S.A. Vinogradov, Method and system for the generation of torsional guided

- waves using a ferromagnetic strip sensor, US patent 7573261 B1, August 11,2009.
- [55] Y.Y. Kim, C.I. Park, S.H. Cho, S.W. Han, Torsional wave experiments with a new magnetostrictive transducer configuration, *J. Acoust. Soc. Am.*, 117 (2005) 3459-3468.
- [56] I.K. Kim, Y.Y. Kim, Wireless frequency-tuned generation and measurement of torsional waves using magnetostrictive nickel gratings in cylinders, *Sensors Actuat. A*, 126 (2006) 73-77.
- [57] E. Kannan, B. Maxfield, K. Balasubramaniam, SHM of pipes using torsional waves generated by in situ magnetostrictive tapes, *Smart Mater. Struct.*, 16 (2007) 2505.
- [58] H.W. Kim, S.H. Cho, Y.Y. Kim, Analysis of internal wave reflection within a magnetostrictive patch transducer for high-frequency guided torsional waves, *Ultrasonics*, 51 (2011) 647-652.
- [59] H.W. Kim, J.K. Lee, Y.Y. Kim, Circumferential phased array of shear-horizontal wave magnetostrictive patch transducers for pipe inspection, *Ultrasonics*, 53 (2013) 423-431.
- [60] H. Kwun, A.J. Parvin, R.H. Peterson, Flexible plate magnetostrictive sensor

probe for guided-wave inspection of structures, US patent 7913562, March 29, 2011.

[61] E. Saidha, G.N. Naik, S. Gopalkrishnan, An Experimental Investigation of a Smart Laminated Composite Beam with a Magnetostrictive Patch for Health Monitoring Applications, *Struct. Health Monit.*, 2 (2003) 273-292.

[62] J.S. Lee, S.H. Cho, Y.Y. Kim, Radiation pattern of Lamb waves generated by a circular magnetostrictive patch transducer, *Appl. Phys. Lett.*, 90 (2007) 054102.

[63] B. Yoo, S.-M. Na, A.B. Flatau, D.J. Pines, Directional magnetostrictive patch transducer based on Galfenol's anisotropic magnetostriction feature, *Smart Mater. Struct.*, 23 (2014) 095035.

[64] Z. Wei, S. Huang, S. Wang, W. Zhao, Magnetostriction-based omni-directional guided wave transducer for high-accuracy tomography of steel plate defects, *IEEE Sens. J.*, 15 (2015) 6549-6558.

[65] B. Yoo, S.-M. Na, A.B. Flatau, D.J. Pines, Magnetic shape anisotropy effect on sensing performance and directional sensitivity in magnetostrictive nickel patch transducer, *J. Intell. Mater. Syst. Struct.*, (2015) 1045389X15585895.

[66] J.P. Joule, XVII. On the effects of magnetism upon the dimensions of iron and steel bars, *The London, Edinburgh, and Dublin Philosophical Magazine and*

Journal of Science, 30 (1847) 76-87.

[67] S. Williams, THE JOULE MAGNETOSTRICTIVE EFFECT IN A GROUP OF COBALT-IRON ALLOYS, Rev. Sci. Instrum., 3 (1932) 675-683.

[68] E. Villari, Change of magnetization by tension and by electric current, Ann. Phys. Chem, 126 (1865) 87-122.

[69] Technical Committee on Transducers and Resonators of Group on Sonics and Ultrasonics, IEEE standard on magnetostrictive materials: Piezo magnetic nomenclature., The Institute of Electrical and Electronics Engineering Inc., New York, 1991.

[70] R. Ribichini, F. Cegla, P.B. Nagy, P. Cawley, Quantitative modeling of the transduction of electromagnetic acoustic transducers operating on ferromagnetic media, IEEE Trans. Ultrason. Ferroelectr. Freq. Control, 57 (2010) 2808-2817.

[71] J.H. Oh, K.H. Sun, Y.Y. Kim, Time-harmonic finite element analysis of guided waves generated by magnetostrictive patch transducers, Smart Mater. Struct., 22 (2013) 085007.

[72] H.J. Kim, J.S. Lee, H.W. Kim, H.S. Lee, Y.Y. Kim, Numerical simulation of guided waves using equivalent source model of magnetostrictive patch transducers, Smart Mater. Struct., 24 (2015) 015006.

- [73] N. Tzannes, Joule and Wiedemann effects-the simultaneous generation of longitudinal and torsional stress pulses in magnetostrictive materials, IEEE Trans. Sonics Ultrason., 13 (1966) 33-40.
- [74] Innerspec Corp., Standard EMAT sensors and accessories, <<http://innerspec.com/products/standard-emat-sensors-and-accessories>> (accessed October 13, 2015).
- [75] M. Hirao, H. Ogi, An SH-wave EMAT technique for gas pipeline inspection, NDT E Int., 32 (1999) 127-132.
- [76] K. Ho, T. Gan, D. Billson, D. Hutchins, Application of pulse compression signal processing techniques to electromagnetic acoustic transducers for noncontact thickness measurements and imaging, Rev. Sci. Instrum., 76 (2005) 054902.
- [77] X. Zhao, V.K. Varma, G. Mei, B. Ayhan, C. Kwan, In-line nondestructive inspection of mechanical dents on pipelines with guided shear horizontal wave electromagnetic acoustic transducers, J. Press. Vessel. Technol.-Tran. ASME, 127 (2005) 304-309.
- [78] R.S. Edwards, S. Dixon, X. Jian, Characterisation of defects in the railhead using ultrasonic surface waves, NDT E Int., 39 (2006) 468-475.

- [79] M. Rosli, R.S. Edwards, B. Dutton, C.G. Johnson, P. Cattani, Identifying surface angled cracks on aluminium bar using emats and automated computer system, *Rev. Prog. 36th Quant. NDE*, 1211 (2010) 1593-1600.
- [80] V. Giurgiutiu, J. Bao, Embedded-ultrasonics structural radar for in situ structural health monitoring of thin-wall structures, *Struct. Health Monit.*, 3 (2004) 121-140.
- [81] L. Yu, V. Giurgiutiu, In situ 2-D piezoelectric wafer active sensors arrays for guided wave damage detection, *Ultrasonics*, 48 (2008) 117-134.
- [82] J. Vishnuvardhan, A. Muralidharan, C. Krishnamurthy, K. Balasubramaniam, Structural health monitoring of anisotropic plates using ultrasonic guided wave STMR array patches, *NDT E Int.*, 42 (2009) 193-198.
- [83] K. Salas, C. Cesnik, Guided wave structural health monitoring using CLoVER transducers in composite materials, *Smart Mater. Struct.*, 19 (2010) 015014.
- [84] S. Vinogradov, Method and system for generating and receiving torsional guided waves in a structure, US patent 7821258, October 26, 2010.
- [85] M.S. Choi, S.J. Kim, Contact SH-guided-wave magnetostrictive transducer, US patent 0091829, April 19, 2012.

- [86] H. Kwun, S.Y. Kim, Magnetostrictive sensor for generating and detecting plate guided waves, *J. Press. Vessel. Technol.-Tran. ASME*, 127 (2005) 284-289.
- [87] J.-C. Hong, K.H. Sun, Y.Y. Kim, The matching pursuit approach based on the modulated Gaussian pulse for efficient guided-wave damage inspection, *Smart Mater. Struct.*, 14 (2005) 548.
- [88] COMSOL Multiphysics, *COMSOL Multiphysics Modeling Guide: Version 3.5*, COMSOL AB, Stockholm, 2008.
- [89] R.B. Thompson, A model for the electromagnetic generation of ultrasonic guided waves in ferromagnetic metal polycrystals, *IEEE Trans. Sonics Ultrason.*, 25 (1978) 7-15.
- [90] R. Murayama, Driving mechanism on magnetostrictive type electromagnetic acoustic transducer for symmetrical vertical-mode Lamb wave and for shear horizontal-mode plate wave, *Ultrasonics*, 34 (1996) 729-736.
- [91] H. Ogi, E. Goda, M. Hirao, Increase of efficiency of magnetostriction SH-wave electromagnetic acoustic transducer by angled bias field: Piezomagnetic theory and measurement, *Jpn. J. Appl. Phys.*, 42 (2003) 3020.
- [92] Y.-G. Kim, H.-S. Moon, K.-J. Park, J.-K. Lee, Generating and detecting torsional guided waves using magnetostrictive sensors of crossed coils, *NDT E*

Int., 44 (2011) 145-151.

- [93] R. Ribichini, F. Cegla, P.B. Nagy, P. Cawley, Study and comparison of different EMAT configurations for SH wave inspection, IEEE Trans. Ultrason. Ferroelectr. Freq. Control, 58 (2011) 2571-2581.
- [94] R. Ribichini, P. Nagy, H. Ogi, The impact of magnetostriction on the transduction of normal bias field EMATs, NDT E Int., 51 (2012) 8-15.
- [95] H.M. Seung, H.W. Kim, Y.Y. Kim, Omni-directional shear-horizontal wave magnetostrictive patch transducer and method of winding coil, US patent pending 13/953633, July 29, 2013.
- [96] J. Rajagopalan, K. Balasubramaniam, C. Krishnamurthy, A single transmitter multi-receiver (STMR) PZT array for guided ultrasonic wave based structural health monitoring of large isotropic plate structures, Smart Mater. Struct., 15 (2006) 1190.
- [97] H.M. Seung, H.W. Kim, Y.Y. Kim, Development of an omni-directional shear-horizontal wave magnetostrictive patch transducer for plates, Ultrasonics, 53 (2013) 1304-1308.
- [98] S. Hill, S. Dixon, Frequency dependent directivity of periodic permanent magnet electromagnetic acoustic transducers, NDT E Int., 62 (2014) 137-143.

- [99] H.M. Seung, Y.Y. Kim, Generation of omni-directional shear-horizontal waves in a ferromagnetic plate by a magnetostrictive patch transducer, *NDT E Int.*, submitted (in revision), June 2015.
- [100] C.I. Park, Y.Y. Kim, Nonferromagnetic material inserted magnetostrictive patch bonding technique for torsional modal testing of a ferromagnetic cylinder, *Rev. Sci. Instrum.*, 81 (2010) 035103.
- [101] T. Suzuki, H. Baba, E. Matsumoto, Stress effect on hysteretic magnetization curve of nickel, *Int. J. Appl. Electromagn. Mech.*, (2003) 307-310.
- [102] T. Zhang, J. Zhong, Y. Lv, T. Cui, J. Qin, J. Xing, M. Li, J. Yang, G. Pan, F. Yang, Magnet Design and Fabrication of CYCIAE-14, a 14 MeV PET Cyclotron, *IEEE Trans. Appl. Supercond.*, 22 (2012) 4101004-4101004.
- [103] P. Petcher, S.E. Burrows, S. Dixon, Shear horizontal (SH) ultrasound wave propagation around smooth corners, *Ultrasonics*, 54 (2014) 997-1004.
- [104] H.M. Seung, Y.Y. Kim, Omni-directional shear-horizontal wave electromagnetic acoustic transducer, US patent pending 14/676198, April 1, 2015.
- [105] H.M. Seung, C.I. Park, Y.Y. Kim, An omnidirectional shear-horizontal guided wave EMAT for a metallic plate, *Ultrasonics*, submitted (in revision),

September 2015.

- [106] C. Borigo, J.L. Rose, F. Yan, A spacing compensation factor for the optimization of guided wave annular array transducers, *J. Acoust. Soc. Am.*, 133 (2013) 127-135.
- [107] J.-C. Hong, K.H. Sun, Y.Y. Kim, Dispersion-based short-time Fourier transform applied to dispersive wave analysis, *J. Acoust. Soc. Am.*, 117 (2005) 2949-2960.
- [108] R.B. Thompson, Mechanisms of electromagnetic generation and detection of ultrasonic Lamb waves in iron-nickel alloy polycrystals, *J. Appl. Phys.*, 48 (1977) 4942-4950.
- [109] R.B. Thompson, Generation of horizontally polarized shear waves in ferromagnetic materials using magnetostrictively coupled meander-coil electromagnetic transducers, *Appl. Phys. Lett.*, 34 (1979) 175-177.
- [110] H. Kwun, A. Holt, Feasibility of under-lagging corrosion detection in steel pipe using the magnetostrictive sensor technique, *NDT E Int.*, 28 (1995) 211-214.
- [111] H. Kwun, K. Bartels, Magnetostrictive sensor technology and its applications, *Ultrasonics*, 36 (1998) 171-178.

[112] Z. Liu, J. Zhao, B. Wu, Y. Zhang, C. He, Configuration optimization of magnetostrictive transducers for longitudinal guided wave inspection in seven-wire steel strands, *NDT E Int.*, 43 (2010) 484-492.

ABSTRACT (KOREAN)

전방향 전단 탄성과 구현을 위한 평판용 초음파 트랜스듀서

승 홍 민

서울대학교 대학원

기계항공공학부

본 논문은 평판구조물에서 설치되어 모든 방향으로 전단 탄성파를 고르게 발생 및 측정할 수 있는 초음파 트랜스듀서의 최초 개발과 그 응용을 다루었다. 기존의 전방향 유도초음파 트랜스듀서 개발에 관한 연구들은 모두 램파를 사용하는 것에 국한되었기에 본 연구에서 개발된 전방향 전단파 트랜스듀서들을 이용하면 램파의 단점들을 극복할 수 있을 뿐 아니라 보다 효과적인 평판구조물 검사가 가능할 것으로 기대된다. 따라서, 자기변형 원리와 전자기 음향 현상을 이용한 두 가지 종류의 전방향 전단파 트랜스듀서들을 각각 새롭게 개발하고 그 특성을 파악하는 연구를 수행하였다.

먼저 전방향 전단파 자기변형 패치 트랜스듀서를 개발하였고 해석과 실험을 통하여 개발된 트랜스듀서의 성능과 특성을 검증하였다. 더 나아가 트랜스듀서가 강자성체 평판에 설치되었을 때 발생하는 자속 누설이 트랜스듀서 성능 저하에 끼치는 연구를 수행하였다. 자속누설로 인한 문제를 해결하기 위해 트랜스듀서를 최적으로 구성하는 방법도 제시하였다. 이를 통해 더욱 실질적인 평판구조물의 검사에 적용할 수 있는 가능성을 확인하였다.

더불어, 평판구조물에 직접적으로 부착하지 않고 전방향으로 전단파를 발생 및 측정할 수 있는 전자기 음향 트랜스듀서를 개발하였다. 개발된 트랜스듀서는 비접촉식으로 구조물에 쉽게 설치되기 때문에 보다 정확하고 효율적이며 다양한 평판 검사에 적용이 가능하다. 트랜스듀서의 유효성을 확인하고자 수치적 해석과 실험을 수행하였다. 이를 통해 성공적으로 트랜스듀서의 성능을 그 유용성을 입증하였다.

주요어: 초음파 트랜스듀서, 전방향 트랜스듀서, 전단파, 유도초음파, 자기변형 패치 트랜스듀서, 전자기음향 트랜스듀서

학 번 : 2010-20689